

International Review of Biophysical Chemistry (IREBIC)

Contents

Ag⁺-Induced Arrangement of Poly(dC) into Compact Ring-Shaped Structures <i>by Dragoslav Zikich, Irit Lubitz, Alexander Kotlyar</i>	1
Dye-Liposome Interactions: Dye Localization in Neutral Lipid Bilayers <i>by Virginia Castillo, Salvador Ventura, Raimon Sabaté</i>	7
Multi Transition States for S_N2 Reaction in Intramolecular Processes <i>by Rafik Karaman, Shireen Alfalal</i>	14
Multivariate and T₁ Analysis on Serum Samples from Coronary Heart Disease Patients (CHD): a Pilot Study <i>by Divya Misra, Usha Bajpai</i>	24
Physico-Chemical Changes of Human Serum Albumin During in Vivo and in Vitro Glycation Processes <i>by N. Sattarahmady, A. A. Moosavi-Movahedi, M. Habibi-Rezaei, H. Heli</i>	29
Purine Nucleoside Phosphorylase as a Molecular Target to Develop Active Compounds Against <i>Mycobacterium Tuberculosis</i> <i>by Rodrigo G. Ducati, André A. Souto, Rafael A. Caceres, Walter F. de Azevedo Jr., Luiz A. Basso, Diógenes S. Santos</i>	34
Adsorption of Rhodamine B Dye – Thermodynamic and Equilibrium Studies <i>by K. Baskaran, B. R. Venkatraman, S. Arivoli</i>	41
Poly (Methyl Methacrylate-co-Maleic Anhydride-co-N-Isopropylacrylamide): Synthesis, Characterization and Antimicrobial Activity <i>by E. Uzluk, M. Talu</i>	49



Ag⁺-Induced Arrangement of Poly(dC) into Compact Ring-Shaped Structures

Dragoslav Zikich¹, Irit Lubitz¹, Alexander Kotlyar^{1,2}

Abstract – We report the synthesis, circular dichroism (CD) and atomic force microscopy (AFM) characterization of DNA-based ring-shaped nanostructures resulting from folding of 700 base poly(dC) strands in the presence of silver ions (Ag⁺). The AFM contour length and height analyses of the molecules suggest that the poly(dC) strand in complex with Ag⁺ can wrap around itself forming a double helical circular molecule. Incubation of stoichiometrical complex between poly(dG)-poly(dC) with Ag⁺ at 50°C leads to dissociation of the strands and to spontaneous folding of the G-strand into monomolecular G-quadruplex and the C-strand into double stranded C-C duplex stabilized by Ag-ions. Copyright © 2010 Praise Worthy Prize S.r.l. - All rights reserved.

Keywords: AFM, CD, DNA, Poly(dC), G-quadruplex, Silver Ions

I. Introduction

Interaction of Ag⁺ with nucleic acids has been a subject of extensive studies in the 60's and 70's [1-10]. It has been demonstrated that Ag⁺ has higher binding affinity to nucleic bases as compared to phosphate residues [11]. The affinity of the Ag⁺ to G- and C-bases is much higher compared to the affinity of T- and A-basis, leading to a selective binding of the cation to oligonucleotides composed of G- and C-fragments [12]. The X-ray diffraction analysis of the complex between C-base analogue, (nitrate)(1-methylcytosine) and silver ions revealed that in the crystal, each two C-bases are bridged by two Ag⁺ linked to N(3) and O(2') atoms of the C-bases [13]. It has been also shown that C-dyads are forming columnar arrays in the crystal [13]. The mass spectroscopic analysis of a mixture of (dC)₁₂ with Ag⁺ showed the presence of the oligonucleotide fraction corresponding to 2x(dC)₁₂ with 10-12 Ag⁺ [14]. This led authors to suggest that Ag⁺ can mediate the formation of C-C duplex [14]. It was shown that melting temperature of duplex DNA containing C-C mismatch increases upon addition of Ag⁺, also suggesting the stabilization of duplex formation by the Ag⁺ [15]. All the studies were performed on short C-oligonucleotides or C-bases.

Here, we report that incubation of 700 base, uniform poly(dC) strands, (dC)₇₀₀, with Ag⁺ results in the formation of a high affinity complex between the DNA and the cation. The complex is characterized by a circular dichroism (CD) spectrum with a strong negative band around 270 nm. The CD titration data showed that the band amplitude reaches its maximum at a 2:1 molar ratio between C-base and Ag⁺, suggesting that one silver ion is linked to two C-bases in the (dC)₇₀₀-Ag⁺ complex. Atomic Force Microscopy (AFM) imaging revealed that

the complex arranges into a compact ring-shaped structure. The average contour length of the folded (dC)₇₀₀-strand is equal to about half the length of the 700 base pairs (bp) poly(dG)-poly(dC), indicating that poly(dC) strand folds back on itself in a hairpin fashion and form an intramolecular circular duplex with C-C pairs stabilized by silver ions. The height of the folded complex is similar to that of dsDNA, supporting its double-stranded nature. Furthermore, we show that incubation of a complex between Ag⁺ and poly(dG)-poly(dC) at low ionic strength, at 50°C for 30 min, leads to separation of the strands and independent folding of the G-strand into monomolecular G-quadruplex and the C-strand into a double stranded circular duplex structure.

II. Experimental Section

II.1. Materials

Unless otherwise stated, the reagents were obtained from Sigma-Aldrich (USA) and were used without further purification. Klenow fragment of DNA polymerase I from E.coli lacking the 3'→5' exonuclease activity (Klenow exo⁻) was purchased from Fermentas (Lithuania).

II.2. Methods

II.2.1. DNA Samples

(dC)₁₀ and (dG)₁₀ oligonucleotides were purified using an ion-exchange PolyWax LP column (4.6×200 mm, 5 μm, 300 Å) (Western Analytical Products, USA) at pH 7.5 and pH 12, respectively. HPLC-purified oligonucleotides were desalted using pre-packed

Sephadex G-25 DNA-Grade columns (GE Healthcare, UK). 700 bp poly(dC)-poly(dG), [(dC)₇₀₀-(dG)₇₀₀], was synthesized as described previously [16]. The reaction solution contained HPLC purified 1.5 μ M (dC)₁₀-(dG)₁₀, 1.2 mM dGTP, 1.2 mM dCTP, 60 mM K-Pi (pH 7.4), 3 mM MgCl₂, 5 mM DTT, 0.2 μ M Klenow exo⁻. Concentrations of G- and C-homopolymers were calculated using extinction coefficients of 11.7 and 7.5 mM⁻¹ cm⁻¹ for G and C-bases at 260 nm [17], respectively.

II.2.2. DNA Polymerase Assays

The synthesis reaction contained 60 mM K-Pi (pH 7.4), 3 mM MgCl₂, 5 mM DTT, 2 mM of dGTP, 0.17 mM of HPLC purified (dC)₂₀, 0.2 μ M Klenow exo⁻ and 0.2 μ M (dC)₇₀₀-(dG)₇₀₀. Reaction was triggered by the addition of the enzyme. The sample was pre-incubated for 15 min at room temperature, followed by the incubation for 2 hours at 37°C. The synthesis yielded molecules composed of a 5000 base G-strand, 700 base C-strand and several (n) (dC)₂₀ oligonucleotides annealed with the G-strand, (dG)₅₀₀₀-(dC)₇₀₀-n(dC)₂₀.

II.2.3. HPLC Separation of the Polymerase Products

(dG)₅₀₀₀-(dC)₇₀₀-n(dC)₂₀ molecules were separated from nucleotides, template-primers and other reaction components of the synthesis, using size-exclusion HPLC. The separation was achieved with a 7.8×300 mm TSK-gel G-DNA PW HPLC column (TosoHaas, Japan) by isocratic elution with 20 mM Tris-Ac at pH 7.5 for 30 min at a flow rate of 0.5 ml per min. Size-dependent separation of fragments composing (dG)₅₀₀₀-(dC)₇₀₀-n(dC)₂₀ was performed using a 7.8×300 mm TSK-gel G-DNA PW HPLC column, (TosoHaas, Japan), by isocratic elution with 0.1 M NaOH at a flow rate of 0.5 ml per min. Separation of (dG)₇₀₀ and (dC)₇₀₀-Ag⁺ structures originated from rearrangement of (dG)₇₀₀-(dC)₇₀₀ in the presence of Ag-ions was performed on the same HPLC column, by isocratic elution with 20 mM Tris-Ac at pH 7.5 for 30 min at a flow rate of 0.5 ml per min. All the experiments were conducted on Agilent 1100 HPLC system with a photodiode array detector. Peaks were identified by their retention times obtained from the absorbance at 260 and 300 nm.

II.2.4. CD and Absorption Spectroscopy

CD spectra were recorded at 25°C with a Chirascan Circular Dichroism Spectrometer (Applied Photonics, UK). Each spectrum was recorded from 220 to 320 nm and represents an average of 3 scans. Absorption spectra of the synthesized products were acquired with a Jasco V-630 spectrophotometer (Japan).

II.2.5. AFM Imaging

Atomic force microscopy was conducted on molecules adsorbed onto muscovite mica surfaces. 20 μ l of 0.2 nM (in molecules) DNA samples in 2 mM Tris-Ac (pH 7.4), containing 2 mM MgCl₂, were incubated on a 1 x 1cm freshly cleaved mica plates for 2-5 minutes, washed with distilled water and dried with nitrogen gas. AFM images were acquired with a Solver PRO AFM (NT-MDT, Russia) in a semi-contact (tapping) mode using Si-gold-coated cantilevers (NT-MDT, Russia) 130 μ m long with resonance frequency of 119-180 KHz. The images were "flattened" (each line of the image was fitted to a 2nd- order polynomial, and the polynomial was then subtracted from the image line) by the AFM's image processing software package. The images were analyzed using WSxM 3.0 imaging software (Nanotec Electronica S.L., Madrid) [19]. The analyses of the DNA lengths and heights are expressed as average values \pm standard deviation.

III. Results

A method for the preparation of long uniform poly(dC) comprises the following steps: (I) Enzymatic synthesis of (dC)₇₀₀-(dG)₇₀₀, as described previously [16]; (II) Enzymatic extension of the G-strand in the (dC)₇₀₀-(dG)₇₀₀ in the presence of dGTP and (dC)₂₀-oligonucleotides as described in [20]; (III) Size-exclusion HPLC separation of the strands composing the synthesized molecule in 0.1M NaOH. The main difference between the method applied in this study and the one developed by us earlier, for the preparation of long poly(dG) strands, is the length of the starting poly(dG)-poly(dC) [20]. In the previous work, a short (dG)₁₀-(dC)₁₀ oligonucleotides were subjected to a polymerase reaction, while here we used much longer polymer, (dC)₇₀₀-(dG)₇₀₀. The enzymatic extension of only G-strand in (dC)₇₀₀-(dG)₇₀₀ was achieved in the assay containing dGTP and (dC)₂₀. The product of the synthesis reaction is a double stranded polymer comprising the initial (dC)₇₀₀ strand, thousands base long continuous G-strand and (dC)₂₀ fragments associated with the *de novo* G-strand, d(G)₅₀₀₀-(dC)₇₀₀-n(dC)₂₀.

At pH > 12.5, the polynucleotide fragments, (dG)₅₀₀₀, (dC)₇₀₀ and (dC)₂₀, composing the DNA, are separated from each other and are eluted as discrete peaks from the HPLC column. Size-dependent HPLC separation of fragments composing the above polymer, by isocratic elution with 0.1M NaOH is shown in the Fig. 1. As seen in the figure, the G-strand fraction is eluted from the column between 13 and 15 min (Fig. 1, peak 1) in a volume corresponding to polymer composed of thousands of bases.

The C-strand fraction is eluted 2-3 min after the G-one (Fig. 1, peak 2), while (dC)₂₀ fragments are eluted in a full column volume, ~5 min after the C-strands (not shown in the figure).

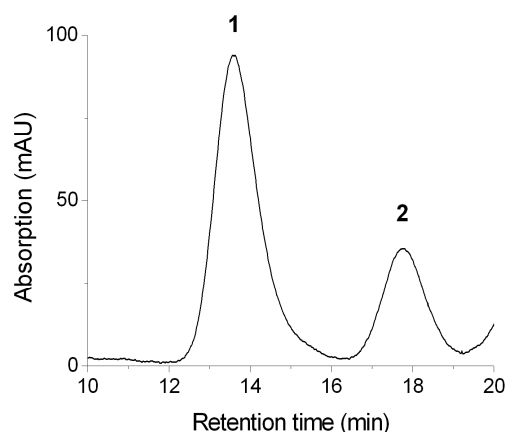
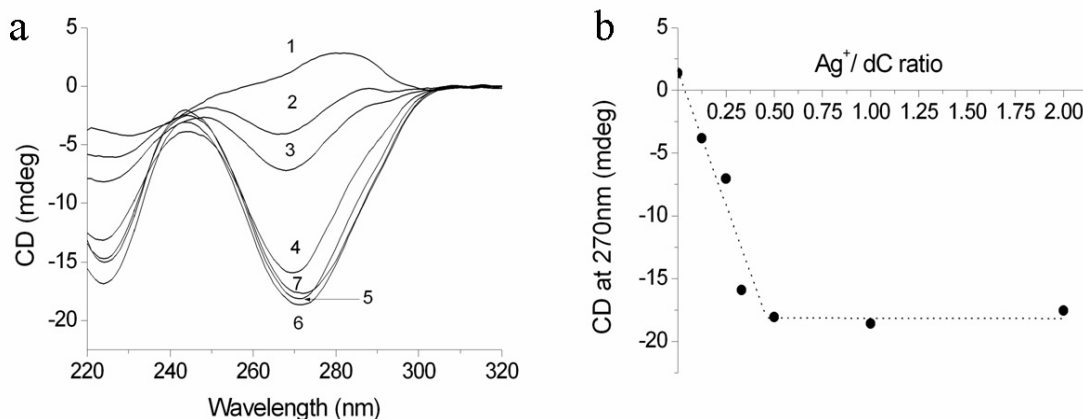


Fig. 1. Size-dependent HPLC separation of the strands composing (dG)₅₀₀₀-(dC)₇₀₀-n(dC)₂₀ at alkaline pH. Numbers 1 and 2 indicate the elution positions of 5000 base poly(dG) and 700 base poly(dC) strands, respectively. The elution was followed at 300 nm. The separation was done by isocratic elution with 0.1 M NaOH at a flow rate of 0.5 ml/min

The HPLC separation of (dG)₅₀₀₀ and (dC)₇₀₀ strands composing the DNA, enables preparation of highly purified and uniform poly(dC) strands. The C-strand fraction was collected from the column and subsequently dialyzed against 500 ml of 20 mM Tris-Ac pH 7.5 at room temperature for 2 hours, in order to reduce the pH of the sample. The samples were stored at 4 °C until use.

Ag⁺ ions induce a strong negative band at 270 nm in the CD spectrum of a (dC)₇₀₀ (Fig. 2a, compare curves 1 and 6). Earlier reports have shown that Ag⁺ ions cause similar changes in CD spectrum of a short single-stranded (dC)₁₂ oligonucleotide [21]. Titration of (dC)₇₀₀ with Ag⁺ shows that maximum enhancement of the CD signal amplitude at 270 nm is achieved at a 1 to 2 molar ratio between Ag⁺ and C-bases (Fig. 2b). The increase of the Ag⁺ to base ratio beyond 0.5 is not associated with changes; either in the shape of the spectrum or the amplitude of the signal at 270 nm (see Figs. 2). This behavior is consistent with the formation of a complex in

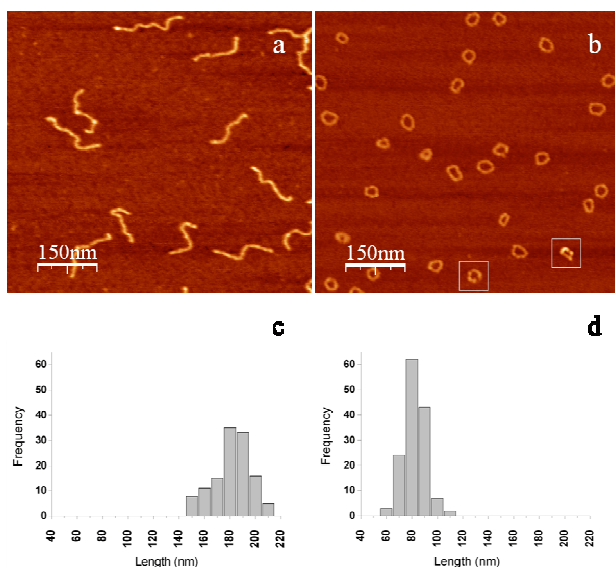


Figs. 2. Ag⁺-induced changes in the CD spectrum of (dC)₇₀₀. (a) 25 μM (concentration expressed in C-bases) (dC)₇₀₀ (line 1) was incubated with 3.12 μM (line 2), 6.25 μM (line 3), 8.33 μM (line 4), 12.5 μM (line 5), 25 μM (line 6) and 50 μM (line 7) Ag⁺ in 20 mM Tris-Ac (pH 7.5) for 15 min at 25°C. The CD spectra were recorded at 25°C. Each spectrum is an average of three scans. (b) Concentration dependence of the CD signal at 270 nm. The dependence of signal amplitude at 270 nm (estimated from spectra presented in a) is plotted as a function of Ag⁺ to C-base ratio

which one Ag⁺ is bound to two C-bases of the polynucleotide. The shape of a CD spectrum and the relative amplitude of the signal at 270 nm do not change during the size-exclusion chromatography of (dC)₇₀₀-Ag⁺ (data not presented), showing that the complex is stable and does not dissociate in a size-exclusion column.

Figures 3 show the AFM imaging and statistical analysis of 700 bp poly(dG)-poly(dC) and (dC)₇₀₀-Ag⁺ molecules. The (dC)₇₀₀-Ag⁺ complex was prepared by incubation of 50 μM (dC)₇₀₀ (concentration expressed in C-bases) with 25 μM Ag⁺. The molecules were deposited on a freshly cleaved muscovite mica surface and scanned by AFM in a semi-contact mode. As seen in the image, (dC)₇₀₀-Ag⁺ molecules appear as single ring-shaped compact structures (Fig. 3b); the poly(dG)-poly(dC) molecules, as expected, have a linear-like conformation on the surface (Fig. 3a). The average length of (dC)₇₀₀-Ag⁺ molecules is 85 ± 9 nm, which is about half the average length of 700 bp poly(dG)-poly(dC), 177 ± 17 nm (see Fig. 3c and d, respectively). The images reveal that both ends of the (dC)₇₀₀-Ag⁺ molecule are approaching each other forming a closed circular structure. A small number of partly folded structures can be also detected on the surface.

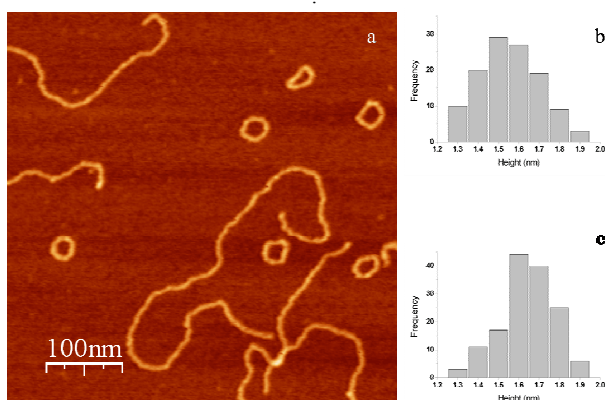
In these structures (marked by white squares in Fig. 3b) the opposite ends of the folded DNA molecule are not connected to each other. Occasionally, the (dC)₇₀₀-Ag⁺ molecules were seen in an extended, open conformation on a large surface areas (not shown). The height relations between (dC)₇₀₀-Ag⁺ molecules and a standard, double-stranded linear plasmid DNA (pUC19) co-deposited on a mica surface are shown in Figs. 4. Plasmid DNA is easily distinguished on the image by its linear shape and much longer contour. The estimated apparent height, extracted from cross-sections of many (dC)₇₀₀-Ag⁺ molecules is 1.67 ± 0.15 nm. This value is identical, within the experimental error, to the average height of the plasmid DNA, 1.56 ± 0.16 nm.



Figs. 3. AFM images of 700 bp poly(dG)-poly(dC) (a) and (dC)₇₀₀-Ag⁺ (b) molecules. The (dC)₇₀₀-Ag⁺ complex was prepared by incubation of 50 μM (concentration expressed in C-bases) (dC)₇₀₀ with 25 μM Ag⁺. Poly(dG)-poly(dC) and (dC)₇₀₀-Ag⁺ molecules were deposited on mica under the same conditions. Statistical contour length analysis of poly(dG)-poly(dC) (c) and (dC)₇₀₀-Ag⁺ (d) molecules

Interaction of 700 bp poly(dG)-poly(dC) with Ag⁺ results in the formation of a strong complex between the DNA and the cation. The complex is stable to column chromatography and is characterized by a stoichiometry of one Ag⁺ per G-C base pair (data not presented). Incubation of the complex in 2 mM Tris-Ac at pH 7.5 for 30 min at 50°C results in strands separation. As seen in Fig. 5 (solid curve) the strands are eluted separately from the size-exclusion HPLC column. The C-strand fraction is eluted from the column between 14.5 and 16 min, whereas the G-strand fraction is eluted approximately 2 min later. This shows that G-structures have smaller molecular size than the C-ones.

The absorption spectra of the former and latter fractions fit nicely with those of G and C nucleotides, respectively (data not presented).



Figs. 4. (a) (dC)₇₀₀-Ag⁺ were co-deposited with a linear DNA molecules (pUC19) on a mica surface. The plasmid DNA can be easily distinguished by its much longer length. Statistical analyses of the apparent height of (b) single well separated plasmid and (c) ring structure

The poly(dG)-poly(dC) is eluted from the column as a single peak between 14 and 16 min (see Fig. 5, dashed curve). The molecular morphology of the eluted structures was revealed by AFM. Both C- and G-fractions were collected from the column, deposited on freshly cleaved mica and imaged. As seen in Fig. 6, the C-structures are similar to those formed in the poly(dC) solution in the presence of Ag⁺ (see Fig. 3b). The ring-shaped molecules are clearly seen in the image together with linear structures. The molecular morphology of the latter structures corresponds nicely with that of 700 bp poly(dG)-poly(dC). We thus suggest that a minor fraction of the molecules did not dissociate into single strands.

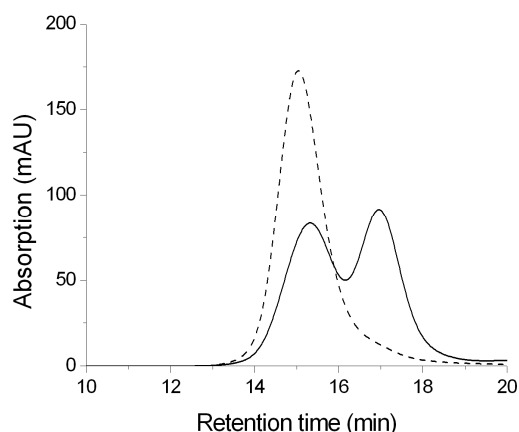
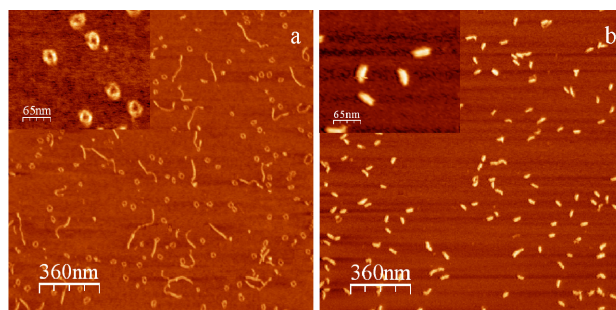
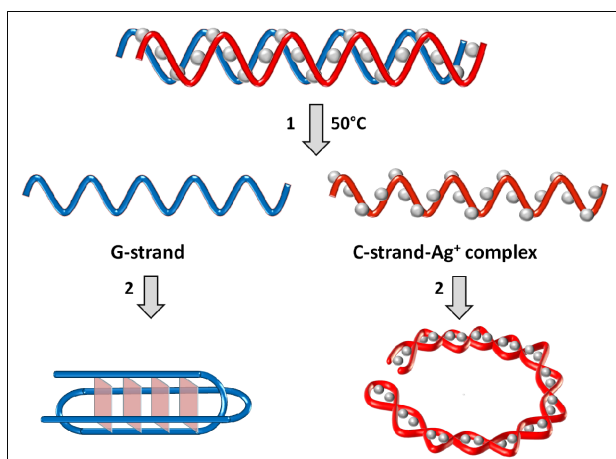


Fig. 5. Size-dependent HPLC of 700 bp poly(dG)-poly(dC) molecules before (dashed line) and after (solid line) incubation with Ag⁺ at 50°C for half an hour (solid curve). The elution was followed at 260 nm. The separation was done by isocratic elution with 20 mM Tris-Ac (pH 7.5)

The G-structures eluted from the column are seen in Fig. 6b, as rod-shaped structures. The average contour length of the structures is approximately equal to 40 nm, which is about one-fourth the length of 700 bp poly(dG)-poly(dC). We thus propose that the G-strand undergoes folding into a monomolecular G-quadruplex (see scheme in Figs. 7). We have demonstrated (data not presented) that the G-structures strongly bind a G-quadruplex specific dye, Thiozol Orange [22]. This also confirms the G-quadruples nature of the above structures.



Figs. 6. AFM images of separated DNA fractions (a) The fractions containing C- and (b) G-strands, eluted from the HPLC column (see Fig. 5) on mica surface. Both fraction were deposited on mica under the same conditions. Insets in a and b; Enlargement of C- and G-structures respectively



Figs. 7. Model for molecular reorganization of poly(dG)–poly(dC) in the presence of Ag^+ . The figure depicts the assumed events during incubation of a poly(dG)–poly(dC)– Ag^+ complex at 50°C . (1) Incubation of the ds DNA with Ag^+ (shown as grey spheres) results in separation of G- (blue line) and C- (red line) strands. (2) Subsequent folding of the G-strand into a monomolecular G-quadruplex and complex of the C-strand with Ag^+ into a ring-shaped C-C duplex

IV. Conclusion

We have synthesized the uniform $(\text{dC})_{700}$ molecules using Klenow exo⁻ fragment of DNA polymerase I. The employed synthesis procedure yielded uniform poly(dC) strands with narrow distribution of molecular sizes. Ag^+ strongly affects the CD spectrum of $(\text{dC})_{700}$. The effect on the spectrum reaches its maximum at a 1 to 2 molar ratio between Ag^+ and C-bases, suggesting that one Ag^+ is bound per two C-bases in a $(\text{dC})_{700}\text{-Ag}^+$ complex. The complex is stable and does not dissociate during size-exclusion chromatography. The $(\text{dC})_{700}\text{-Ag}^+$ molecules form a circular configuration on a mica surface. The statistical analysis of AFM images (see Figs. 3) showed that the contour length of the molecules is approximately equal to half the length of the 700 bp poly(dG)-poly(dC). This suggests that poly(dC) strand in $(\text{dC})_{700}\text{-Ag}^+$ complex can wrap around itself forming a duplex structure with C-C pairs. The duplex further folds into a compact circular structure (see schematic drawing, Figs. 7). The proposed double stranded configuration of $(\text{dC})_{700}\text{-Ag}^+$ complex is in a good agreement with mass spectroscopic data, showing the presence of $(\text{dC})_{12}$ oligonucleotide in a double stranded form, $2 \times (\text{dC})_{12}$, in complex with 10-12 Ag^+ [14].

We show that incubation of a stoichiometrical complex between poly(dG)-poly(dC) and Ag^+ -ions at 50°C , results in separation of the strands composing the DNA (reaction 1 in Figs. 7). Poly(dG) and poly(dC) strands fold independently into monomolecular G-quadruplexes and ring-shaped double stranded C-structures stabilized by Ag^+ , respectively (reaction 2 in Figs. 7). Thus, we suggest that in the presence of Ag^+ -ions the free energy of system comprising monomolecular G-quadruplexes and C- Ag^+ -C duplexes is lower than that of poly(dG)-poly(dC).

A novel DNA nanostructures reported in this work might possess interesting mechanical and conductive properties. One may speculate that redox active Ag^+ ions could promote charge migration through the complex. Exploring the properties of $(\text{dC})_{700}\text{-Ag}^+$ structures may lead to the development of new functional DNA-based nanomaterials with novel physicochemical characteristics.

Acknowledgements

This work was supported by European Commission FP6 Information Society Technologies program, grant “DNA-Based Nanodevices”, and by the ISF Converging Technologies program, grant 1714/0.

References

- [1] Arroye Arya, S.K. and Yang, J.T. Optical rotatory dispersion and circular dichroism of silver(I):Polyribonucleotide complexes. *Biopolymers, Volume 14*, (Issue 9), 1975, Pages 1847-1861.
- [2] Dattagupta, N. and Crothers, D.M. Solution structural studies of the $\text{Ag}(\text{I})$ -DNA complex. *Nucleic Acids Res, Volume 9*, (Issue 12), 1981, Pages 2971-2985.
- [3] Daune, M., Dekker, C.A. and Schachman, H.K. Complexes of silver ion with natural and synthetic polynucleotides. *Biopolymers, Volume 4*, (Issue 1), 1966, Pages 51-76.
- [4] Dove, W.F. and Davidson, N. Cation effects on the denaturation of DNA. *Journal of Molecular Biology, Volume 5*, (Issue 5), 1962, Pages 467-478.
- [5] Eichhorn, G.L., Butzow, J.J., Clark, P. and Tarien E. Interaction of metal ions with polynucleotides and related compounds. X. Studies on the reaction of silver(I) with the nucleosides and polynucleotides, and the effect of silver(I) on the zinc(II) degradation of polynucleotides. *Biopolymers, Volume 5*, (Issue 3), 1967, Pages 283-296.
- [6] Izatt, R.M., Christensen, J.J. and Rytting, J.H. Sites and thermodynamic quantities associated with proton and metal ion interaction with ribonucleic acid, deoxyribonucleic acid, and their constituent bases, nucleosides, and nucleotides. *Chemical Reviews, Volume 71*, (Issue 5), 1971, Pages 439-481.
- [7] E Jensen, R.H. and Davidson, N. Spectrophotometric, potentiometric, and density gradient ultracentrifugation studies of the binding of silver ion by DNA. *Biopolymers, Volume 4*, (Issue 1), 1966, Pages 17-32.
- [8] Shin, Y.A. and Eichhorn, G.L. Induction of helicity in polyuridylic acid and polyinosinic acid by silver ions. *Biopolymers, Volume 19*, (Issue 3), 1980, Pages 539-556.
- [9] Yamane, T. and Davidson, N. (1962) Note on the spectra of the mercury(II) and silver(I) complexes of some polyribonucleotides and ribonucleic acid. *Biochim. Biophys. Acta, Volume 55*, 1960, Pages 780-782.
- [10] Yamane, T. and Davidson, N. On the complexing of deoxyribonucleic acid by silver(I). *Biochim. Biophys. Acta, 55*, 1962, Pages 609-621.
- [11] Eichhorn, G.L. Inorganic Biochemistry. G. L. Eichhorn, (ed. Elsevier, Amsterdam, New York, 1973, Vollume II, Chapter 33).
- [12] Shukla, S. and Sastry, M. Probing differential Ag^+ -nucleobase interactions with isothermal titration calorimetry (ITC). *Towards patterned DNA metallization Nanoscale, Volume 1*, 2009, Pages 122-127.
- [13] Kistenmacher, T.J., Rossi, M. and Marzilli, L.G. Crystal and molecular structure of (nitrate)(1-methylcytosine)silver(I): an unusual crosslinked polymer containing a heavy metal and a modified nucleic acid constituent. *Inorganic Chemistry, Volume 18*, (Issue 2), 1979, Pages 240-244.
- [14] Ritchie, C.M., Johnsen, K.R., Kiser, J.R., Antoku, Y., Dickson, R.M. and Petty, J.T. Ag Nanocluster Formation Using a Cytosine

Oligonucleotide Template. *The Journal of Physical Chemistry C*, Volume 111, (Issue 1), 2006 Pages 175-181.

- [15] Ono A, Cao S, Togashi H, Tashiro M, Fujimoto T, Machinami T, Oda S, Miyake Y, Okamoto I, Tanaka Y. Specific interactions between silver(I) ions and cytosine-cytosine pairs in DNA duplexes. *Chem Commun (Camb)*. (Issue 39) 2008, Pages 4825482-7.
- [16] Kotlyar, A.B., Borovok, N., Molotsky, T., Fadeev, L. and Gozin, M. In vitro synthesis of uniform poly(dG)-poly(dC) by Klenow exo- fragment of polymerase I. *Nucleic Acids Res*, Volume 33, (Issue 2), 2005, Pages 525-535.
- [17] Cantor, C.R., Warshaw, M.M. and Shapiro, H. Oligonucleotide interactions. 3. Circular dichroism studies of the conformation of deoxyoligonucleotides. *Biopolymers*, Volume 9, (Issue 9), 1970, Pages 1059-1077.
- [18] Wells, R.D., Larson, J.E., Grant, R.C., Shortle, B.E. and Cantor, C.R. Physicochemical studies on polydeoxyribonucleotides containing defined repeating nucleotide sequences. *Journal of Molecular Biology*, Volume 54, (Issue 3), 1970, Pages 465-497.
- [19] Horcas, I., Fernandez, R., Gomez-Rodriguez, J.M., Colchero, J., Gomez-Herrero, J. and Baro, A.M. WSXM: A software for scanning probe microscopy and a tool for nanotechnology. *Rev Sci Instrum*, Volume 78, (Issue 1), 2007, Pages 013705.
- [20] Borovok, N., Molotsky, T., Ghabboun, J., Porath, D. and Kotlyar, A. Efficient procedure of preparation and properties of long uniform G4-DNA nanowires. *Anal Biochem*, Volume 374, (Issue 1), 2008, Pages 71-78.
- [21] Petty, J.T., Zheng, J., Hud, N.V. and Dickson, R.M. DNA-Templated Ag Nanocluster Formation. *Journal of the American Chemical Society*, Volume 126, (Issue 6), 2004, Pages 5207-5212.
- [22] Lubitz, I., Zikich, D. and Kotlyar, A.B. Specific High-Affinity Binding of Thiazole Orange to Triplex and G-Quadruplex DNA. *Biochemistry*, Volume 49 (Issue 17), 2010, Pages 3567-3574.
- [23] D. Gorinevsky, S. Boyd, G. Stein, Optimization-based tuning of low-bandwidth control in spatially distributed systems, *American Control Conference*, Vol. 3, pp. 2658-2663, Denver, CO, June 2003.

Authors' information

¹Department of Biochemistry, George S. Wise Faculty of Life Sciences, Tel Aviv University, 69978 Ramat Aviv, Israel

²Department of Biochemistry, George S. Wise Faculty of Life Sciences, The Center for Nanoscience and Nanotechnology, Tel Aviv University, 69978 Ramat Aviv, Israel



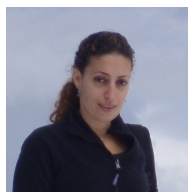
Alexander Kotlyar was born in Moscow, Russia, May 1957. Graduated in Biochemistry and got his PhD in Biochemistry at Moscow State University in 1985. A staff member of Tel Aviv University, Israel since 1994. His major research interests since 2001 focus around the DNA-based nanostructures. He developed novel methods for enzymatic synthesis of various

DNA nanowires and complexes of the wires with metal particles.

Prof. Kotlyar



Dragoslav Zikich was born in Belgrade, Serbia, January 1970. He got Biotechnology Engineering degree from Braude Technology College in Karmiel, Israel, in 1998. He graduated MSc in Neurobiochemistry in 2004 at Tel Aviv University and presently, has completed the PhD studies in Biochemistry at Tel Aviv University, Israel. From 2006 his research is focused on alternative DNA structures and DNA-metal nanoparticle materials.



Irit Lubitz was born in Ramat Gan, Israel, January 1977. She got B.Sc degree in biology from Bar Ilan University Israel, in 2004. She graduated MSc in Biochemistry in 2007 at Tel Aviv University, Israel. In 2007 she started her PhD studies in Biochemistry at Tel Aviv University, under the supervision of Prof. Kotlyar. Her research is focused on novel DNA-based functional nanomaterials.

Dye-Liposome Interactions: Dye Localization in Neutral Lipid Bilayers

Virginia Castillo¹, Salvador Ventura², Raimon Sabaté³

Abstract – A large number peptides and proteins can interact with lipid membranes, these contacts serve different functions and their deregulation is associated to different human disorders. Although cyanine dyes have become standard optical probes to study protein conformational changes upon membrane binding, their interactions with lipid bilayers remain essentially unexplored. In the present work we characterize the association of Congo Red (CGR), merocyanine (MER) and pinacyanol (PIN) with DMPC liposomes by spectrophotometry. These dyes exhibit different association constants and localization at the liposome membrane. Dye affinity to liposome exhibits the following gradation: MER>PIN>CGR. Importantly, bound MER and PIN are localized in inner nonpolar region of the DMPC bilayer whereas CGR interacts preferentially with the more polar bilayer surface. These dye properties should be taken into account when dissecting protein-membrane interactions using spectroscopic approaches. **Copyright © 2010 Praise Worthy Prize S.r.l. - All rights reserved.**

Keywords: Association Constant, Congo Red, Dimerization Constant, Dye, Liposome, Merocyanine, Pinacyanol

I. Introduction

Liposomes are vesicles in which a small volume is entirely enclosed by a membrane composed of phospholipids. Lipid bilayers are widely used as membrane models and biological membrane similes. Studies of membrane-protein contacts and more recently membrane-amyloid interactions are the object of an increasing interest. In this context, liposomes represent ideal systems to study the mechanisms of permeabilization, protein insertion and pore formation by toxic protein conformers [1]-[13].

Cyanine dyes have frequently been used as optical probes in the study of membranes, surfactants, micellar systems, proteins and amyloid aggregation [14]-[23]; Among cyanine dyes, merocyanine-540 (MER) or pinacyanol (PIN) have been used in multiple studies of protein – membrane interaction and amyloid association [21], [24]-[26]. Congo Red (CGR) is a diazo dye that binds to many amyloid proteins because of their β -sheet structure [27], [28]. Careful analysis of liposome-dye interactions are a necessary prerequisite to understand in the context of the study of protein-membrane interaction.

Cyanine dyes, as other dyes, have a demonstrated ability to form associates such as dimers, and H- and J-aggregates. This association is strongly favoured in water, and even at low dye concentrations, dimers and higher order aggregates can be present in equilibrium with the monomeric species [29]. To obtain the real association constant for the liposome – dye interaction the dye dimerization constant has to be previously determined and considered in the binding equation.

In the present work, we present a study of the interaction of neutral liposomes with three dyes commonly used in protein-membrane interaction and amyloid formation studies. The dimerization and association constants as well as the localization of the dyes at the liposome bilayer have been characterized.

II. Experimental methods

II.1. Materials

PIN, MER and CGR were obtained from Sigma-Aldrich (St. Louis, MO, USA); 1,2-Dimyristoyl-*sn*-Glycero-3-Phosphocholine (DMPC) Avanti Polar Lipids (Alabaster, AL, USA). Dye solutions were made in double-distilled water purified through a Milli-Q system (Millipore, USA).

II.2. Procedure to Prepare Dye Solutions

Stock solutions of PIN and MER were made in CHCl_3 . When necessary, the required amount was placed in a round-bottomed flask and evaporated at reduced pressure. To remove CHCl_3 traces, the residue was freeze-dried overnight and the appropriate solution was prepared. Stock solution of CGR was made in water. All preparations were kept in the dark and wrapped in aluminium foil to lower the likelihood of photodecomposition during storage. To minimize dye adsorption, glassware and cuvettes were silanated with 2% (v:v) dichloromethylsilane/toluene solution and then rinsed with methanol.

II.3. Procedure to Prepare Liposomes

DMPC was dissolved in a mixture (2:1, volume ratio) of chloroform and methanol in a round-bottom flask and dried in a rotary evaporator under reduced pressure at 40 °C to form a thin film on the flask. The film was hydrated for 24 h in 10mM TRIS-HCl buffer at pH 7.4. Multilamellar liposomes (MLV) were formed by gentle sonication in a Transonic Digital bath sonifier (Elma, Germany) for 10 min. MLV were downsized to form oligolamellar vesicles by extrusion at room temperature in a Liposofast device (Avestin, Canada) through two polycarbonate membrane filters of 0.2- μ m pore size a minimum of 21 times [30]. Vesicle size was measured by dynamic light scattering with a Malvern II-C autosizer. Vesicles have a mean diameter of 200 nm and a narrow size distribution (polydispersity <0.1).

II.4. Spectral Overlapping Peaks Determination

From the 4th derivative spectrum of dyes we obtained that PIN and MER were formed by three principal bands whereas CGR was formed by four ones. Hence, PIN, MER and CGR spectra (from dimer or monomer) were fitted to three or four overlapping Gaussian curves and the amplitude, center and bandwidth at half of the maximum amplitude and area of each Gaussian function were been calculated using a non-linear peak fitting program (PeakFit package, Systat Software, San Jose, CA, USA).

II.5. Spectroscopic Measurements

The absorption spectra were recorded with a Shimadzu UV-2401 PC UV-visible spectrophotometer (Shimadzu, Japan) using a matched pair of glass cuvettes of 1 cm optical length placed in a thermostated cell holder, at 25 \pm 0.1 °C. Spectra were fitted to three overlapping Gaussian curves with the help of a Gaussian curve fitting program that made it possible to obtain the amplitude, center, band width at half of the maximum amplitude and area of each Gaussian function.

II.6. Determination of the Dimerization Constant

Assuming the only existence of dimers and monomers of PIN in an aqueous solution, the equilibrium between monomer and dimer ($2M \leftrightarrow D$) at a temperature T is described by the dimerization constant K_D , which is given by the ratio between the molar concentrations of dimers, C_D , and monomers, C_M , at equilibrium:

$$K_D = \frac{C_D}{C_M^2} \quad (1)$$

On the other hand, the total absorbance of a PIN solution per unity of optical length at a given wavelength ($A(\lambda)$) is:

$$A(\lambda) = \varepsilon_M(\lambda)C_M + \varepsilon_D(\lambda)C_D \quad (2)$$

where ε_M and ε_D represent the molar absorption coefficients of monomeric and dimeric species, respectively, at a wavelength λ .

From equations 1 and 2 and considering the mass balance of PIN in the volume dispersion, the following equation is obtained:

$$A(\lambda) = \varepsilon_D(\lambda) \left(\frac{C}{2} - \frac{-1 \pm \sqrt{1 + 8K_D C}}{8K_D} \right) + \varepsilon_M(\lambda) \left(\frac{C}{2} - \frac{-1 \pm \sqrt{1 + 8K_D C}}{4K_D} \right) \quad (3)$$

where C is the total analytical concentration of PIN.

By plotting the measured absorbances as a function of dye concentration at any wavelength, the molar absorptivity of monomer, $\varepsilon_M(\lambda)$, and dimer, $\varepsilon_D(\lambda)$, as well as the dimerization constant, K_D , were calculated using a nonlinear least-squares fitting routine program.

II.7. Bound Dye Determination

The amount of bound dye was calculated using a spectrophotometric method using two wavelengths [21,27]:

$$[Dye]_{bound} = \frac{(A_t^{\lambda_1} / \varepsilon_f^{\lambda_1}) - (A_t^{\lambda_2} / \varepsilon_f^{\lambda_2})}{(\varepsilon_b^{\lambda_1} / \varepsilon_f^{\lambda_1}) - (\varepsilon_b^{\lambda_2} / \varepsilon_f^{\lambda_2})} \quad (4)$$

where A and ε are absorbance and molar absorptivity for each λ (wavelength) and the free (f) and bound (b) forms. In all of cases, liposome scattering was previously corrected.

II.8. Determination of the Association Constant

The dye - liposome bindings were calculated using the typical one site binding equation (saturation binding curve):

$$y = \frac{B_{max} * x}{K_A + x} \quad (5)$$

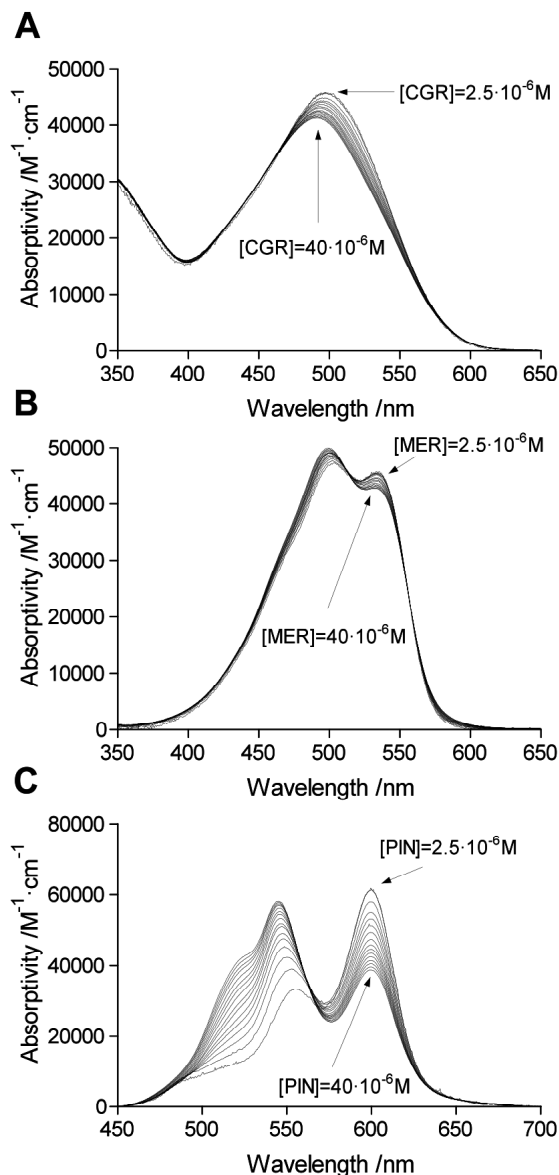
where y is concentration of ThT bound to DMPC liposomes, B_{max} is the maximum number of binding sites expressed in concentration, x is ThT concentration and K_A is the process constant.

III. Results and Discussion

III.1. Effects of Dye Concentration on Absorption Spectra: Dimerization Constant Determination

It is known that cyanine and other related dyes have a natural tendency to aggregate spontaneously in solution

when dye concentration is increased or the solution temperature is lowered. Dye molecules aggregation, promote a change on the absorption spectrum relative to the monomer, and, apparently, the dye behaviour deviates from that expected according to the Lambert-Beer law. The molar absorptivity of each dye was measured at increasing dye concentrations (see Figs. 1).



Figs. 1. Effect of dye concentration on the visible absorption spectra of CGR (A), MER (B) and PIN (C) in 10 mM of TRIS buffer at pH7.5 and 25°C

Molar absorptivity varied with concentration and the spectra revealed the presence of a well-defined isosbestic point at 465.5, 516.5 and 562.5 nm for CGR, MER and PIN, respectively. The existence of these isosbestic points indicates equilibrium between two states of dye molecules. Since at the used concentrations higher order aggregates are not significantly populated, although a simplification, we can assume that the monomer–dimer equilibrium is the only equilibrium contributing to

changes in the molar absorptivity of the compound in this low concentration range.

From the spectral data of the dyes at different concentrations (see Figs. 1), we obtained the values for the dimerization constant (Table I) as well as the molar absorptivities of monomer and dimer (Figs. 2) for each dye. From the dimerization constant (K_D) it can be calculated the free energy change of the dimerization process (ΔG^D):

$$\Delta G^D = -RT \cdot \ln K_D \quad (6)$$

where R is the gas constant and T is the absolute temperature. Negative ΔG^D values (Table I) denote the natural tendency of those dyes to form dimers.

TABLE I
VALUES OF MONOMER-DIMER DYE EQUILIBRIUM

	Congo Red	Merocyanine	Pinacyanol
K_D / M^{-1}	9964±126	6420±11	18343±113
λ_{max}^{mon} / nm	498.5	534.5	599.0
λ_{max}^{dim} / nm	475.5	493.5	542.0
$\Delta\lambda_{max}^{mon-dim} / nm$	23.0	41.0	57.0
λ_{isos} / nm	465.5	516.5	562.5
$E_T^{mon} / kJ \cdot mol^{-1}$	239.97	223.810	199.71
$E_T^{dim} / kJ \cdot mol^{-1}$	251.58	242.40	220.71
$\Delta G^D / kJ \cdot mol^{-1}$	-22.812	-21.72	-24.32

From the wavelength of maximal absorbance we calculated the molar electronic transitional energies (E_T) of dyes in each state. E_T values expressed as $kJ \cdot mol^{-1}$ were obtained as:

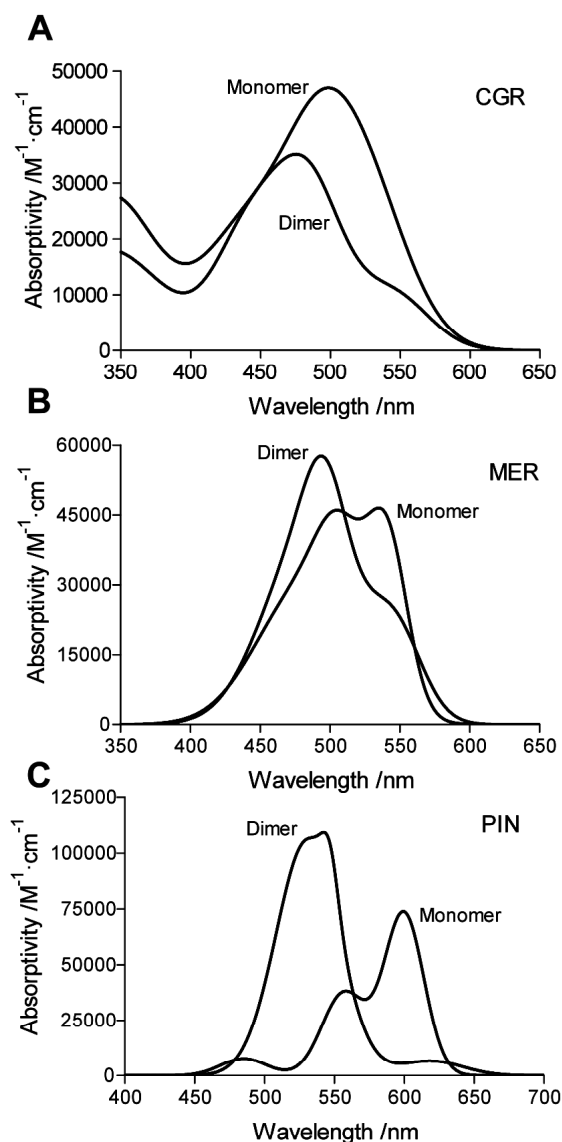
$$E_T = \varepsilon_M(\lambda) hc N_A / \lambda_{max} = 119600 / \lambda_{max} (nm) \quad (7)$$

where h is the Planck constant, c is the vacuum light velocity, and N_A is the Avogadro's constant. Differences between E_T values for monomer and dimer reflect the variation in energy in the transference process from monomer to dimer. The positive values of these differences are indicative of the dyes dimerization propensity (Table I).

III.2. Interaction of Dyes with DMPC Liposomes

The interaction of DMPC liposomes with dyes was then studied at several DMPC concentrations ranging from 0 to 1.7mM and $1 \cdot 10^{-6} M$ of dye. Figs. 3 represent the dyes absorptivity spectra at different DMPC concentrations.

Isosbestic points at 460.0 and 559.0 nm are observed for CGR and PIN, respectively, indicating equilibrium between two spectrophotometrically distinguishable states of CGR and PIN. In CGR spectra, it is possible to detect a secondary isosbestic point at 548.0 nm.

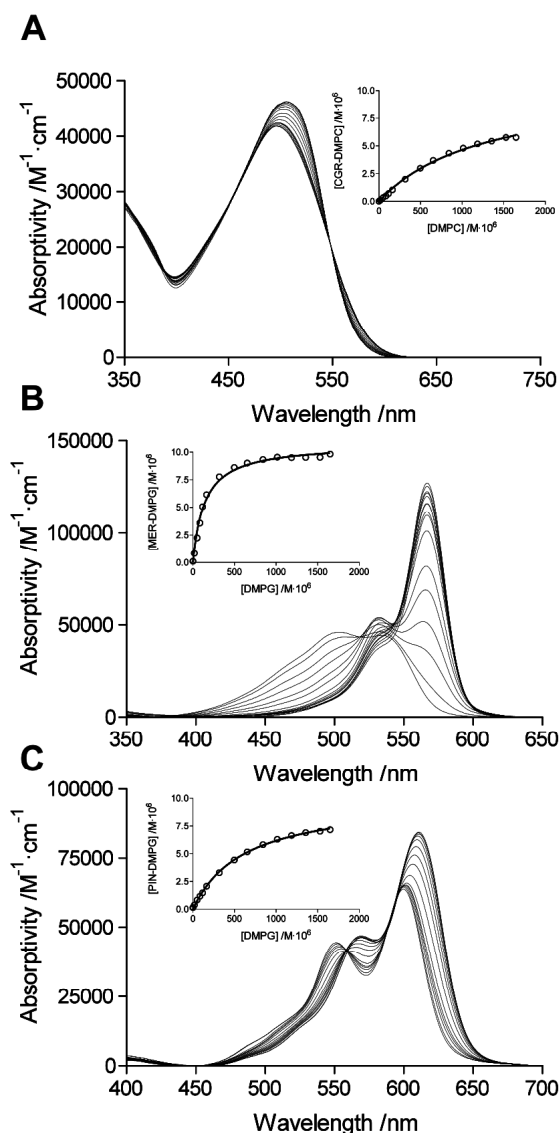


Figs. 2. Reconstruction monomer and dimer absorption spectra of CGR (A), MER (B) and PIN (C) in 10 mM of TRIS buffer at pH7.5 obtained from theoretical values of molar absorptivities at any wavelength. Deconvolution of spectrums represent the sum of three (MER and PIN) or four (CGR) Gaussian curves

In MER spectra, no isosbestic points are observable; the lack of isosbestic point is probably due to equilibrium between free monomer and dimer species, and the dye associated to the liposome bilayer. For MER, an isosbestic point is only detectable at high DMPC concentration where the dimer/monomer equilibrium is highly displaced towards the monomeric form and a new equilibrium between free and DMPC bound monomer is favored, thus resulting in the appearance of an isosbestic point at 540.0 nm.

The general increase in the absorbance values at increasing DMPC concentrations indicates that a larger number of the dye molecules are taken up by DMPC liposomes.

Dye association to liposomes involves an hyperchromic effect accompanied by hyperchromic shift.



Figs. 3. Visible absorption spectrum of $1.0 \cdot 10^{-6}$ M dye in the presence of increasing concentrations of DMPC (from 0 to 1.7 mM). Inset, dye-liposome binding saturation curves; CGR-DMPC (A), MER-DMPC (B) and PIN-DMPC (C) saturation curves in 10 mM TRIS buffer at pH7.5 and 25°C

The shift to the red indicates that dye chromophores become located in a less polar environment, the liposome bilayer. Accordingly, the hydrocarbon core of liposome phospholipids has a dielectric constant of $\sim 2-5$ whereas that of the water solution is of ~ 80 .

The similarity between the absorption spectra of the dyes as free monomer or bound to liposomes supports that these dyes were principally incorporated into liposomes in a monomeric form and suggests the establishment of a new equilibrium between free and bounded monomer.

The inset in Figs. 3 shows dye-liposome binding saturation curves. From the plots, K_A^I values of 1290, 141.5 and $620.9 \text{ M}^{-1} \cdot 10^{-6}$ were obtained for CGR, MER and PIN, respectively. These values indicate that dye affinity to liposome follows the gradation:

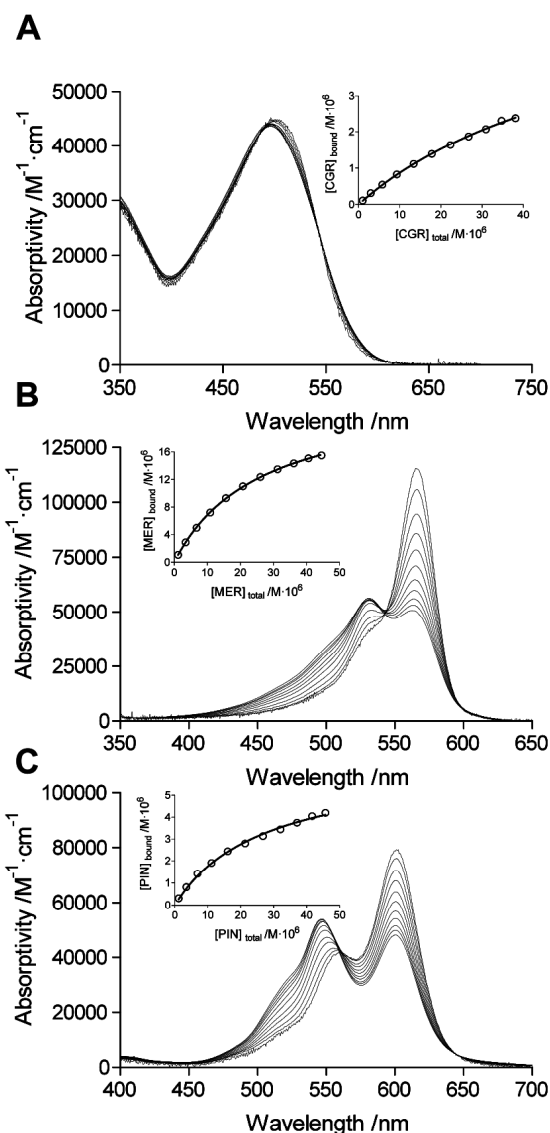
MER>PIN>CGR being high for MER and lower for CGR. Negative ΔG^I values are illustrative of the dyes tendency to associate to liposomes (Table II).

TABLE II
VALUES OF MONOMER-DIMER DYE EQUILIBRIUM

	Congo Red	Mero-cyanine	Pina-cyanol
$K_A^I / M^{-1} \cdot 10^{-6}$	1290	141.5	620.9
$B_{max}^I / M \cdot 10^{-6}$	10.63	10.76	10.01
<i>DMPC-DYE</i>			
$\Delta G^I / kJ \cdot mol^{-1}$	-17.75	-12.27	-15.93
λ_{isos} / nm	460.0 (548.0)	542.5 ^a	559.0
$K_A^{II} / M^{-1} \cdot 10^{-6}$	61.94	26.23	28.07
$B_{max}^{II} / M \cdot 10^{-6}$	6.257	24.76	6.626
$\Delta G^{II} / kJ \cdot mol^{-1}$	-10.22	-8.094	-8.262
<i>DYE_{bound}</i>	~460-		
λ_{isos} / nm	490 ^b (548.0)	542.5	559.0
n	0.0626	0.2476	0.0663
n^{-1}	15.97	4.04	15.08
$\lambda_{max}^{bound} / nm$	506.5	566.0	611.5
$\Delta \lambda_{max}^{mon-bound} / nm$	-8.0	-31.5	-12.5
$E_T^{bound} / kJ \cdot mol^{-1}$	236.18	211.35	195.63

The interaction of DMPC liposomes with dyes was studied at a constant DMPC concentration (0.1 mM) and at dye concentrations ranging from 0 to $5 \cdot 10^{-5}$ M (see Figs. 4). When the dyes are adsorbed on the liposome bilayer the absorption of the most red-shifted peak shows a bathochromic shift and undergoes an E_T reduction (Table II). Isosbestic points of 542.5 and 559.0 are observed for MER and PIN, respectively indicating a dynamic process between two species. In the case of CGR, the low association of the dye in our experimental conditions complicated an accurate determination of the isosbestic point around 460 nm but the differential spectra between free and bound dye allowed detection of the secondary isosbestic point (548.0 nm).

The inset in Figs. 4 shows the binding saturation curves. From the plots, K_A^{II} values of 61.94, 26.23 and $28.07 M^{-1} \cdot 10^{-6}$ were obtained for CGR, MER and PIN, respectively (Table II).



Figs. 4. Visible absorption spectrum of 0.1mM DMPC in the presence of increasing concentration of dye (from 0 to $5 \cdot 10^{-5}$ M). Inset, dye-liposome binding saturation curves; CGR (A), MER (B) and PIN (C) binding saturation curves in 10mM TRIS buffer at pH7.5 and 25°C

Negative ΔG^{II} values indicate a spontaneity of association process. Maximal binding values (B_{max}^{II}) for MER are 4-fold higher than for PIN or CGR indicating a higher MER tendency for association to liposomes. From B_{max}^{II} , the number of sites of union (n) can be determined ($B_{max}^{II} = n \cdot [DMPC]$); in saturation conditions, only 4 molecules of DMPC are necessary to fix a molecule of MER whereas 16 molecules of DMPC are necessary in the cases of CGR and PIN (Table II).

III.3. Dye Localization in Liposome Bilayer

The dyes may be adsorbed on the bilayer surface oriented near the surface or deeply trapped in the hydrocarbon core. It exists a direct relationship between the wavenumber of the maximal absorbance peak and the

Bayliss function (f_B) of the refractive index (n_s) of the solvent where the dye is localized:

$$f_B = \frac{n_s^2 - 1}{2n_s^2 + 1} \quad (8)$$

In order to determine the dyes localization in the liposome bilayer, the dye spectra in different solvents were determined and the plots of wavelength vs Bayliss function were obtained (see Fig. 5).

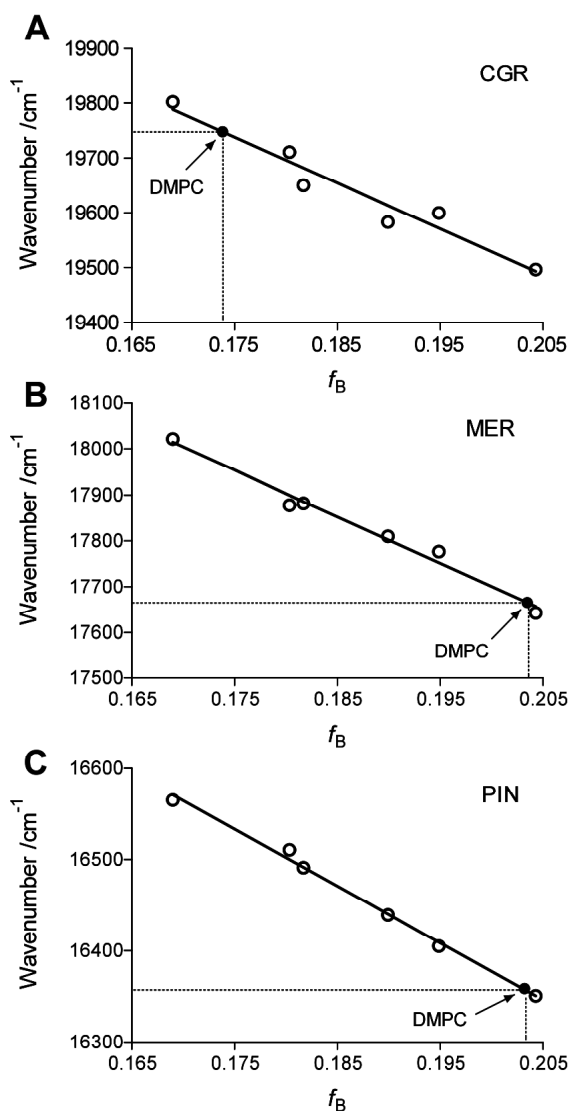
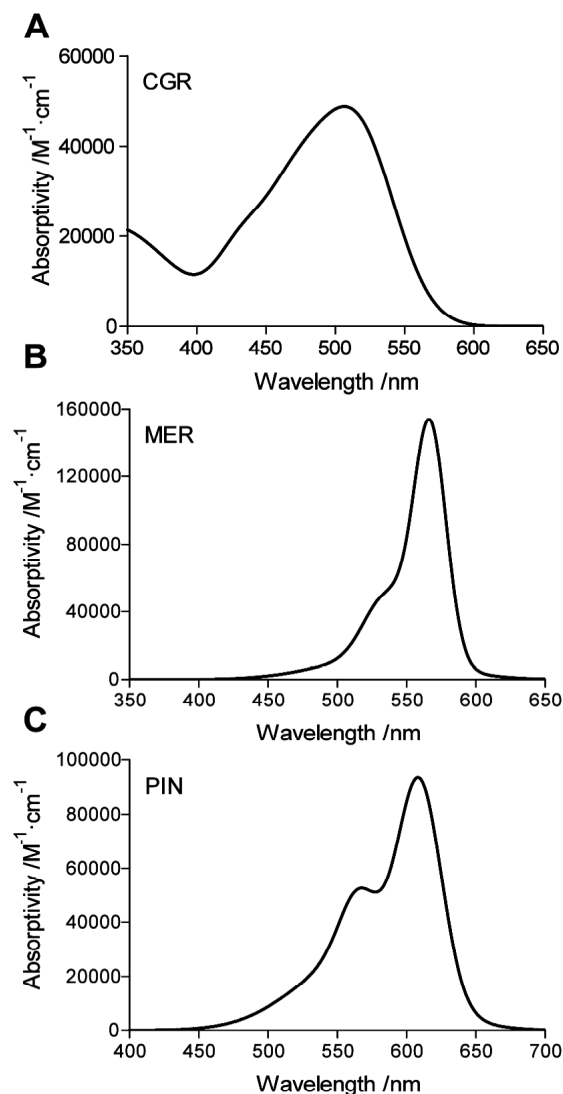


Fig. 5. Dye localization in liposome bilayer using Bayliss plot for CGR (A), MER (B) and PIN (C). Solvents used are from left to right: methanol, acetone, ethanol, 1-propanol, 1-butanol and 1-octanol

Interpolation of maximal absorbance peak of bound dye (Figs. 6) allows to assess the polarity of the dyes environment and therefore to infer the localization of these molecules in the liposome bilayer. As observed in Figs. 5, the n values measured for MER ($n=1.4245$) and PIN ($n=1.4237$) are closely similar and higher than for CGR ($n=1.3414$). In other words, MER and PIN are

incorporated in a more hydrophobic context than CGR. These values correspond to the polarity of octanol and a methanol-ethanol mixture respectively. These n values indicate a localization of MER and PIN in a inner region of the liposome bilayer probably trapped in hydrocarbon core whereas CGR would be localized in a polar zone, likely in contact with the liposome surface.



Figs. 6. Reconstruction bounded absorption spectra of CGR (A), MER (B) and PIN (C) in 10 mM of TRIS buffer at pH7.5 obtained by difference of spectra from the theoretical values of molar absorptivities at any wavelength. Deconvolution of spectrums represent the sum of three (MER and PIN) or four (CGR) Gaussian curves

IV. Conclusion

The present data shows that dyes in study interact with DMPC membranes. The transfer of the dye from bulk water (where dyes are in equilibrium between monomer and dimer state) to liposome bilayer affects its spectral properties leading to a bathochromic shift of the wavelength of maximal peak. Such shifts were interpreted as the passage of the dye chromophore from a polar medium (aqueous medium) to a relatively apolar

environment (liposome bilayer). Dye incorporation to liposome leads to a new equilibrium between the bulk species and bounded molecules. Interpolation of maximal wavelength of bounded species in lineal plot of dyes in different solvents allows determine the micro-environment of the dye embedded into DMPC bilayers and localize each dye in a respective area of the liposome membrane. All these dyes properties should be carefully considered when using these molecules as optical probes to analyze protein-membrane interactions.

Acknowledgment

We thank S. J. Saupe from IBGC (Bordeaux, France) for his helpful suggestions and Joan Estelrich from the UB for the use of the equipments. This work was supported by grant 2009-SGR 760 from AGAUR. SV has been granted with an ICREA Academia award.

References

- [1] S. Nir, J.L. Nieva, Interactions of peptides with liposomes: pore formation and fusion, *Prog. Lipid. Res.* 39, March 2000 (Issue 2), Pages 181-206.
- [2] J.L. Nieva, A. Agirre, et al., Mechanisms of membrane permeabilization by picornavirus 2B viroporin, *FEBS Lett.* 552 September 2003, (Issue 1), Pages 68-73.
- [3] G. Beschiaschvili, J. Seelig, *Biochemistry* 29, December 1990, (Issue 49), Pages 10995-11000.
- [4] M. Hoebeke, X. Damoiseau, et al., Fluorescence, absorption and electron spin resonance study of bacteriochlorin a incorporation into membrane models, *Biochim Biophys. Acta* 1420 (1999), (Issue 1-2), Pages 73-85.
- [5] G.P. Gorbenko, Bromothymol blue as a probe for structural changes of model membranes induced by hemoglobin, *Biochim. Biophys. Acta* 1370, March 1998, (Issue 1), Pages 107-118.
- [6] B. Kurganov, M. Doh, et al., Aggregation of liposomes induced by the toxic peptides Alzheimer's Abetas, human amylin and prion (106-126): facilitation by membrane-bound GM1 ganglioside, *Peptides* 25, February 2004, (Issue 2), Pages 217-232.
- [7] R. Kayed, Y. Sokolov, et al., Permeabilization of lipid bilayers is a common conformation-dependent activity of soluble amyloid oligomers in protein misfolding diseases, *J. Biol. Chem.* 279, November 2004, (Issue 45), Pages 46363-46366.
- [8] M. Bokvist, F. Lindstrom, et al., Two types of Alzheimer's beta-amyloid (1-40) peptide membrane interactions: aggregation preventing transmembrane anchoring versus accelerated surface fibril formation, *J. Mol. Biol.* 335, January 2004, (Issue 4), Pages 1039-1049.
- [9] C. Ege, K.Y. Lee, Insertion of Alzheimer's A beta 40 peptide into lipid monolayers, *Biophys. J.* 87, September 2004, (Issue 3), Pages 1732-1740.
- [10] A. Relini, S. Torrasa, et al., Monitoring the process of HypF fibrillization and liposome permeabilization by protofibrils, *J. Mol. Biol.* 338, May 2004, (Issue 5), Pages 943-957.
- [11] R. Lahdo, S. Coillet-Matillon, et al., The amyloid precursor protein interacts with neutral lipids, *Eur J. Biochem.* 269, April 2002, (Issue 46), Pages 2238-2246.
- [12] C.M. Yip, J. McLaurin, Amyloid-beta peptide assembly: a critical step in fibrillogenesis and membrane disruption, *Biophys. J.* 80, March 2001, (Issue 3), Pages 1359-1371.
- [13] J.J. Kremer, D.J. Sklansky, et al., Profile of changes in lipid bilayer structure caused by beta-amyloid peptide, *Biochemistry* 40, July 2001, (Issue 29), Pages 8563-8571.
- [14] R. Sabate, M. Gallardo, et al., Location of Pinacyanol in Micellar Solutions of N-Alkyl Trimethylammonium Bromide Surfactants, *J. Colloid Interface Sci.* 233, January 2001, (Issue 2), Pages 205-210.
- [15] C. Sato, J. Nakamura, et al., A chemometric approach to the estimation of the absorption spectra of dye probe merocyanine 540 in aqueous and phospholipid environments, *J. Biochem.* 127, April 2000, (Issue 4), Pages 603-610.
- [16] D.L. Sackett, J. Wolff, Nile red as a polarity-sensitive fluorescent probe of hydrophobic protein surfaces, *Anal. Biochem.* 167, December 1987, (Issue 2), Pages 228-234.
- [17] N. Kato, J. Prime, et al., Preparation of J-aggregate liposome dispersions and their chromic transformation, *Langmuir* 20, July 2004, (Issue 14), Pages 5718-5723.
- [18] B. Cunderliká, L. Sikurova, Solvent effects on photophysical properties of merocyanine 540, *Chem. Phys.* 263, June 2001, Pages 415-422.
- [19] P. Kaschny, F.M. Goñi, Spectroscopic properties of hydrophobic dyes incorporated into phospholipid bilayers. An application to the study of membrane - surfactant interaction, *J. Colloid Interface Sci.* 160, April 1993, Pages 24-30.
- [20] P. Bilski, T. McDevitt, et al., Merocyanine 540 solubilized as an ion pair with cationic surfactant in nonpolar solvents: spectral and photochemical properties, *Photochem. Photobiol.* 69, June 1999, (Issue 6), Pages 671-676.
- [21] R. Sabate, J. Estelrich, Pinacyanol as effective probe of fibrillar beta-amyloid peptide: comparative study with Congo Red, *Biopolymers* 72, May 2003, (Issue 6), Pages 455-463.
- [22] A. Mishra, R.K. Behera, et al., Cyanines during the 1990s: A Review, *Chem. Rev.* 100, June 2000, (Issue 6), 1973-2012.
- [23] P. Kaschny, F.M. Goni, The components of merocyanine-540 absorption spectra in aqueous, micellar and bilayer environments, *Eur. J. Biochem.* 207, August 1992, (Issue 3), 1085-1091.
- [24] E. Jo, A.A. Darabie, et al., Alpha-Synuclein-synaptosomal membrane interactions: implications for fibrillogenesis, *Eur. J. Biochem.* 271, August 2004, (Issue 15), 3180-3189.
- [25] L. Sikurova, R. Frankova, The effect of albumin on incorporation of merocyanine 540 into phospholipid liposomes, *Gen. Physiol. Biophys.* 13, October 1994, (Issue 5), Pages 393-403.
- [26] R. Sabate, J. Estelrich, Aggregation characteristics of ovalbumin in beta-sheet conformation determined by spectroscopy, *Biopolymers* 67, January 2002, (Issue 2), Pages 113-120.
- [27] W.E. Klunk, R.F. Jacob, et al., Quantifying amyloid beta-peptide (Aβ) aggregation using the Congo red-Aβ (CR-Aβ) spectrophotometric assay, *Anal. Biochem.* 266, January 1999, (Issue 1), Pages 66-76.
- [28] H. Inouye, D.A. Kirschner, A beta fibrillogenesis: kinetic parameters for fibril formation from congo red binding, *J. Struct. Biol.* 130, June 2000, (Issue 2-3), Pages 123-129.
- [29] R. Sabate, J. Estelrich, Determination of the dimerization constant of pinacyanol: Role of the thermochromic effect, *Spectrochim. Acta A* 70, September 2007, Pages 1386-1425.
- [30] R.C. MacDonald, R.I. MacDonald, et al., Small-volume extrusion apparatus for preparation of large, unilamellar vesicles, *Biochim. Biophys. Acta* 1061, (Issue 2), January 1991, Pages 297-303.

Authors' information

* To whom correspondence should be addressed: Salvador Ventura (salvador.ventura@uab.es), Raimon Sabaté (raimon.sabate@uab.cat)
Tel.: + 34 935 812 154; Fax: + 34 935 811 264.

^{1,2,3} Institut de Biotecnologia i Biomedicina. Departament de Bioquímica i Biologia Molecular, Universitat Autònoma de Barcelona AB, E-08193 Bellaterra (Spain).

Multi Transition States for S_N2 Reaction in Intramolecular Processes

Rafik Karaman, Shireen Alfalah

Abstract — The DFT calculation results for ring-closing reactions of eight different ω -bromoalkanecarboxylate anions, 1-8, five different 4-bromobutylamines, 9-13 and four β -aminoethyl chlorides, 14-17 reveal that the intramolecular substitution nucleophilic attack of the nucleophile ($-O^-$ or $-NH_2$) on the electrophilic center ($-(CH_2)-Br$ or $-(CH_2)-Cl$) involves multi-transition states. Further, the results establish that the activation energy ($\Delta\Delta G^\ddagger$) for intramolecular cyclization processes calculated from the higher transition state is strongly correlated with the experimentally intramolecular cyclization rate ($\log k_{intra}$), whereas the difference in the energies of the highest and the lowest energy transition states is found to correlate strongly with the experimental or MM2 calculated strain energy of the reactant or the strain energy difference between the cycle formed and the reactant ($E_{s, Exp}$). The latter result is the first to predict strain energy based on energy barrier. **Copyright © 2010 Praise Worthy Prize S.r.l. - All rights reserved.**

I. Introduction

The chemistry of intramolecular processes has been utilized for the design of chemical models for mimicking the extraordinary efficiency of enzyme catalysis. Both systems are similar in that the reacting centers are held together: in the former by a covalent bond and in the latter by a noncovalent enzyme substrate complex. Therefore, the unraveling of the mechanism of an enzyme catalyzed reaction could be feasible if an appropriate intramolecular process is to be fully investigated. [1]

Significant number of chemical models consist of two reactive moieties to interact in an intramolecular fashion has been designed. Among these is the scholarly proton transfer model advocated by Menger with the rationale that the type of the reaction intermolecular or intramolecular is determined by the distance between the nucleophile and the electrophile, and the activation energy for the process is a function of the distance between them. [2] Other examples include: (1) “near attack conformation” model presented by Bruice on intramolecular lactonization of some dicarboxylic semi esters, [3] (2) “orbital steering” theory presented by Koshland, [4] and, (3) “stereopopulation control” suggested by Cohen to explain the extraordinary rate accelerations in the acid catalyzed lactonization of the trimethyl lock system. [5] Both, the concept of proximity orientation and of strain energy have been invoked for understanding the remarkable accelerations in rate of these enzyme models. The concept of strain energy has been used to understand the remarkable accelerations in rate of some of these enzyme models. Ring-strain energy was commonly assumed to be the sole driving force for the accelerations in rate of five-membered cyclic phosphate and phosphonate relative to their acyclic analogues. [6]

Furthermore, it has been shown that there is a strong relationship between rates and equilibrium constants in intramolecular cyclization reactions, especially those involving the *gem*-dialkyl effect.

Recently, we have been studying the driving force(s) for enhancements in rate of some intramolecular processes that have been used as enzyme models. Using many levels at the DFT method, we researched the behavior for the acid catalyzed lactonization of some hydroxy-acids, [2] proton transfer reactions in Menger’s rigid cycloalkanes system, as well as, in the cleavage reaction of Menger’s aliphatic amide, [2] lactonization of dicarboxylic semi esters (Bruice’s System), [3] and ring-closing reactions of substituted 4-bromobutylamines (Brown’s system) [7] arriving at the following findings: (a) the driving force for rate acceleration in intramolecular processes can be due to either proximity orientation or strain effects, depending on the nature of the system. (b) Rate enhancements in intramolecular reactions are a result of both entropic and enthalpic effects. Additionally, it was found that entropy change is more dominant in flexible systems than in the rigid ones. [8]

Studies by Illuminati, Mandolini and Galli on ring-closing of bi-functional system [9] that covers reactions for the formation of ring sizes in the range of 3-23 atoms [10] involving the formation of lactones, [11] carbocyclic diethylmalonates, [12] cyclic ethers, [13] cyclic N-tosylamines, [14] and cyclic aromatic ketones [15] establish that the ring product is a good model of the transition state for all bifunctional chains except the shortest ones, and the free energy of activation can be estimated from the strain energy of the cyclic product, and the ease of cyclization of long chains is decreased upon the growth of the chain. [16]

In this paper, we disclose the first theoretical study to show linear correlation between energy barrier and ring-strain energy and the first to indicate the existence of multi-transition state in intramolecular S_N2 reactions; the highest transition state reflects activation energy (reaction rate) and the others internal strain energy (E_s).

We have calculated, using B3LYP/6-31G (d, p), B3LYP/aug-cc-pVDZ, B3PW91/cc-pVDZ and B3PW91/cc-pVTZ levels of theory, the kinetic and the thermodynamic properties for ring formation from ω -bromoalkanecarboxylate anions **1-8**, 4-bromobutylamines **9-13** and β -aminoethyl chlorides **14-17** (see Charts 1 and 2).

II. Methods

The DFT calculations were carried out using the quantum chemical package Gaussian-98. [17] MM2 molecular mechanics strain energy calculations were performed using Allinger's MM2 program installed in Chem 3D Ultra 8.0. [18] The starting geometries of all the molecules presented in this study were obtained using the Argus Lab program [19] and were initially optimized at the AM1 level of theory. [17] The calculations were carried with full optimization of all geometrical variables. [20] The global minimum structures of the starting materials in **1-8** were found by conducting rotation of the carboxylate group (C(O)O⁻) around the C-C bond located at α position to the carboxyl group. Similarly, the global minimum structures for the starting geometries in **9-17** were located by rotation of the amino group (NH₂) around the adjacent C₂-C₃ bond (see Chart 1). To avoid results with local minima optimization, frequency calculation were carried out for these systems. An energy minimum (a stable compound or a reactive intermediate) has no negative vibrational force constant. A transition state is a saddle point which has only one negative vibrational force constant. [21] The "reaction coordinate method" [22] was used to calculate the activation energy in systems **1-17**. In this method, one bond length is constrained for the appropriate degree of freedom while all other variables are freely optimized. The activation energy values for ring closing reactions were calculated from the difference in energies of the global minimum structures of ω -bromoalkanecarboxylate anions **1-8** and the first derived transition state (TS₁) of the cyclization reaction, obtained by a decrease in the distance between the carboxylate oxygen (O₁) and the carbon attached to the bromide (C₅) in increments of 0.1Å (see Chart 1). The activation energy values for ring-closing of **9-17** were calculated from the difference in energies of the global minimum structures and the last derived transition state (TS₁), obtained by a decrease in the distance between the amine nitrogen (N₁) and the carbon attached to bromide (C₅) in systems **9-13**, and to chloride (C₃) in systems **14-17**, in increments of 0.1Å (see Chart 1). Verification of the desired reactants and products was accomplished using the "intrinsic reaction coordinate method". [22] The

transition state structures were verified by their only one negative frequency. Full optimization of the transition states was accomplished after removing any constrains imposed while executing the energy profile. The activation energies obtained from the DFT levels of theory for **1-17** were calculated with and without the inclusion of solvent (water). The calculations with the incorporation of a solvent were performed using the integral equation formalism model of the Polarizable Continuum Model (PCM). [23]

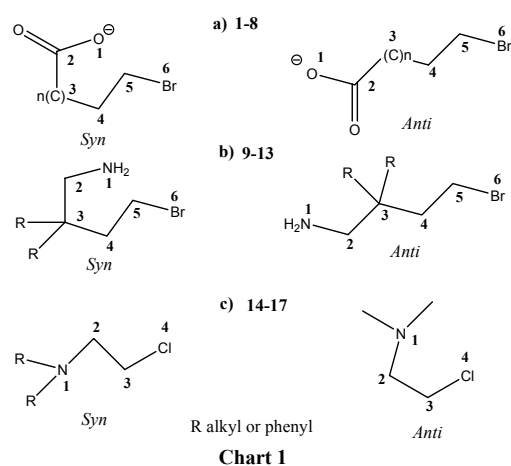


Chart 1: *Syn* and *anti* orientation in systems 1-17

III. Results and Discussion

The global minimum geometries for the derivatives of ω -bromoalkanecarboxylate anions **1-8**, 4-bromobutylamines **9-13** and β -aminoethyl chlorides **14-17** were obtained by rotating either the carboxylate group (COO⁻) around the adjacent C₂-C₃ bond (i.e. variation of the dihedral angle C₂C₃C₄C₅, see Chart 1a) or the amino group (-NH₂) around C₂-C₃ bond (i.e. variation of the dihedral angle N₁C₂C₃C₄ for **9-13**, and N₁C₂C₃Cl₄ for **14-17**, see Charts 1b and 1c), and calculating the conformational energies.

In the DFT calculations of ω -bromoalkanecarboxylate anions **1-8**, two types of conformations in particular were considered: one with the anionic oxygen (O₁) of the carboxylate in the *syn* orientation to the carbon attached to bromide (C₅) and the other with the carboxylate in the *anti* orientation to C₅ (see Chart 1a). It was found that for ω -bromoalkanecarboxylate anions **1-8**, the global minimum structures have a zigzag conformation with the anionic oxygen of the carboxylate group in the *syn* orientation to the electrophilic center (C₅-Br). For 4-bromobutylamines **9-13** and β -aminoethyl chlorides **14-17**, the global minimum structures were these having the amino group in the *syn* orientation to the carbon attached to the halide (see Charts 1b and 1c).

III.1. Energy Profile Calculations

We have conducted a reaction coordinate method to

calculate the activation energy for ring-closing reactions of **1-8** (Chart 2). This was accomplished by a decrease in the distance between the carboxylate oxygen (O_1) and the carbon attached to bromide (C_5) in increments of 0.1 \AA . The calculated energy profile for the reaction pathway, from reactants (GM) to products (P), indicates the presence of many conformations, having one negative frequency, in a wide range.

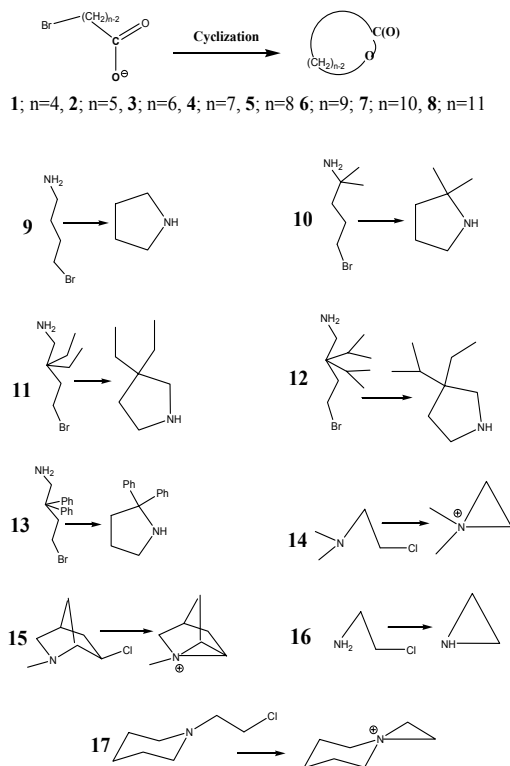


Chart 2: Ring-closing reactions for ω -bromoalkancarboxylate anions 1-8, bromobutylamines 9-13 and β -aminoethyl chlorides 14-17

In order to demonstrate beyond reasonable doubt that these results are not artifacts of the way in which the reaction coordinates were constructed. System **2** was selected for further investigations. Four different levels of theory, B3LYP/6-31G (d, p), B3LYP/cc-pVDZ, B3LPW91/cc-pVDZ and B3LPW91/cc-pVTZ were exploited to verify the existence and the nature of the multi-transition state zone (MTSZ). The calculation results emerged indicate that the intramolecular ring-closing reaction for **2** has a broad range consists of many transition states having different energies (MTSZ). It should be emphasized that B3LPW91/cc-pVDZ and B3LPW91/cc-pVTZ methods have been shown to predict frequencies in excellent manner. [24]

It is worth noting that the minimization procedure in Gaussian, starting from certain guess geometry, always leads to the same transition state. In fact, the procedure followed in this study is the following: the reaction coordinates going from the reactant to product was decremented with a step-size of 0.05 \AA . Figure 1 shows typical energy profile (plot of energy vs. reaction progress) for a ring-closing reaction of ω -bromoalkancarboxylate anion. As this figure

shows, a plateau is observed in the range marked with a star symbol. It is proposed that this plateau consists of the MTSZ. Each of the marked geometries in Figure 1 was subjected to transitional state optimization using Gaussian-98 software. The results show that each of these geometries is indeed a transition state (only one negative frequency).

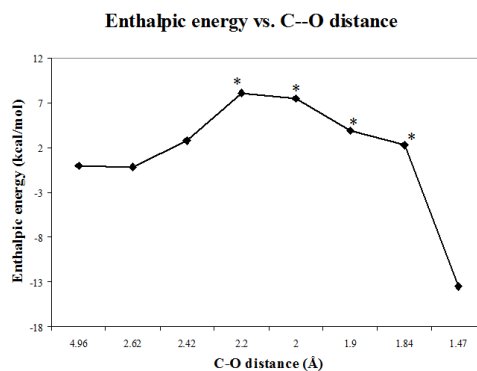


Fig. 1. Plot of enthalpic energy vs. C---O distance for system 5. The MTSZ zone consists of the marked points with the star symbol

To shed light on this observation, the region from GM to P for systems **1-8** was intensively investigated. “Mid-way” conformations in the MTSZ, between TS_1 (the first TS) and TS_L (the last TS) were constructed by decreasing the distance between the anionic oxygen (O_1) and the carbon attached to bromide (C_5) in increments of 0.05 \AA while maintaining the other variables to be fully optimized. The results reveal that the MTSZ commences when the distance between O_1 and C_5 reaches 2.2 \AA and vanishes when the distance between the two reactive centers approaches 1.82 \AA . The first conformation along the MTSZ has the highest energy among all conformations obtained and the one achieved by the end of the zone has the lowest (see Chart 3a). The geometries of the transition states within the MTSZ were re-optimized after removing all constraints imposed during the reaction coordinate calculations and were verified by their only one negative frequency in a similar manner to that conducted in the reaction coordinate calculations.

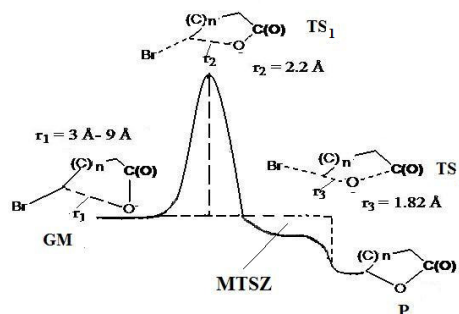


Chart 3a: Energy profile for ring-closing reactions of ω -bromoalkancarboxylate anions 1-8. GM, TS_1 , TS_L and P are global minimum, first transition state, last transition state and product, respectively. r_1 , r_2 and r_3 are O_1 - C_5 distance values in GM, TS_1 and TS_L , respectively. MTSZ is the multi-transition state zone. There is no minimum between TS_1 and TS_L .

Viewing the vibrational motion of the optimized conformations having one negative frequency, achieved within the MTSZ, indicates that the first conformations in the MTSZ, with O₁---C₅ distance around 2.2 Å (TS₁), are completely governed by breaking (C₅-Br) and forming bonds (O₁-C₅) as evident from the mode and the direction of the frequency vectors. On the other hand, the frequency vector map for the reaction coordinate(s) of the last conformations in the MTSZ (O₁---C₅ distance of 1.82 Å, TS_L) reveals a change in the mode and direction of the vectors from stretching (as for TS₁) to mainly non-stretching" vibrations of the atoms surrounding the two reactive centers. These vibrations are indicative to strain effects of the cycle being formed. Figures 2a and 2b show the vibrational movements of the atoms along the MTSZ in systems **2** and **5**, respectively. It should be noted that the more intense vectors after the change in the mode of the reaction coordinate in system **5**

compared with system **2** is due to the superiority of the strain effects in the eight-membered ring over that in the five-membered ring.

The fact that there is no minimum structure found between TS₁ and TS_L and all entities in this range have one negative frequency establishes that TS_L is dominated by coordinate(s) other than those involved in the transition vector for TS₁. This is evident from the change in the torsion angle C₂-O₁-C₅-Br₆ when passing from TS₁ to TS_L (see Table I). The calculated B3LYP/6-31G (d,p) data of the energy profiles (GM-TS₁-TS₂-P) for **2-8** is listed in Table I.

In order to examine if our observation of the multi-transition state range is valid for S_N2 reactions in other intramolecular processes, we have conducted the same calculations for ring-closing reactions of systems **9-17** (Chart 2).

TABLE I
ENERGY PROFILE PROPERTIES FOR RING-CLOSING REACTIONS OF SYSTEMS **2-8** AS CALCULATED BY B3LYP/6-31G (D, P) IN THE GAS PHASE

System 2						
O ₁ -C ₅ Distance in Å	C ₅ -Br ₆ Distance in Å	Attack Angle (α, O ₁ -C ₅ -C ₄ , degree)	Angle C ₂ O ₁ C ₅ Br ₆ , degree	Frequency Cm ⁻¹	Enthalpy in Hartree	Entropy Cal/Mol-Kelvin
2.89 (GM)	2.00	72.14	148.83	minimum	-2878.25897	91.91
2.62	2.07	81.52	139.51	minimum	-2878.25789	94.86
2.42	2.13	84.08	167.48	minimum	-2878.25652	91.47
2.22 (TS ₁)	2.39	87.68	178.17	-233.2109	-2878.25444	87.91
2.00	2.74	93.36	-166.97	-354.1700	-2878.25833	88.27
1.90	2.89	95.95	-159.90	-325.2909	-2878.26386	88.40
1.82 (TS _L)	3.15	100.30	-152.82	-260.5329	-2878.26943	88.56
System 3						
O ₁ -C ₅ Distance in Å	C ₅ -Br ₆ Distance in Å	Attack Angle (α, O ₁ -C ₅ -C ₄ , degree)	Angle C ₂ O ₁ C ₅ Br ₆ , degree	Frequency Cm ⁻¹	Enthalpy in Hartree	Entropy Cal/Mol-Kelvin
2.75 (GM)	2.05	95.58	119.00	minimum	-2917.57467	98.10
2.62	2.07	96.68	125.78	minimum	-2917.57430	97.17
2.42	2.12	97.47	131.76	minimum	-2917.57197	96.67
2.22 (TS ₁)	2.39	100.10	144.82	-204.7449	-2917.56776	94.33
2.00	2.83	102.15	-164.07	-321.8370	-2917.56605	94.93
1.90	3.00	105.83	-155.37	-298.4870	-2917.57629	95.32
1.83 (TS _L)	3.11	107.38	-144.56	-238.2920	-2917.58100	95.26
System 4						
O ₁ -C ₅ Distance in Å	C ₅ -Br ₆ Distance in Å	Attack Angle (α, O ₁ -C ₅ -C ₄ , degree)	Angle C ₂ O ₁ C ₅ Br ₆ , degree	Frequency Cm ⁻¹	Enthalpy in Hartree	Entropy Cal/Mol-Kelvin
4.28 (GM)	2.01	30.35	138.05	minimum	-2956.88784	106.65
2.62	2.06	82.64	36.37	minimum	-2956.88450	100.17
2.30 (TS ₁)	2.18	87.99	82.64	-35.09100	-2956.88058	97.06
2.10	2.56	95.65	100.80	-366.6250	-2956.87950	99.22
1.83 (TS _L)	3.21	106.92	50.85	-198.7480	-2956.89600	99.44

System 5						
O ₁ -C ₅ Distance in Å	C ₅ -Br ₆ Distance in Å	Attack Angle (α , O ₁ -C ₅ -C ₄ , degree)	Angle C ₂ O ₁ C ₅ Br ₆ , degree	Frequency Cm ⁻¹	Enthalpy in Hartree	Entropy Cal/Mol-Kelvin
4.96 (GM)	2.01	72.77	155.60	minimum	-2996.20269	112.28
2.62	2.06	83.95	-76.80	minimum	-2996.20291	105.53
2.42	2.11	86.29	-86.73	minimum	-2996.19819	105.75
2.20 (TS _i)	2.26	89.80	-89.23	-179.7100	-2996.18974	103.34
2.00	2.83	97.00	-107.12	-346.0050	-2996.19071	105.04
1.90	3.00	99.65	-115.83	-308.9469	-2996.19644	105.14
1.84 (TS _L)	2.92	100.65	-122.04	-259.4555	-2996.19900	105.05

System 6						
O ₁ -C ₅ Distance in Å	C ₅ -Br ₆ Distance in Å	Attack Angle (α , O ₁ -C ₅ -C ₄ , degree)	Angle C ₂ O ₁ C ₅ Br ₆ , degree	Frequency Cm ⁻¹	Enthalpy in Hartree	Entropy Cal/Mol-Kelvin
6.18 (GM)	2.00	20.80	150.53	minimum	-3035.51576	125.00
2.62	2.06	94.73	130.81	minimum	-3035.51780	109.35
2.42	2.10	93.24	141.64	minimum	-3035.51460	114.01
2.21 (TS _i)	2.21	95.64	152.07	-46.69500	-3035.50774	108.23
2.00	2.95	106.01	-144.33	-318.2489	-3035.50559	112.60
1.90	3.10	109.99	-159.56	-288.2429	-3035.51122	111.60
1.83 (TS _L)	3.51	105.37	4.07	-102.8270	-3035.51800	110.26

System 7						
O ₁ -C ₅ Distance in Å	C ₅ -Br ₆ Distance in Å	Attack Angle (α , O ₁ -C ₅ -C ₄ , degree)	Angle C ₂ O ₁ C ₅ Br ₆ , degree	Frequency Cm ⁻¹	Enthalpy in Hartree	Entropy Cal/Mol-Kelvin
6.86 (GM)	2.00	54.30	11.94	minimum	-3074.83125	129.91
2.62	2.06	85.66	148.05	minimum	-3074.83990	119.91
2.40	2.11	89.39	165.11	minimum	-3074.83637	119.39
2.21 (TS _i)	2.24	90.93	-175.50	-155.0980	-3074.82946	115.00
2.00	2.82	94.49	-131.99	-348.7739	-3074.82972	115.89
1.90	3.02	103.27	-132.67	-311.2980	-3074.83508	116.27
1.81 (TS _L)	3.19	106.12	-149.13	-208.5859	-3074.84200	116.91

System 8						
O ₁ -C ₅ Distance in Å	C ₅ -Br ₆ Distance in Å	Attack Angle (α , O ₁ -C ₅ -C ₄ , degree)	Angle C ₂ O ₁ C ₅ Br ₆ , degree	Frequency Cm ⁻¹	Enthalpy in Hartree	Entropy Cal/Mol-Kelvin
8.52 (GM)	1.99	21.54	144.73	minimum	-3114.14734	137.04
2.62	2.39	99.97	-142.14	minimum	-3114.12284	109.92
2.40	2.13	92.78	-161.50	minimum	-3114.15149	126.28
2.15 (TS _i)	2.39	97.85	-142.94	-325.8110	-3114.14569	121.72
1.82 (TS _L)	3.37	108.10	-169.25	-139.7409	-3114.15900	123.25

For the numbering of the atoms see Chart 1

The DFT calculation results for the intramolecular ring-closing reactions of **9-17** reveal a broad region of one negative frequency. This region starts with the lowest energy TS conformation (TS_i) in the range of 2.0 Å - 2.2 Å, whereas the highest energy transition state conformation (TS_L) is achieved when the distance between the two reactive centers is in the range of 1.8 Å - 2.0 Å (see Chart 3b). This is similar to that seen with systems **1-8** however; the order of the highest and lowest

energy transition states is reversed. Further, in contrast to the energy profiles of **1-8**, viewing the conformations along the MTSZ for **9-17** reveals that the reaction coordinate at the beginning of the zone is characterized mainly by the presence of vibrational vectors that are characteristic to strain energy and that at the end of the zone belongs to stretching motions indicative to breaking and forming bonds (see Figures 2c).

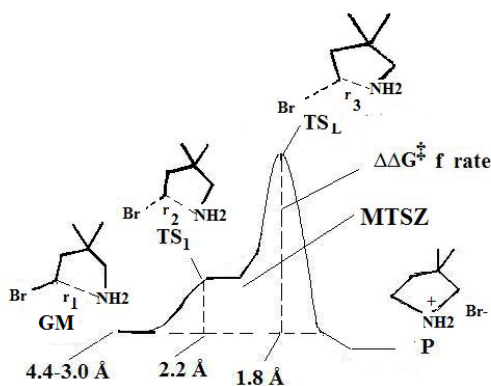
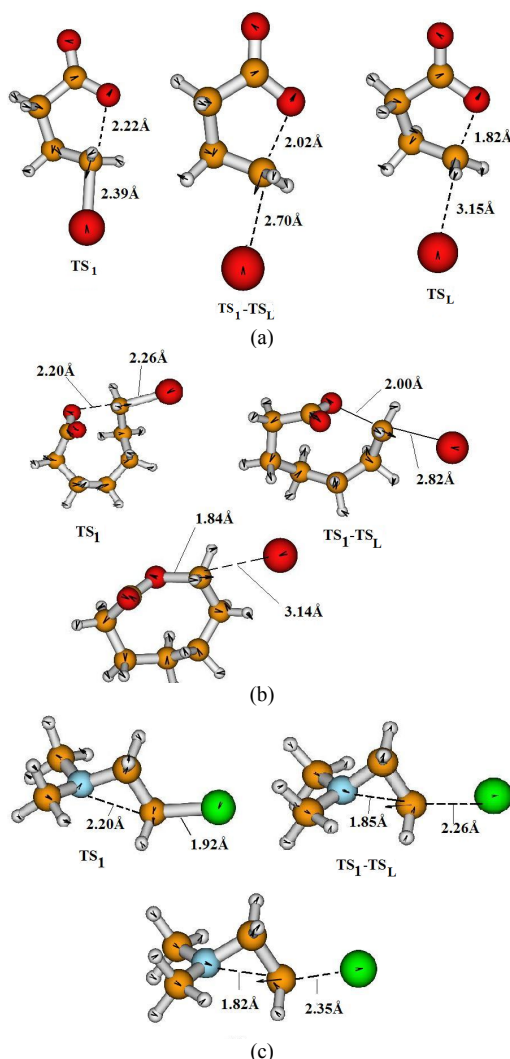


Chart 3b: Energy profile for ring closing-reactions of **9-13**. GM, TS₁, TS_L and P are global minimum, first transition state, last transition state and product, respectively. r_1 , r_2 and r_3 are the N₁-C₅ distance values in GM, TS₁ and TS_L, respectively. MTSZ is the multi transition state zone. There is no minimum between TS₁ and TS_L.



Figs. 2. (a) Frequency vectors map in the energy profile for ring-closing reaction of **2**. TS₁, TS_L and TS₁-TS_L are first transition state, last transition state and mid - way transition state, respectively. (b) Frequency vectors map for the energy profile of system **5**. TS₁, TS_L and TS₁-TS_L are first transition state, last transition state and mid - way transition state, respectively. (c) Frequency vectors for the energy profile of **14**. TS₁, TS_L and TS₁-TS_L are first transition state, last transition state and mid way transition state, respectively

To test if the phenomenon of the multi-transition state range is unique to S_N2 reaction in intramolecular processes or could be general for intermolecular S_N2 processes, the energy profiles for the intermolecular counter parts of systems **2**, **3**, **9** and **10** were calculated by DFT methods. The calculation results indicate clearly that there is only one transition state along the reaction pathway in all systems studied. For example the transition state for **9** and **10** are achieved when the distance between the two reactive centers (C---N) is 2.0 Å. This result suggests that the multi-transition states zone is a result of a reaction coordinate stemming from vibrational motions of the ongoing formation of the heteroatom cycle.

III.2. Analysis of the Multi-Transition State Zone (MTSZ)

In the reaction coordinate of O₁ approaching C₅ in systems **1-8**, when O₁ and C₅ are separated and not yet interacting (as in the reactants) the potential energy is at minimum, when O₁ and C₅ come together in a reactive collision, the potential energy rises as the atoms (mainly O₁ and C₅) begin to execute the motion that will carry over to the final destination (formation of the cyclic product). At some configuration the potential passes through a maximum, and then falls until reaching a minimum with the separated products (cyclic ring and bromide anion).

According to the “principle of least nuclear motion”, elementary reactions will be favored that involve the least change in atomic position and electronic configuration. [25]

Thus, in ordinary reactions at each point of the reaction coordinate line (such as a nucleophile approaching towards an electrophile) there are motions off the line correspond to vibrations other than the single one that is carrying the reactants to products (Nu---E approach). These motions are all ordinary vibrations, having nothing to do with the reaction and proceeding quite independently of it. If we assume that the reaction coordinate is perpendicular to each of the other vibrations, so that if we were to leave the reaction coordinate path and follow the potential energy surface in the direction of some other modes, the energy would always go up.

In the case of ring-closing reactions of **1-8**, in addition to ordinary vibrations, there are other motions belong to strain effects of the cycle being formed. In the energy profile of O₁ approaching C₅, the trend of the potential energy, in the region GM to TS₁, resembles that of any ordinary reaction coordinate. However, on passing TS₁, the reaction coordinate switches mode as a result of other motions effects (strain effects) that take place once the process of stretching bonds (C---Br) reaches a level by which the other motions are more dominant. The new mode of the reaction coordinate continue going on until reaching the last transition state of the MTSZ (TS_L). At this point, the motions related to strain effects vanish and

the potential energy surface goes back to the direction by which the approach of O₁ and C₅ starts. The length of the MTSZ and the difference in magnitude of TS₁ and TS_L are determined upon the nature of the ring being formed.

Mapping of the frequency vectors for the energy profile for system **14** indicates that at the beginning of the one negative frequency zone (MTSZ) the reaction coordinate takes a direction by which the influence of the other motions (strain effects) are much more dominant than the stretching motion responsible for taking the reactants to the desired products. At the end of the MTSZ, these strain motions decline and the reaction coordinate switches mode to the direction by which the stretching vibrations have the superiority to carry the reactants to products (see Figures 2c).

It should be indicated that Bickelhaupt and coworkers have published few studies on nucleophilic substitution (S_N2) at carbon and silicon and have showed that the nature of the SN2 reaction barrier is in essence steric but can be modulated by electronic factors. Further, they found that increasing the steric demand of the that substituent around the silicon changes the mechanism from a single-well PES to a double-well PES via a triple-well PES (with a pre and a post TS before and after the transition complex intermediate) [26] On the other hand, Houk and coworkers have observed similar phenomenon to that found by us when calculating 1,3 dipolar cycloadditions. [27]

III.3. Strain Energy Calculations for 1-8

Since strain energy is an enthalpic factor we executed correlations of $\Delta\Delta H_{\text{Exp}}^{\ddagger}$ and DFT calculated $\Delta\Delta H^{\ddagger}$ with $E_{\text{s Exp}}$ (Table II) and found that the curves obtained are composed of two straight lines that have a significantly different slopes (see Figure 3a and equations (1) and (2) in Table III). However, when the calculated energy difference values of TS₁ and TS_L ($\Delta\Delta H_{\text{TS1-TSL}}$, with and without the inclusion of water as a solvent) were plotted against $E_{\text{s Exp}}$ only one line with high correlation coefficient was obtained (see Figure 2b and equations (3)-(6) in Table III). Equations (3)-(6) could be summarized in a simple expression as shown in eq. (7) where $E_{\text{s calc}} = \Delta\Delta H_{\text{TS1-TSL}}$:

$$E_{\text{s calc}} = A E_{\text{s Exp}} + C \quad (7)$$

where A is the slope and C is a constant

When comparing the values of the slopes in equations 1-2 with that obtained from the plot of the calculated enthalpic energy difference in water, $\Delta\Delta H_{\text{TS1-TS2/H2O}}$ vs. $E_{\text{s Exp}}$, (eq. (4) or (5) in Table III) we find that the slope values for the latter are almost identical to that obtained for the cyclization reactions forming medium-sized rings.

The discrepancy in the slope values for the formation of the different rings may be attributed to solvation effects which are more dominant in the cyclization reactions leading to medium-sized rings as evident from the slopes values of the calculated enthalpic energies in

the gas phase (-0.47, see eq. (3) in Table III) vs. those calculated with the inclusion of water (-0.85, eq. (4) in Table III).

TABLE II
EXPERIMENTAL AND CALCULATED THERMODYNAMIC AND KINETIC PROPERTIES FOR RING-CLOSING REACTIONS OF Ω -BROMOALKANECARBOXYLATE ANIONS **1-8**

System	B3L/GP $\Delta\Delta H_{\text{TS1-TSL}}$	B3L/H ₂ O $\Delta\Delta H_{\text{TS1-TSL}}$	B3Lcc/H ₂ O $\Delta\Delta H_{\text{TS1-TSL}}$	Experiment al $E_{\text{s}}^{10-16, 28}$
1	1.47	1.47	3.28	23.3
2	9.41	9.41	10.96	7.7
3	8.31	8.31	13.74	9.5
4	9.68	9.68	12.18	10.7
5	5.81	5.81	11.87	11.9
6	6.65	6.65	12.47	11.2
7	7.87	7.87	18.47	8.4
8	8.35	8.35	18.83	7.2

TS₁ and TS_L refer to first and last transition states, respectively. The unit for $\Delta\Delta H_{\text{TS1-SM}}$, $\Delta\Delta G_{\text{TS1-SM}}$, $\Delta\Delta H_{\text{TS1-TSL}}$, $\Delta\Delta H_{\text{SM-P}}$ and Experimental E_{s} is kcal/mol. The unit for $\Delta S_{\text{TS1-SM}}$ is Cal/Mol-Kelvin. B3L/GP refers to calculated by B3LYP/6-31G (d, p). B3L/H₂O and B3Lcc/H₂O refer to calculated by B3LYP/6-31G (d, p) and B3LYP/cc-pVDZ, respectively

This result is supported by the correlation results of $E_{\text{s Exp}}$ with $\Delta\Delta H_{\text{P-SM/B3L/H2O}}$ that gave a correlation coefficient of $R = 0.95$ (see eq. (6) in Table III).

Another explanation to this phenomenon might be attributed to the discrepancy in the proximity orientation of the nucleophile (C(O)O⁻) to the electrophile (CH₂-Br) in the two different systems (see values of O₁---C₅ in Table I).

III.4. Strain Effects vs. Proximity Orientation

To examine whether the discrepancy in rates for processes **1-8** stems from proximity orientation (difference in the distance between the two reactive centers) or due to strain effects we executed correlations of the B3LYP/6-31G(d, p) calculated O₁-C₅ distance in the global minimum structures for **1-8** (2.63 Å, 2.89 Å, 2.75 Å, 4.28 Å, 4.96 Å, 6.18 Å, 6.68 Å and 8.52 Å, respectively) with $\log k_{\text{intra}}$. The correlation results indicate a relatively poor correlation ($R^2 = 0.77$).

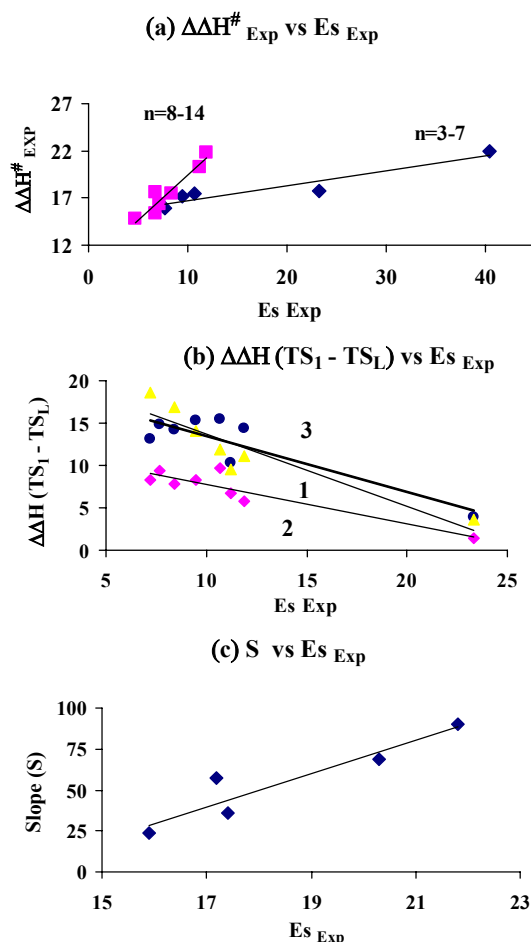
In order to shed light on what constituent factors are affected by the strain effect, we calculated the change in the value of the attack angle α (O₁/C₅/ α -C₄, Chart 1a) and the change in the distance between the two reactive centers ($r = \text{O}_1\text{-C}_5$ distance) as a function of ΔH (enthalpic energy) since both parameters (r and α) were reported to play an important role in the reaction rates of intramolecular systems. [2] [8]

It should be noted that the values of ΔH , r and α were obtained from DFT calculations of the energy profiles of the anionic oxygen (O₁) approach towards the electrophilic center (C₅) in each of the reactants **2-8**. The calculation results of the approaches are summarized in Table I.

TABLE III
CORRELATION EQUATIONS FOR DFT CALCULATED PROPERTIES FOR
RING-CLOSING REACTIONS OF Ω -BROMOALKANECARBOXYLATE
ANIONS **1-8** WITH THE CORRESPONDING EXPERIMENTAL VALUES

No	Equation	R value
1	$\Delta\Delta H_{\text{Exp}}^{\ddagger} = 0.16 E_{\text{s Exp}} + 15.13$	0.94 for n = 3-7
2	$\Delta\Delta H_{\text{Exp}}^{\ddagger} = 0.95 E_{\text{s Exp}} + 9.95$	0.95 for n = 8-14
3	$\Delta\Delta H_{(\text{TS}_1\text{-TS}_L)/\text{B3L/GP}} = -0.47 E_{\text{s Exp}} + 12.48$	0.92 for n = 4-11
4	$\Delta\Delta H_{(\text{TS}_1\text{-TS}_L)/\text{B3L/H}_2\text{O}} = -0.85 E_{\text{s Exp}} + 22.20$	0.92 for n = 4-11
5	$\Delta\Delta H_{(\text{TS}_1\text{-TS}_L)/\text{B3Lcc/H}_2\text{O}} = -0.92 E_{\text{s Exp}} + 23.76$	0.95 for n = 4-11
6	$\Delta\Delta H_{\text{P,SM}/\text{B3L/H}_2\text{O}} = -1.2836 E_{\text{s Exp}} + 31.898$	0.97 for n = 4-11
8	$S = 14.47 E_{\text{s Exp}} - 85.86$	0.97 for n = 5-9

Exp, B3L/GP, B3L/H₂O and B3Lcc/H₂O refer to experimental, calculated by B3LYP/6-31G (d, p) in the gas phase, calculated by B3LYP/6-31G (d, p) in water and calculated by B3LYP/aug-cc-pvdz in water, respectively. $\Delta\Delta H^{\ddagger}$ and $E_{\text{s Exp}}$ are enthalpic activation energy and experimental strain energy for ring-closing reactions of **1-8**, respectively. n is the number of atoms present in the cycle of the lactonization product. S is the slope of the plot of ΔH vs. $\sin \alpha + 1/r$, where α is the attack angle and r is the O₁-C₅ distance



Figs. 3. (a) Plot of experimental $\Delta\Delta H^{\ddagger}$ vs. experimental E_{s} for ring-closing reactions of **1-8**. (b) Plot of calculated $\Delta\Delta H (\text{TS}_1\text{-TS}_L)$ vs. experimental E_{s} for ring-closing reactions of **1-8**. For lines 1, 2 and 3 the $\Delta\Delta H (\text{TS}_1\text{-TS}_L)$ values were calculated by B3LYP/6-31 G (d, p) in the gas phase and B3LYP/6-31 G (d, p) and B3LYP/cc-pVDZ in water, respectively. (c) Plot of the slope (S) vs. experimental E_{s} for ring-closing reactions of **1-8**

The data of Table I was examined for linear correlations, and a strong correlation was achieved between the energy ΔH (enthalpic energy) and $\sin \alpha$ and $1/r$ ($R = 0.97 - 0.99$, see Table S1). Careful examination of Table S1 indicates that the energy needed to increase the value of angle α to reach the optimal value for the formation of a stable transition state is less for **2** than for **5**. This suggests that it is easier for O₁ to approach C₅ in system **2** than that in system **5**. Furthermore, it was found that the order of the slope values (S) for ΔH vs. $\sin \alpha + 1/r$ in systems **2-6** is: $S_5 > S_6 > S_4 > S_3 > S_2$, and when the S values were plotted against $E_{\text{s Exp}}$ values, very strong correlations were obtained (see eq. 8 in Table 3 and Figure 2c). Thus, S can be used as a good indicator for predicting the strain energy of a heteroatom ring.

The fact that intramolecular processes are much faster than their intermolecular counterparts has inspired organic chemists to explore enzyme catalysis by studying certain intramolecular reactions. Both enzymes and intramolecular processes are similar in that the reacting centers are held together covalently with intramolecular systems, and non-covalently with enzymes. Enzymes bring reacting molecules together precisely the correct position for reaction with each other and with catalytic functional groups at the enzyme active site. The resulting induced intramolecularity can account for the remarkable accelerations in rate observed with enzymes. Many theories were suggested to explain these phenomena. The most important among these theories are (1) proximity orientation (enthalpic factors), (2) strain effects, and (3) entropy factors.¹

In the series of bromoalkylcarboxylate anions **1-8** we have shown that the proximity orientation of the nucleophile (C(O) O⁻) to the electrophile (C-Br) is not playing a main role in the determining the cyclization rate of the intramolecular process. This is evident from the random correlation of the C---O distance (distance between the two reacting centers) with the intramolecular activation energy. On the other hand we have found that accelerations in rate are vastly affected by both the strain energy of the cycle being formed and the loss in entropy. The DFT calculation results reveal that ring-closing reactions to yield five- and six-membered rings enjoy low enthalpic energies due to the fact that in these reactions the products are strainless, whereas processes leading to eight- and nine-membered rings have high values of activation enthalpy. Further, the results indicate that processes leading to medium-sized rings (more than seven-membered) are accompanied by negative change in entropy that is mainly translational and rotational.

Examination of the calculated energy profiles for processes **1-8** reveals that the major loss of translational and rotational entropy occurs upon the conversion of the reactant (GM) to the first transition state (TS₁) due to major conformational changes of the reactant before engaging in a process by which bonds are being formed or broken. On the other hand, in the MTSZ (TS₁ to TS_L) the change in entropy is minimal and the change in energy is mainly enthalpic in origin. In processes leading

to strain-less rings such as five- and six-membered rings, the enthalpic difference between TS_1 and TS_L is relatively high due to the fact that the structure of TS_L is much more stabilized than that of TS_1 since the structure of the former resembles that of the strain less cyclic product. On the other hand, in ring-closing reactions leading to strained products such as eight- and nine-membered rings, the TS_1 - TS_L enthalpic difference is relatively low because the conformation and the stability of TS_L , resembles that of the strained cyclic product, are not much different from that of TS_1 .

IV. Conclusion

The salient points emerged from this study are: (1) S_N2 in intramolecular processes leading to the formation of small, medium and large sized rings have a wide range of multi-transition state zone where the highest transition state reflects activation energy (reaction rate) and the energy difference between the highest and the lowest transition states reflects internal strain energy (E_s) of the cycle being formed. The order of the transition states in the MTSZ (from the low TS to the high TS or *vice versa*) is dependent on the functional group of the system. (2) DFT calculations can be used as a good tool to predict cyclization rates, as well as, strain energies for different bi-functional entities that are difficult to be experimentally determined.

Acknowledgment

We thank the Karaman Co. and the German-Palestinian-Israeli fund agency for support of our hardware computational facilities. Special thanks to Rowan Karaman, Nardene Karaman and Donia Karaman for computational software support and technical assistance.

Supplementary Material

xyz Cartesian coordinates and absolute energies for GM, TS_1 and TS_2 for processes 1-8. Table S1: slope values (S) for the plots of ΔH vs. $\sin \alpha + 1/r$ in systems 2-6. Figure S1: Calculated global minimum (GM), first transition state (TS_1) and last transition state (TS_2) structures for ring-closing reactions of anions 1-8.

References

[1] For a review in this topic, see A. W. Czarink, In *Mechanistic Principles of Enzyme Activity*: (Eds.; J. F. Liebman, A. Greenberg) VCH publishers, New York, NY, 1988. T. C. Bruice, S. J. Benkovic, "Bioorganic Mechanisms" Vols. I and II; Benjamin: Reading, MA 1966. W. P. Jencks, "Catalysis in Chemistry and Enzymology"; McGraw; New York 1969. M. L. Bender, "Mechanism of Homogeneous Catalysis from Protons to Proteins"; Wiley Interscience: New York 1971. D. L. Nelson, M. M. Cox, "Lehninger Principles of Biochemistry" Worth Publishers: New York 2003. A. Fersht, "Structure and Mechanism in Protein Science: A guide to Enzyme Catalysis and Protein Folding, W. H. Freeman and Company, New York 1999. R.

Pascal, *Eur. J. Org. Chem.* (2003), 1813. R. Pascal, *Bioorganic Chemistry* **31** (2003), 485. G. F. Sweigers, "Mechanical Catalysis", John Wiley & Sons, (Hoboken, NJ), 2008. C. Walsh, "Enzymatic Reaction Mechanism" San Francisco: Freeman, 1979, pp 978. M. I. Page "In Enzyme Mechanisms. Ed. M. I. Page, A. Williams. London. R. Soc. Chem., 1987, pp 1. R. B. Silverman, "The Organic Chemistry of Enzyme-Catalyzed Reactions. San Diego: Academic, 2002, pp 717. R. Pascal, *Eur. J. Org. Chem.* (2003), 1813. D. A. Kraut, K. S. Carroll, D. Herschlag, *Annu. Rev. Biochem.* **72** (2003), 517. A. Radzicka, R. Wolfenden, *J. Am. Chem. Soc.* **118** (1996), 6105. M. J. Snider, R. Wolfenden, *J. Am. Chem. Soc.* **122** (2000), 11507. M. I. Page, W. P. Jencks, *Proc. Natl. Acad. Sci. U.S.A.* **68** (1971), 1678. M. I. Page, W. P. Jencks, *Gazz. Chim. Ital.* **117** (1987), 455. M. I. Page, *Chem. Soc. Rev.* **2** (1973), 295. M. I. Page, *Angew. Chem., Int. Ed. Engl.* **16** (1977), 449.

[2] F. M. Menger, M. Ladika, *J. Org. Chem.* **35** (1990), 3006. F. M. Menger, M. Ladika, *J. Am. Chem. Soc.* **110** (1988), 6794. F. M. Menger, *Acc. Chem. Res.* **18** (1985), 128. F. M. Menger, J. F. Chow, H. Kaiserman, P. C. Vasquez, *J. Am. Chem. Soc.* **105** (1983), 4996. F. M. Menger, *Tetrahedron* **39** (1983), 1013. F. M. Menger, J. Grossman, D. C. Liotta, *J. Org. Chem.* **48** (1983), 905. F. M. Menger, A. L. Galloway, D. G. Musaev, *Chem. Commun.* (2003), 2370. F. M. Menger, *Pure Appl. Chem.* **77** (2005), 1873 and references therein.

[3] T. C. Bruice, F. L. Lightstone, *Acc. Chem. Res.* **32** (1999), 127. F. L. Lightstone, T. C. Bruice, *J. Am. Chem. Soc.* **119** (1997), 9103. F. L. Lightstone, T. C. Bruice, *J. Am. Chem. Soc.* **118** (1996), 2595. F. L. Lightstone, T. C. Bruice, *J. Am. Chem. Soc.* **116** (1994), 10789. T. C. Bruice, W. C. Bradbury, *J. Am. Chem. Soc.* **90** (1968), 3803. T. C. Bruice, W. C. Bradbury, *J. Am. Chem. Soc.* **87** (1965), 4846. T. C. Bruice, U. K. Pandit, *J. Am. Chem. Soc.* **82** (1960) 5858. T. C. Bruice, U. K. Pandit, *Proc. Natl. Acad. Sci. U. S. A.* **46** (1960) 402.

[4] A. Dafforn, D. E. Jr. Koshland, *Proc. Natl. Acad. Sci. U. S. A.* **68** (1971), 2463; A. Dafforn, D. E. Jr. Koshland, *Bioorg. Chem.* **1** (1971), 129.

[5] S. Milstein, L. A. Cohen, *J. Am. Chem. Soc.* **92** (1970), 4377. S. Milstein, L. A. Cohen, *Proc. Natl. Acad. Sci. U. S. A.* **67** (1970), 1143. S. Milstein, L. A. Cohen, *J. Am. Chem. Soc.* **94** (1972), 9158.

[6] A. Greenberg, J. F. Liebman, "Strained Organic Molecules"; Academic Press; New York, 1978. J. F. Liebman, A. Greenberg, *Chem. Rev.* **78** (1976), 311.

[7] R. F. Brown, N. M. Van Gulick, *J. Org. Chem.* **21** (1956), 1046.

[8] R. Karaman, *Tet. Lett.* **49** (2008), 5998. R. Karaman, *Bioorg. Chem.* **37**(2009), 11. R. Karaman, *Tet. Lett.* **50** (2009), 452. R. Karaman, *Res. Lett. Org. Chem.* doi: 10.1155/2009/240253. R. Karaman, *Bioorg. Chem.* **37** (2009), 106. R. Karaman, *J. Mol. Struct. (Theochem)* **910** (2009), 27. R. Karaman, *Tet. Lett.* **50** (2009), 6083. R. Karaman, *J. Mol. Struct. (Theochem)* **939** (2010), 69. R. Karaman, *Tet. Lett.* **50** (2009) 7304. R. Karaman, *J. Mol. Struct. (Theochem)* **940** (2010), 70. R. Karaman, *Tet. Lett.* **51** (2010), 2130.

[9] L. Ruzicka, *Chem. Ind. (London)* **54** (1935), 2.

[10] For reviews on early studies see : G. Illuminati, L. Mandolini, *Acc. Chem. Res.* **14** (1981), 95. L. Mandolini, *Adv. Phys. Org. Chem.* **22** (1986), 1.

[11] C. Galli, G. Illuminati, L. Mandolini, *J. Am. Chem. Soc.* **95** (1973), 8374; C. Galli, G. Illuminati, L. Mandolini, P. Tamborra, *J. Am. Chem. Soc.* **99** (1977), 2591; L. Mandolini, *J. Am. Chem. Soc.* **100** (1978), 550.

[12] M. A. Casadei, C. Galli, L. Mandolini, *J. Am. Chem. Soc.* **106** (1984), 1051.

[13] G. Illuminati, L. Mandolini, B. Masci, *J. Am. Chem. Soc.* **97** (1975), 960. G. Illuminati, L. Mandolini, B. Masci, *J. Am. Chem. Soc.* **99** (1977), 6308. L. Mandolini, B. Masci, S. Roelens, *J. Org. Chem.* **42** (1977), 3733. A. Dalla Cort, L. Mandolini, B. Masci, *J. Org. Chem.* **45** (1980), 3923. A. Dalla Cort, G. Illuminati, L. Mandolini, B. Masci, *J. Chem. Soc. Perkin Trans. 2* (1980), 1774.

[14] C. Galli, P. Gargano, L. Mandolini, *Gazz. Chim. Ital.* **116** (1986), 653.

[15] C. Galli, G. Illuminati, L. Mandolini, *J. Org. Chem.* **45** (1980), 311.

- [16] C. Galli, L. Mandolini, *Eur. J. Org. Chem.* (2000), 3117.
 [17] <http://www.gaussian.com>.
 [18] U. Burkner, N. L. Allinger, *Molecular Mechanics*; American Chemical Society; Washington, DC, 1982.
 [19] C. J. Casewit, K. S. Colwell, A. K. Rappe', *J. Am. Chem. Soc.* **114** (1992), 10024. C. J. Casewit, K. S. Colwell, A. K. Rappe', *J. Am. Chem. Soc.* **114** (1992), 10035. C. J. Casewit, K. S. Colwell, A. K. Rappe', *J. Am. Chem. Soc.* **114** (1992), 10046.
 [20] M. J. S. Dewar, E. G. Zoebisch, E. F. Healy, J. J. P. Stewart, *J. Am. Chem. Soc.* **107** (1985), 3902.
 [21] J. N. Murrell, K. J. Laidler, *Trans Faraday Soc.* **64** (1968), 371.
 [22] K. Fukui, *Acc. Chem. Res.* **14** (1981), 363. K. Muller, *Angew. Chem. Int. Ed. Engl.* **19** (1980), 1.
 [23] M. T. Cancès, B. Mennucci, J. Tomasi, *J. Chem. Phys.* **107** (1997), 3032. B. Mennucci, J. Tomasi, *J. Chem. Phys.* **106** (1997), 5151; B. Mennucci, E. Cancès, J. Tomasi, *J. Phys. Chem. B* **101** (1997), 10506; J. Tomasi, B. Mennucci, E. Cancès, *J. Mol. Struct. (Theochem)* **464** (1999), 211.
 [24] F. Jensen, "Introduction to Computational Chemistry" John Wiley & Sons 2002, pp 1-422.
 [25] J. Hine, *Adv. Phys. Org. Chem.* **15** (1977), 1.
 [26] A. P. Bento, F. M. Bickelhaupt, *J. Org. Chem.* **72** (2007), 2201. A. P. Bento, F. M. Bickelhaupt, *J. Org. Chem.* **73** (2008), 7290. G. Th. de Jong, F. M. Bickelhaupt, *ChemPhysChem* **8** (2007), 1170.
 [27] D. H. Ess, K. N. Houk, *J. Am. Chem. Soc.* **130** (2008), 10187; D. H. Ess, K. N. Houk, *J. Am. Chem. Soc.* **129** (2008), 10646; L. Xu, C. E. Doubleday, K. N. Houk, *Angew. Chem. Int. Ed.* **48** (2009), 2746.
 [28] Some of the $E_{3 \text{ Exp}}$ values were calculated by different methods, for further information see: K. H. Wiberg, R. F. Waldron, *J. Am. Chem. Soc.* **113** (1991), 7697; J. M. Brown, A. D. Conn, G. Pilcher, M. L. P. Leitao and Y. Meng-Yan *Chem. Commun.* (1989), 1817. H. J. Rodriguez, J.-C. Chang, T. F. Thomas, *J. Am. Chem. Soc.* **98** (1976), 2027. H. J. Rodriguez, I. H. Williams, *J. Chem Soc. Perkin Trans. 2* (1997), 953.

Authors' information

Faculty of Pharmacy,
 Al-Quds University, P. O. Box 20002, Jerusalem,
 E-mail: dr_karaman@yahoo.com. Fax + (972) 2790413

Multivariate and T_1 Analysis on Serum Samples from Coronary Heart Disease Patients (CHD): a Pilot Study

Divya Misra, Usha Bajpai

Abstract – The one dimensional 1H NMR at $48^\circ C$ of serum samples were acquired for CHD (coronary heart disease patients) ($n = 26$). The reduced ultra binned spectra region 0.77-0.81ppm of 0.01ppm at $48^\circ C$ comprising of methyl protons of VLDL, LDL and HDL were found to provide discriminating clusters in the Principal Component Analysis score plots when compared with healthy control serum samples. The spin lattice relaxation times (T_1) of alanine, lactate and methylene protons of lipoproteins were found to be significantly reduced in univariate analysis when compared with control samples. The T_1 values of these metabolites were further subjected to Discriminant Function Analysis (DFA) for control and CHD patients. It was observed that 84.6% of correct classification was achieved. The analysis demonstrated that NMR can be an effective method for diagnosis of CHD in clinical setup. **Copyright © 2010 Praise Worthy Prize S.r.l. - All rights reserved.**

Keywords: Serum, Metabolites, Lipoproteins, Spin Lattice Relaxation Time

I. Introduction

Coronary heart disease (CHD) is the major cause of mortality and morbidity in developed and developing countries, affecting as many as one in three individuals before the age of 70 years[1]. The CHD rates among overseas Asian Indians worldwide are 50% to 400% higher than people of other ethnic origin irrespective of gender, religion, or social class. India is now in the middle of a CHD epidemic with urban Indians having CHD rates similar to overseas Indians, which is 4-fold higher than Americans[2]. Whereas, the CHD rates has reduced considerably in the West during the past 30 years, while the rates doubled in India with no signs of a downturn yet[3]. The average age of first myocardial infarction (MI) has decreased by 20 years in India. Among Asian Indian men, about half of all MI occur under the age of 50 and 25% under the age of 40[4]. Studies have come out with facts that , coronary heart disease (CHD) is the leading cause of death in India, not only this the deaths due to it are expected to double in the next ten years[5]. Regular physical activity has been found helpful in reducing the risk of obesity[6] blood lipid abnormalities[7], hypertension, and non-insulin dependent diabetes mellitus, but has also been shown to reduce substantially the risk of coronary heart disease (CHD) [8].

Over the past three decades many risk factors involved in development of CHD have been identified. CHD is caused by atherosclerosis, a process characterized by endothelial dysfunction- in association with hypertension either systolic/diastolic or isolated systolic[9], diabetes[10], smoking[11], and elevated homocysteine concentrations.

(LDLMW) (Low density lipoprotein molecular weight) has been shown to correlate positively with coronary heart disease. It has been shown in that LDL MW decreases as plasma triglyceride increased and concentrations of triglyceride were found to be greater in CHD patients, than in controls [12]. The risk factors identified so far from the cross-sectional epidemiological studies are insufficiently powerful to provide a clinically useful diagnosis of CHD[13]. Although several algorithms have been designed based on a range of risk factors such as age, sex, physical activity, systolic/diastolic blood pressure, body mass index (BMI)[14], which can identify subpopulations at very significant excess risk of CHD. Even the best of these have failed to diagnose the presence of CHD on an individual-by-individual basis.

NMR based analysis and metabolomics in biofluids offers many advantages to traditional clinical chemistry, like it can be carried out on standard preparations of serum, plasma or urine, circumventing the need for specialist preparations of cellular RNA and proteins required for genomics and proteomics analysis. Many risk factors have already been identified, such as levels of various lipids and small molecule metabolites that will contribute to the metabonomic data set[15].

James D. Otvas who began his research on nuclear magnetic resonance of blood plasma in 1988 successfully discovered that NMR could measure lipoprotein levels in blood plasma and that NMR could measure the lipoprotein particle size and particle number[16] The usefulness of NMR LipoProfile test in the assessment of CHD risk gained importance in 1999. Also landmark data from Framingham offspring study demonstrates

clinical benefit of lowering LDL-P number, in 2008 American Diabetes Association and the American College of Cardiology Foundation publishes consensus statement recognizing the role of lipoproteins in atherosclerosis[17].

Many studies in literature show the role of lipoproteins in CHD. Like Freedman study shows that large VLDL and small HDL particles play important role in development of CHD (1998). While in 2002 Kuller L et. al study concluded that the size of LDL particles and the greater number of LDL particles are related to incidents of CHD among older woman. The basis for NMR analysis and lipoprotein subclasses is that each lipoprotein particle in plasma within a given diameter range broadcasts a distinctive lipid NMR impression, the intensity of which is proportional to its bulk lipid mass concentration.

Though deconvolution at 48°C is quantitative but is not for normal utilization because it is patented. The Liposcience Incorporation USA, routinely analysis serum samples by ¹H NMR spectra at 48°C and quantify different lipoproteins using this patented deconvolution method. Since, standard available post processing mathematical filters such as Gaussian enhancements are available in NMR spectrometers and provide resolution enhancement to a certain extent, extra fine binning of the methyl resonances of the lipoproteins may provide differentiation in PCA CHD analysis when compared with control.

Small molecular weight components like lactate, alanine etc. usually posses non-covalent interaction properties with lipoprotein in the complex mixture of serum samples. Due to this, there relaxation times may get altered as different sizes of lipoprotein are present in the serum. Since there is an increase in the concentration of VLDL in CHD patients, it was therefore envisaged that spin lattice relaxation time (T_1) of the small molecules in serum may be used as an indicator for differentiating healthy controls with CHD patients

With this aim and objective, a pilot study has been carried out in order to evaluate T_1 of most significant metabolites to have a simple discriminating aspect for distinguishing between healthy subjects and CHD subjects at normal temperature followed by high temperature at 48°C. This ultra fine binning along PCA and T_1 studies, may come out with results which can be sufficient in order to discriminate between CHD patient and normal control. The differences obtained in the results of CHD and control can be utilized in clinical set up provided an NMR spectrometer is available.

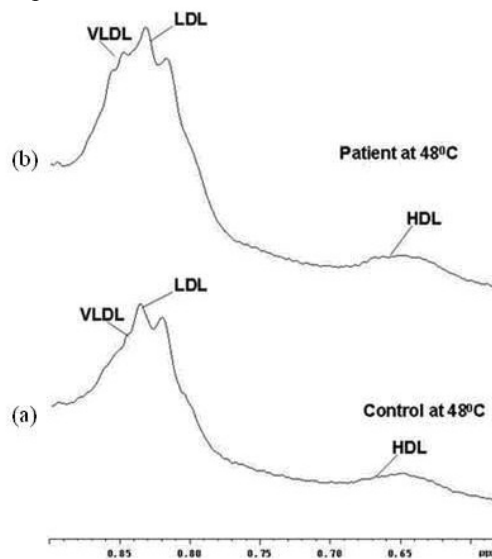
II. Material and Methods

The study was carried out on (n = 26) patients of ischemic heart disease admitted to KGMC with acute myocardial infarction presenting within 48 hours of symptoms. Stable angina, Unstable angina and (n= 26) age/sex matched healthy normal without any manifestations of atherosclerosis individuals.

After 12 hours of fasting 2ml of blood sample from each patient was taken and was allowed to clot in plastic tube for 2 hrs at room temperature 37°C. The serum was collected by centrifugation. Half of the sample was sent for carrying lipid analysis by conventional method and the other half was stored in liquid nitrogen for NMR studies. The samples were stored under liquid nitrogen. Before NMR analysis, 600µl of the samples were taken in a 5mm high quality NMR tubes. Inside the NMR tube a capillary containing D₂O with 70mg/dL of external reference TSP was inserted inside the 5mm NMR tube prior to NMR measurement.

The NMR measurements were carried out on a Bruker Avance 400 FT NMR spectrometer (Switzerland) operating at 400 MHz frequency, equipped with 5mm multinuclear inverse period with Z shielded gradient. Recording of the one dimensional NMR spectra were performed with water suppression using NOESY pulse sequence at 25°C and 48°C. The FID's obtained at 48°C were multiplied by Gaussian window function for resolution enhancement using Gaussian broadening of 0.15Hz and a line broadening of -1.5 Hz prior to fourier transformation.

A 1D NMR spectrum of the representative classes is shown in Figure 1 at 48°C, along with expansion of the methyl protons of VLDL, LDL and HDL in Figure 2 which distinctively showed differences in the pattern of the disease state with respect to control cases. Chemical components were assigned on the basis of previous published data[18-19] as well as based on assignments on 2D spectra.



Figs. 1. 1D NMR Spectrum of the representative classes

III. Statistical Analysis

26 cases of normal healthy control and 26 cases of coronary heart disease patients were taken and then the spin lattice relaxation time T_1 (in milliseconds) of nine major metabolites lipids, creatine/creatinine, glutamine, N-Acetyl aspartate, alanine, CH₂LP, valine, CH₃LP were

evaluated with the help of Bruker Topspin software Version 3 .

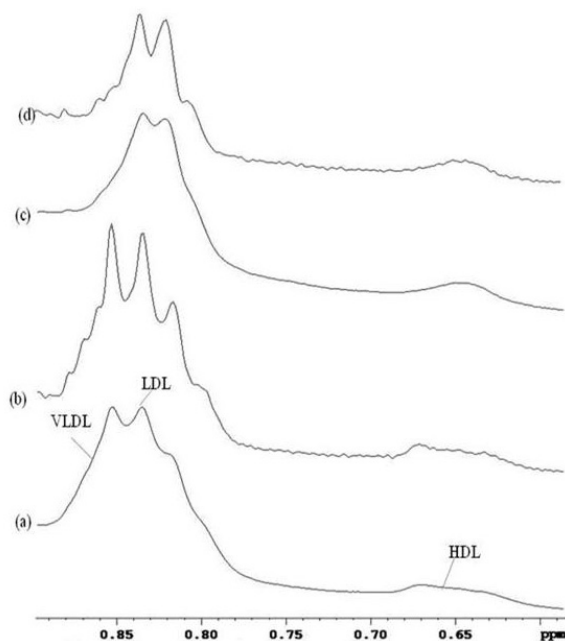


Fig. 2. Typical expansion of the Resolution Enhanced ^1H Spectra of Serum Sample at 48°C (a) & (c) for Control and (b) & (d) for CHD patient

The data was analysed by two statistical methods viz PCA and DFA. Also, the mean pictorial representation of the spectra along with the covariance matrix was calculated in software, AMIX version 3.7.10 of Bruker Biospin Switzerland. PCA was performed with the help of software while DFA was done using SPSS version 11.5.

IV. Results

The spectra of serum sample of control and CHD patient Figure 1 with expansion at 48°C of the specified region of HDL, LDL and VLDL are as shown in Figure 2. It is successful in demonstrating that in CHD cases concentration of LDL (Low Density Lipoprotein) is higher compared to control. This discrimination was due to the variation of ^1H -NMR profile of the controls which differed from the CHD cases. The most influential region for the CHD samples lies around 0.7 to 0.88 ppm mainly due to the CH_3 group from fatty acid side chain in lipids in particular LDL, VLDL, HDL. Since other regions for eg 1.26 ppm, 1.3 ppm, 1.34 ppm, 3.22 ppm are mainly due to the $(\text{CH}_2)_n$ groups of fatty acid of VLDL, LDL, HDL and due to choline (principally phosphatidyl choline) from lipoproteins were observed in NMR spectra but this region was not analysed due to overlapping of other metabolites present in NMR spectrum. The region 0.70 ppm to 0.88 ppm was further subjected to deconvolution in order to obtain various subclasses of lipoproteins. Figure 2 clearly indicates marked increase in small LDL particles in CHD samples compared with

normal healthy control.

With the help of student t-test it was found that out of the nine metabolites studied three (Lactate, Alanine and CH_2LP) were found significant. The statistical significance for the quantified metabolites was determined by univariate t-test. A probability p-value of less than 0.05 was taken to indicate statistical significance. The discriminant function for the metabolites found significant viz. lactate, alanine and methylene protons is given by:

$$d(z) = -3.836 + 0.006\text{Ala.} + 0.005\text{Lac.} - 0.005*\text{CH}_2\text{LP}$$

with a cut off value of 0.081.

Lactate was found to be highly significant in this test, while alanine and CH_2LP was found significant. Hence out of the nine variables studied (lipids, creatine/creatinine, glutamine, N-acetyl aspartate, alanine, lactate, CH_2LP , valine, CH_3LP) best discrimination between control and disease groups is obtained by these three variables (Alanine, Lactate, CH_2LP) with an overall classification of 72.1%. Addition of other study variable's does not improve the classification level.

A detailed statistical summary of 26 control and 26 patient cases is given in Table I. Variations were observed in the measurement range of T_1 as the S.D. variables and mean values showed variation's as is clear from the table, hence need was felt for further detailed statistical analysis

Further the K – mean cluster test was applied to the three metabolites found significant in student t – test vs lactate, alanine and CH_2LP with the help of which we found for the two groups, control and disease, the cluster centres obtained for the significant metabolites for control group for alanine, lactate and CH_2LP were 453.11, 764.86 and 360.09, and for the disease group were 389.35, 498.15 and 398.60 respectively.

Following the univariate analysis the data were further subjected to multivariate analysis to see their impact on disease classification. First we considered all the variables together to select the best discriminatory variables for control and disease cases. Now considering the significant variables alanine, lactate and CH_2LP . The discriminant scores were calculated by the following formula:

$$dF(z) = -6.147 + 0.009\text{Ala} + 0.005 \text{Lac.} - 0.003\text{CH}_2\text{LP}$$

with a cut off value of zero. It classifies 84.6% correctly, which is a very good percentage in clinical studies.

Alanine and Lactate were found to be most important. The discriminant scores for which were calculated by the following formula:

$$\text{Discriminatory function (z)} = -7.366 + 0.009 * \text{Ala.} + 0.005 * \text{Lac}$$

with a cut off value of zero .

TABLE I
SUMMARY OF T₁ (IN MILLISECONDS) ALONG WITH STATISTICAL
ANALYSIS OF 26 CONTROL AND 26 DISEASE CASES

Variable	Control (n=26) Mean ± S.D.	Disease (n=26) Mean ± S.D.	t - value	Sig. Level
Lipids	466.28 ± 62.99	490.43 ± 83.73	1.17	0.245 (NS)
creatinine/creatinine	269.26 ± 62.98	285.45 ± 118.52	.615	0.541 (NS)
glutamine	282.26 ± 35.41	290.62 ± 38.18	.819	0.417 (NS)
N-Acetyl Aspartate	448.80 ± 35.03	435.48 ± 44.91	1.193	0.24 (NS)
alanine	487.46 ± 70.84	398.25 ± 79.78	4.264	0.001 (S)
lactate	772.70 ± 117.17	595.57 ± 164.49	4.472	0.001 (S)
CH ₂ LP	356.30 ± 25.97	391.96 ± 87.68	1.988	0.052 (S)
valine	282.29 ± 57.96	286.38 ± 53.29	0.264	0.793 (NS)
CH ₃ LP	350.18 ± 31.98	370.68 ± 52.8	1.706	0.094 (NS)

From this test it is concluded that if composite square (z) is +ve then control group, if score is -ve then it is patient. Alanine and Lactate classifies 82.7% cases correctly.

For the PCA score plot the spectral data were data reduced to 17 bucket segments, each comprising 0.01ppm which comprises only for the methyl resonances (0.79 – 0.89ppm) lipoprotein region and serum glucose region before chemometric analysis using AMIX (Analysis of MIXtures software package, version 2.5, Bruker). The PCA plot Figure 3 was successful in demonstrating discriminant clustering between the control and disease states.

V. Discussion

Out of the nine variables studied (lipids, creatine/creatinine, glutamine, N-acetyl aspartate, alanine, lactate, CH₂LP, valine, CH₃LP) best discrimination between control and disease groups is obtained by three variables viz (Alanine, Lactate, CH₂LP). Linear discrimination function helped in giving a correct classification of 82.7% for alanine and lactate which is a very good result as far as clinical studies are concerned. From student t-test we conclude that the spin relaxation time of alanine and lactate are significantly lower in disease group compared to that of control group and methylene protons of lipoproteins is significantly higher in disease group compared to control.

From the study we can conclude that lactate and alanine were highly significant, while CH₂LP was significant. In the rest of the six variables (lipids, creatine/creatinine, glutamine, N-acetyl aspartate, valine, CH₃LP) there is no significant difference between control and disease, they are similar.

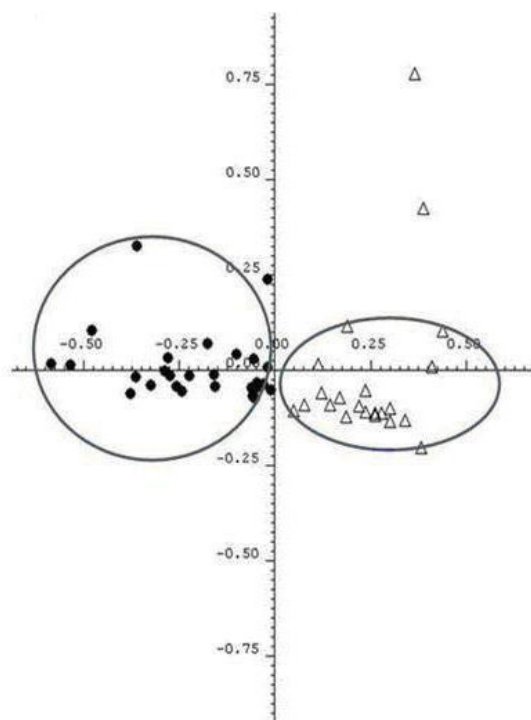


Fig. 3. PCA plots showing clustering of patients and normal healthy control

As can be observed from the summary statistics (Table I) the Mean ± SD of T₁ time is higher in case of control (772.70 ± 117.17) and less (595.57 ± 164.49) in case of disease, the reason for this being that lactate binds easily with lipoproteins (LP), because of which the size of LDL (Low Density Lipoproteins) becomes bigger resulting in shortening of spin lattice relaxation time. LDL (low molecular weight) is higher in patients with CHD, since it is the size that affects T₁, also average T₁ of CHD is coming lower compared to cases of control. Similar is the case with alanine a non-polar amino acid, the T₁ values of CHD patients is (398.25 ± 79.78) were significantly shorter (P < 0.01) than those of controls (487.46 ± 70.84). While the CH₂LP group also shows a lower level of significance compared to lactate and alanine with the control group showing a T₁ time of (356.30 ± 25.97) which is lower compared with the disease group, which shows a T₁ time of (391.96 ± 87.86).

Principal Component Analysis score plot (Figure 3) was successful in demonstrating clustering of the disease group (CHD) with the control group. Resolution enhanced spectra was obtained because of high temperature studies because of which differentiation between control and disease is possible. These two new methods help us in getting a better profile in control and disease cases.

VI. Conclusion

Hence we have successfully shown an alternate method where we do not do deconvolution (which is

patented), but by performing a simple experiment on T_1 we are able to discriminate between control and CHD patients. Under Indian conditions overnight fractional ultracentrifuge takes 12 hours, but in our case only half an hour is required. Using CPMG, we can evaluate T_1 better, we have shown that subtypes Lipoprotein concentration quantitation by NMR is possible. Whereas in the deconvolution method there are equations which makes the procedure complicated, but our approach was a simpler one. To the best of our knowledge such a study has been reported for the first time.

The study may open new possibilities for diagnosis of coronary heart disease in a simple way in response to relaxation effects. However, more extensive study is required on a large sample size and to incorporate other clinical conditions like diabetes, smoking, alcohol in take in patients suffering from CHD.

Acknowledgement

The authors are highly indebted to Dr. Rupali Khanna of Department of Medicine, Chhatrapati Shahuji Maharaj Medical University, Lucknow, India and Dr. A. Ghatak, Division of Experimental Medicine, Central Drug Research Institute, Lucknow, India, and Dr. Raja Roy, Division of SAIF, CDRI Lucknow, for allowing us to perform additional experiments eg T_1 and ^1H NMR measurements at 48°C of CHD patients for evaluating the physical parameters for this additional study in contribution to our earlier work.

References

- [1] J.T. Brindle, H. Antti, E. Holmes, et al., Rapid and noninvasive diagnosis of the presence and severity of coronary heart disease. *Nat. Med.*, 2002, 8, pp. 1439-1444.
- [2] V. Singh, and P. Deedwania, Dyslipidemia in Special Populations: Asian Indians, African Americans, and Hispanics. *Curr. Athero. Rep.*, 2006, 8, pp. 32-40.
- [3] K. Goswami, and A. Bandyopadhyay, Lipid profile in middle class Bengali population of Kolkata. *Ind. Jour. of Clin. Bioch.*, 2003, 18, pp. 127-130.
- [4] E.A. Enas, A. Senthilkumar, Coronary artery disease in Asian, Indians: An update and review. *The Internet Jour. of Cardio.*, 2001, 1, pp. 1-57.
- [5] T. Rastogi, M. Vaz, D. Spiegelman, et al., Physical Activity and risk of coronary heart disease in India. *Inter. Jour. of Epidem.*, 2004, 33, pp. 759-767.
- [6] T. Leskinen, S. Sipilä, et al., Leisure-time physical activity and high-risk fat: a longitudinal population-based twin study. *Inter. Jour. of Obesity*, 2009, 170, pp. 1038.
- [7] S. Daniels, Exercise and Lipid Abnormalities. *Pedia. Cardio.* 1999, 20, pp. 71-77.
- [8] T. Rastogi, K. S. Reddy, et al., Diet and risk of ischemic heart disease in India. *Ameri. Jour. of Clin. Nutr.* 2004, 79, pp. 582-592.
- [9] M. Moser, Hypertension treatment and the prevention of coronary heart disease in the elderly. *Amer. Fam. Physic.* 1999, 59, pp. 1248.
- [10] R. Roussel, F. Mentré, et al., NMR-based prediction of cardiovascular risk in diabetes. *Nat. Med.* 2007, 13, pp. 399-400.
- [11] M. Yokode, T. Kita, et al., Cholesteryl ester accumulation in macrophages incubated with low density lipoprotein pretreated with cigarette smoke extract. *Proc. Natl. Acad. Sci. U.S.A.* 1988, 85, pp. 2344-2348.

- [12] M. Schlaich, S. John, et al., Elevated homocysteine concentrations impair endothelium dependent vasodilation in hypercholesterolemic patients. *Atheros.* 2000, 153, pp. 383-389.
- [13] A.C. Nicholson, K.B. Pomerantz, et al., Inhibition of cholesterol esterification in macrophages and vascular smooth muscle foam cells: evaluation of E5324, an acyl-CoA cholesterol acyltransferase inhibitor. *Lipids*, 1995, 30, pp. 771-774.
- [14] K.E. Reed, W. Darren et al., Cardiovascular Disease Risk In Elementary School Children: Developing a Healthy Heart Score. *Jour. of Spor. Scien. and Med.* 2007, 6, pp. 142 - 148.
- [15] Y. Wang, E. Holmes, et al., Metabonomic investigations in mice infected with *Schistosoma mansoni*: An approach for biomarker identification. *Proc Natl Acad Sci U.S.A.* 2004, 34, pp. 12676-12681.
- [16] J. Otvás, E. Jeyarajah, et al., A spectroscopic approach to lipoprotein subclass analysis. *J Clin Ligand Assay* 1996, 19, pp. 184-189.
- [17] J.D. Brunzell et al., Lipoprotein Management in Patients with Cardiometabolic Risk. *JACC*, 2008, 51, pp. 1513.
- [18] J. D. Bell, and P. J. Sadler, Body fluids. *Encyclo. of Magnet. Reson.* John Wiley and Sons: New York. 1999, 2, pp. 989-1001.
- [19] V. Govindaraju, K. Young, et al., Proton NMR chemical shifts and coupling constants for brain metabolites. *NMR Biomed.* 2000, 13, pp. 129-153.

Author's information



Dr. Divya Misra born in Kanpur, India has done her Ph.D. in the field of Nuclear Magnetic Resonance Spectroscopy, in the year 2009. She has various national and international papers to her credit. Her main field of interest includes metabolite identification by NMR spectroscopy. She is a member of NMRS society. Presently she is serving as Senior Lecturer at Babu Banarasi Das Institute of Engineering and

Technology, Lucknow.

Physico-Chemical Changes of Human Serum Albumin During in Vivo and in Vitro Glycation Processes

N. Sattarahmady^{1*}, A. A. Moosavi-Movahedi², M. Habibi-Rezaei³, H. Heli⁴

Abstract – Glycation, a post-translational modifications, includes the arrangement of proteins with chemically reversible early glycation products, Schiff bases and Amadori adducts. These early products endure slow and complex rearrangements to create advanced glycation end-products (AGEs) that involved in diabetic complications. Here, physico-chemical characteristics of in vitro glycated human serum albumin (HSA) during 14 and 28 days incubation at the presence of glucose inquire with that happened in human serum. The formation of Amadori products, AGE-specific fluorescence intensity, extent of lysine residue modification and the changes in the content of α -helices, and also surface tension value in HSA are all in similar manners in both conditions. It was observed, however, that arginine residues were modified only under physiological conditions (in vivo), and did not occur in vitro. This difference was related to the presence of 3-deoxyglucosone, a 1,2-dicarbonyl compound derived from glucose under physiological conditions. Therefore, the biophysical studies on the HSA glycation process in vitro are credible. Copyright © 2010 Praise Worthy Prize S.r.l. - All rights reserved.

Keywords: Human Serum Albumin, Glycation, Diabetic Individual, Arginine Residue

I. Introduction

Glycation endproducts have been implicated in the pathogenesis of diabetic and uremic complications. Nonenzymatic protein glycation is a classic covalent reaction between reducing sugars and basic amino groups of proteins. Accordingly, it finally yields a class of heterogeneous chemical compounds collectively referred to advanced glycation end products (AGE). Yield of these reactions depends on the glucose concentration and the resultant AGE can permanently alter protein structure and function [1]-[4]. The glycated proteins accumulate in diabetic patients more than normal subjects because of the presence of high glucose concentration during diabetes [5]. In principle, the functions of glycated proteins differ from their non-glycated form. This fact has been suggested for human serum albumin (HSA), hemoglobin, and a series of intracellular enzyme proteins [6].

HSA is the most abundant in human blood serum (40 mg/ml) and quantitatively is the most important depot and transport protein in blood plasma. It is responsible for the binding and transport of endogenous compounds and drugs.

Also, it is a major antioxidant with important roles in maintaining normal osmolarity of plasma and interstitial fluids. It is synthesized in the liver as a single, non-glycosylated polypeptide, which is organized to form a heart-shaped protein comprising about 67% α -helix with no β -sheet [7]-[9].

HSA glycation is of special interest because HSA bears approximately 58 lysine residues making it a favorable target for the glycation process [10]. The identification of the sites of glycation, structural and functional changes during glycation of HSA, and AGE formation in the presence of different carbohydrates have been the subject of recent in vitro studies [11]-[18]. The level of glycated albumin might also be of value as an indicator of the degree of hyperglycemia in diabetics [12].

We reported studies about glycation of HSA in vitro and its characteristics and structural changes during glycation process [19]-[21]. In this study, aim is approval of the structural characteristics of in vitro glycated human serum albumin with that happened in human serum.

II. Materials and Methods

II.1. Materials

HSA, β -D (+) glucose, p-nitroblue tetrazoliumchloride (NBT), Cibacron Blue-3GA Agarose and millipore ultrafiltration membrane (30KDa) were from Sigma. The membrane filter with 0.2 μ m pore size (25 mm in diameter) and dialysis tubing of 10,000 MW cut off were from Whatmann (UK). Sodium azide, EDTA, 9, 10 phenanthrenequinone were from Merck (Germany). 2,4,6-trinitrobenzene sulfonic acid (TNBSA) was from Fluka. All other materials were of analytical grade. All solutions were prepared with deionized water.

II.2 Methods

HSA samples were obtained from pool serum of healthy and diabetic volunteers with different range of glucose concentration (Table I). Serum samples were filtered with a Millipore ultrafiltration membrane (cutoff: 30 kDa, using an Amicon Ultrafiltration apparatus) followed by affinity column chromatography (1*20 cm) on Agarose-Immobilized Cibacron Blue 3GA [22], [23]. The absorbance of eluent solution at 280 nm was recorded with a Shimadzu spectrophotometer model UV-3100. For the investigation of protein separation and purity, SDS-PAGE was carried out according to the method of Laemmli [24]. Protein bands were detected by Coomassie staining method [25]. Concentrations of the protein samples were determined in triplicate by bicinchoninic acid protein assay (BCA assay).

In vitro glycated HSA samples (40 mg/mL) were obtained by incubation of HSA with different concentrations of glucose (90-400 mg/dL) in sodium phosphate buffer (50 mM Na₂HPO₄/NaH₂PO₄ pH 7.4, 1 mM EDTA, and 0.1 mM sodium azide) in capped vials under sterile conditions at 37°C in the dark for 14 and 28 days. Glucose concentrations were selected similar to the concentrations of normal and diabetic individuals. The samples were used for further studies after dialyzed against sodium phosphate buffer at 4°C for 48 h.

Physico-chemical changes of serum albumin during glycation process in purified proteins and incubated protein were analysed with determination of modification extent of side chain residues (Lysine [12] and Arginine [26]) and Amadori product extent [26], measurements of AGEs fluorescence [19], [26], surface tension measurements [21] and Far-UV CD measurements [19].

III. Results

Many studies have discussed the structural changes and characteristics of proteins during glycation process in vitro [11]-[21]. But the compatibility and confirmation of these properties with those occurred in vivo has not been approached. In order to determine whether the results of structural changes and characteristics of glycated albumin in vitro and in serum of diabetic patients are compatible, purification of albumin from pool serum of normal and diabetic patients with different glucose blood concentrations was performed. The concentrations of glucose in the human serum samples are listed in Table I.

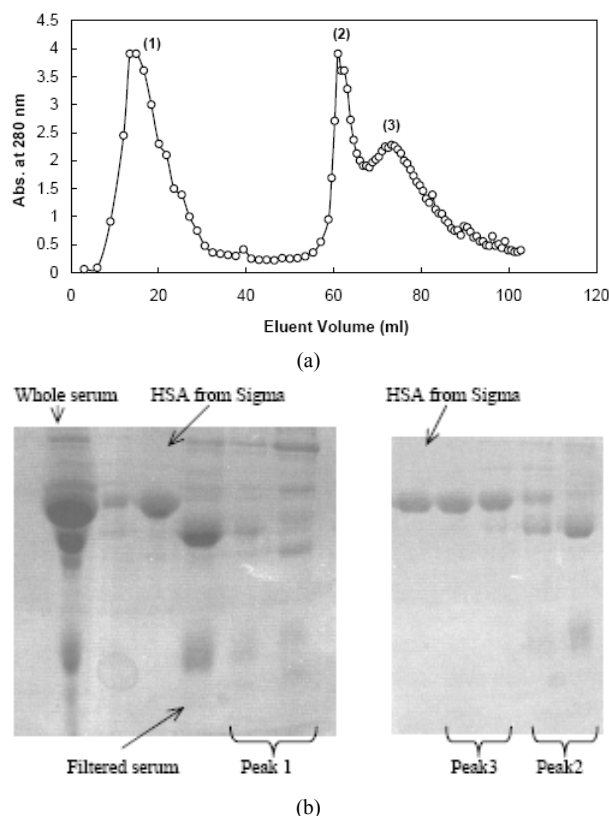
Albumin was purified by a Cibacron Blue-3GA Agarose column and the absorbance of eluent solution at 280 nm is shown in Fig. 1(a). Previous studies showed that this approach is very effective to remove albumin from human plasma [22], [23].

After purification, SDS-PAGE and Coomassie staining methods were used to confirm the purification method (Fig. 1(b)).

TABLE I
THE CONCENTRATION RANGE OF SUGAR IN HUMAN SERUM SAMPLES OF NORMAL AND DIABETIC INDIVIDUALS

Sample	Serum sugar concentration (mg/dl)	Condition
1	< 100	Normal individual
2	150-200	Diabetic individual
3	200-250	Diabetic individual
4	300-350	Diabetic individual
5	> 400	Diabetic individual

Based on the results, HSA was truly purified from other proteins present in the samples. Also, HSA was incubated with different concentrations of glucose (similar to in vivo condition) for 14 and 28 days to study the progression of glycation reaction in vitro. Then, experiments were designed as follows to discriminate the albumin glycation process in vitro and in vivo.



Figs. 1. a) A typical affinity chromatogram for filtered pool diabetic serum on a Cibacron Blue-3GA Agarose column (1*20 cm). The protein fractions were measured at 280 nm. b) The results obtained from the SDS PAGE of the samples of eluted solution of filtered pool diabetic serum from the location 1, 2, 3 from chromatogram and control HSA from Sigma

To evaluate the changes in the secondary structure, the circular dichroism spectra (Far-UV CD) in the range of 190–260 nm were acquired for the albumin samples. Molar ellipticity at 222 nm shows changes in helical structure of proteins. These changes for albumin samples were represented in Fig. 2.

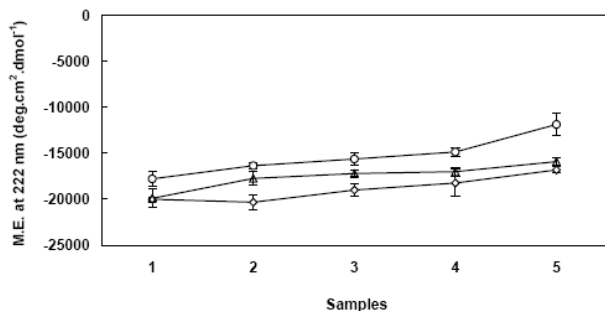
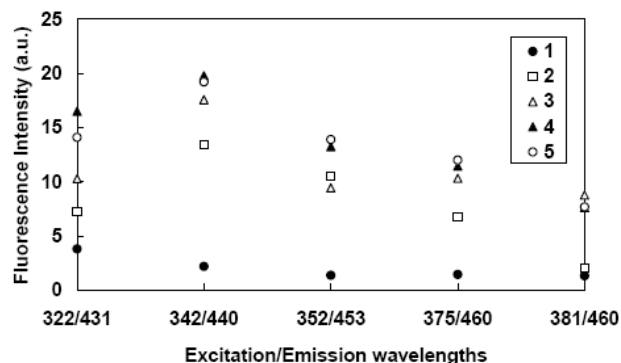


Fig. 2. Molar ellipticity at 222 nm for HSA samples which were purified from human serum (●) and in vitro glycated samples (△, ◇) after 14 days incubation (△) and after 28 days incubation (◇) in phosphate buffer, pH 7.4, with (1) < 100, (2) 150-200, (3) 200-250, (4) 300-350 and (5) > 400 mg/dl sugar concentration

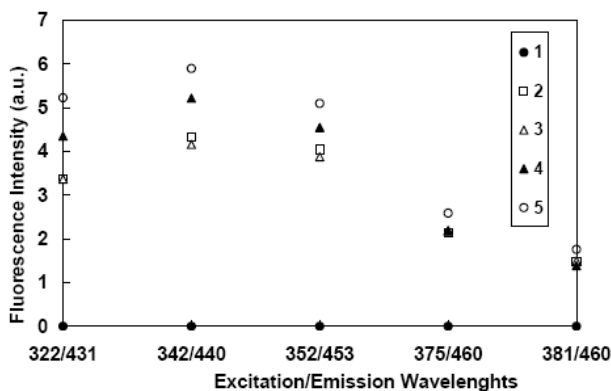
In this figure, upon increasing sugar concentration in serum of diabetic patients and in vitro samples (with respect to the HSA of normal glucose individuals), there is a decrease in the negative ellipticity at 222 nm. The result indicates a loss of helical structure. Therefore, increasing the sugar concentration or the degree of hyperglycemia leads to a decrease in the content of α -helices of HSA, compared to normal individual. Structural changes of glycated HSA to the β -structure and nanofibril formation has been reported previously [21]. In our previous in vitro study [19], it was shown that some AGEs are fluorescent with maximum emission wavelengths at 431, 440, 453, and 460 nm at correspondence excitation maximum of 322, 342, 352, 375 and 381 nm, respectively. Thus, all these five excitation/emission wavelengths were used for the detection of AGE fluorescence in purified HSA and in vitro samples. Fig. 3(a) shows these alterations for purified albumin from normal and diabetic human serum. Also, Fig. 3(b) and (c) show these alterations for in vitro glycated albumins after 14 and 28 days incubation. As it is shown in the figures, AGE-specific fluorescence was found to increase following by increasing the sugar concentration in serum of diabetic patient as well as in vitro condition.

Another more interesting method to follow the formation of AGE is the detection of lysine and arginine side chains modification. Extensive modification to lysine side chains and minor modification to arginine side chains have been found to occur during the AGE-formation process with glucose in albumin [26]. Free lysine and arginine residues were measured by TNBSA [26] and 9, 10-phenanthrenequinone [27] reagents, respectively. Figs. 4 show the number of reacted lysine and arginine residues in each HSA molecule of samples. The number of free lysine and arginine residues in diabetic patients decreased upon increasing the level of glucose in serum, compared to the normal individual.

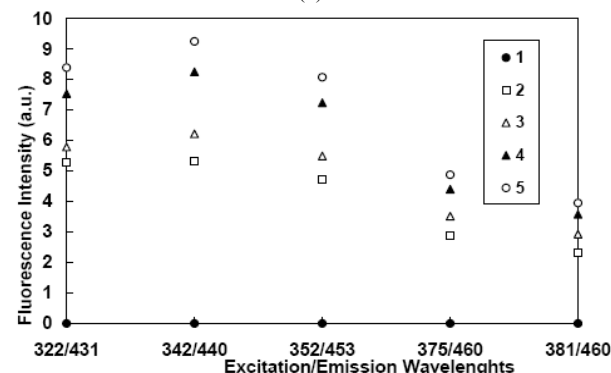
Also, Figs. 4 show a decrease in the level of free lysine residue in glycated albumin in vitro. However, the numbers of free arginine do not change in these in vitro samples.



(a)



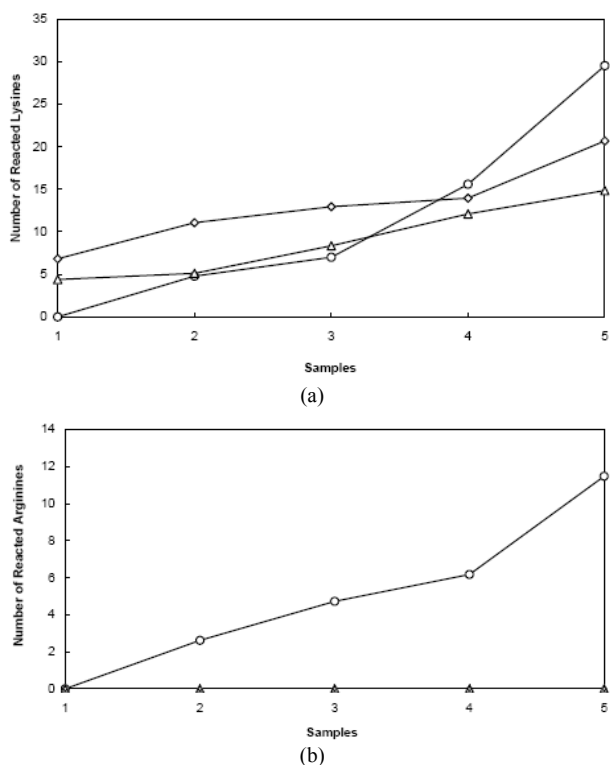
(b)



(c)

Fig. 3. Fluorescence intensity ratio of excitation/emission at different wavelengths (322/431, 342/440, 352/453, 375/460, 381/460) for samples of HSA that were a) purified from human serum, b) in vitro glycated samples after 14 days incubation and c) in vitro glycated samples after 28 days incubation, in phosphate buffer, pH 7.4, with (1) < 100, (2) 150-200, (3) 200-250, (4) 300-350 and (5) >400 mg/dl sugar concentration

This study shows that in the sample of HSA incubated for 35 days in the presence of 500 mM glucose, approximately 2 out of 25 arginine residues in HSA were modified. Also, the results show that in diabetic patient with the sugar concentration more than 400 mg/dl, approximately 63% and 46% of lysine and arginine residues are modified, respectively (Figs. 4). Previous investigations showed that 3-deoxyglucosone, a 1,2-dicarbonyl compound derived from glucose, reacts with arginine in albumin under physiological conditions, whereas glucose itself reacts more extensively with lysine [26].



Figs. 4. Number of reacted lysine residues, and b) arginine residues for HSA samples which were purified from human serum (°) and in vitro glycated samples (Δ , \diamond) after 14 days incubation (Δ) and after 28 days incubation (\diamond) in phosphate buffer, pH 7.4, with (1) <100, (2) 150-200, (3) 200-250, (4) 300-350 and (5) >400 mg/dl sugar concentration.

Another criterion for glycation reaction is generation of ketoamines that called as Amadori products which is detected using fructosamine assay [26]. In this assay, Amadori product (ketoamines) can reduce NBT reagent and then produce colored formazan dye with an absorption maximum at 530 nm. In Fig. 5, formation of formazan dye in purified HSA and in vitro samples in different glucose concentrations were compared. The results reflect the presence of Amadori products which the extent of this Amadori product increases by increasing the level of glucose in serum and in incubation medium.

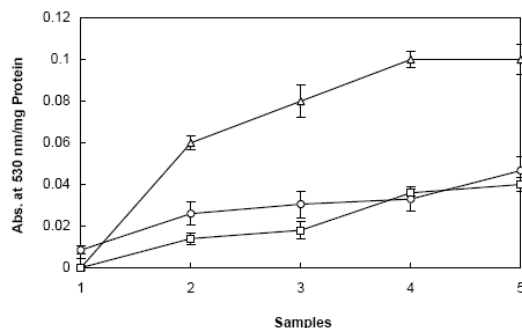


Fig. 5. Amount of Amadori products formed per milligram of HSA for samples which were purified from human serum (°) and in vitro glycated samples (Δ , \diamond) after 14 days incubation (Δ) and after 28 days incubation (\diamond) in phosphate buffer, pH 7.4, with (1) <100, (2) 150-200, (3) 200-250, (4) 300-350 and (5) >400 mg/dl sugar concentration

During the glycation process, the modification of protein structures by the carbohydrates and the interaction of carbohydrates with the proteins affect the surface rheology of globular proteins adsorbed at an air-water interface. Fig. 6 shows the values of surface tension of purified HSA (1 mg/ml) with different levels of sugar in serum (measurements were performed at 25°C).

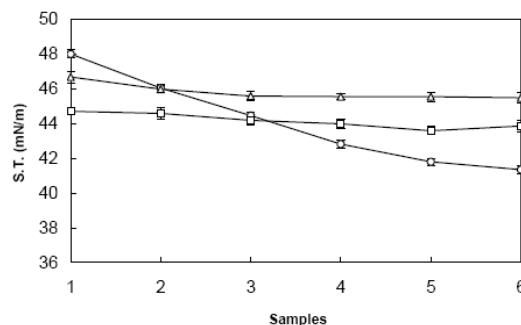


Fig. 6. Surface tension of 1 mg/ml samples of HSA which were purified from human serum (°) and in vitro glycated samples (Δ , \diamond) after 14 days incubation (Δ) and after 28 days incubation (\diamond) in phosphate buffer, pH 7.4, with (1) <100, (2) 150-200, (3) 200-250, (4) 300-350 and (5) >400 mg/dl sugar concentration

The surface tension of 1 mg/ml HSA of normal individual was approximately 48 mN/m. Increasing the level of sugar concentration in serum led to decrease surface tension in two conditions. Glycation of lysine and arginine residues and perhaps other charged and hydrophilic amino acids may also results in an alteration in hydrophobicity/hydrophilicity of the surface of the protein and induced decreasing surface tension.

IV. Discussion and Conclusion

Based on the obtained results, a comparison of the characteristics of glycated HSA in vitro and those observed in vivo, indicates that structural changes of HSA in diabetic patients is compatible with that obtained from in vitro condition. Increasing the sugar concentration or the degree of hyperglycemia leads to a decrease in the content of α -helices of HSA, level of free lysine residue and surface tension values and an increase in AGE-specific fluorescence intensity and the Amadori product formation. The only difference was about the modification of arginine residues. Glucose reacts more extensively with lysine. However, derived compound from glucose under physiological conditions: 3-deoxyglucosone and 1,2-dicarbonyl compounds, react with arginine residue in vivo.

Acknowledgements

The financial support of the Research Council of the Shiraz University of Medical Sciences and the Iran National Science Foundation (INSF) are gratefully acknowledged.

References

- [1] R.G. Khalifah, J.W. Baynes, B.G. Hudson, Amadorins: novel post-Amadori inhibitors of advanced glycation reactions, *Biochem. Biophys. Res. Commun. Volume 257*, 1999, Pages 251-258.
- [2] A. Lapolla, P. Traldi, D. Fedele, Importance of measuring products of non-enzymatic glycation of proteins, *Clin. Biochem. Volume 38*, 2005, Pages 103-115.
- [3] N. Shaklai, R.L. Garlick, H.F. Bunn, Nonenzymatic glycosylation of human serum albumin alters its conformation and function, *J. Biol. Chem. Volume 259*, 1984, Pages 3812-3817.
- [4] P.A. Voziyan, R.G. Khalifah, C. Thibaudeau, A. Yildiz, J. Jacob, A.S. Serianni, B.G. Hudson, Modification of proteins In Vitro by physiological levels of glucose, *J. Biol. Chem. Volume 278*, 2003, Pages 46616-46624.
- [5] B.L. Cussimano, A.A. Booth, P. Todd, B.G. Hudson, R.G. Khalifah, Unusual susceptibility of heme proteins to damage by glucose during non-enzymatic glycation, *Biophys. Chem. Volume 105*, 2003, Pages 743-755.
- [6] B. Trueb, C.G. Holenstein, R.W. Fischer, K.H. Winterhalter, Nonenzymatic glycosylation of proteins, *J. Biol. Chem. Volume 255*, 1980, Pages 6717-6720.
- [7] X.M. He, D.C. Carter, Atomic structure and chemistry of human serum albumin, *Nature Volume 358*, 1992, Pages 209-215.
- [8] D.C. Carter, X.M. He, S.H. Munson, P.D. Twigg, K.M. Gernert, M.B. Broom, T.Y. Miller, Three-dimensional structure of human serum albumin, *Science, Volume 244*, 1989, Pages 1195-1198.
- [9] E. Bourdon, N. Loreau, D. Blache, Glucose and free radicals impair the antioxidant properties of serum albumin, *FASEB J., Volume 13*, 1999, Pages 233-243.
- [10] N. Iberg, R. Fluckiger, Nonenzymatic glycosylation of albumin in vitro (Identification of multiple glycosylated sites), *J. Biol. Chem. Volume 261*, 1986, Pages 13542-13545.
- [11] P.J. Coussons, J. Jacoby, A. McKay, S.M. Kelly, N.C. Price, J. V. Hunt, Glucose modification of human serum albumin: a structural study, *Free Radical Biol. Med. Volume 22*, 1997, Pages 1217-1227.
- [12] S.D. Sharma, B.N. Pandey, K.P. Mishra, S. Sivakami, Amadori product and AGE formation during nonenzymatic glycosylation of bovine serum albumin In Vitro, *J. Biochem. Mol. Biol. Biophys. Volume 6*, 2002, Pages 233-242.
- [13] N. Shaklai, R.L. Garlick, H.F. Bunn, Nonenzymatic glycosylation of human serum albumin alters its conformation and function, *J. Biol. Chem. Volume 259*, 1984, Pages 3812-3817.
- [14] D.M. Mendez, R.A. Jensen, L.A. McElroy, J.M. Pena, R.M. Esquerra, The effect of non-enzymatic glycation on the unfolding of human serum albumin, *Arch. Biochem. Biophys. Volume 444*, 2005, Pages 92-99.
- [15] H. Zoellner, Y.H. Hou, T. Hochgrebe, A. Poljak, M.W. Duncan, J. Golding, T. Henderson, G. Lynch, Fluorometric and mass spectrometric analysis of nonenzymatic glycosylated albumin, *Biochem. Biophys. Res. Commun. Volume 284*, 2001, Pages 83-89.
- [16] B. Bouma, L.M.J. Kroon-Batenburg, Y.P. Wu, B. Brunjes, G. Posthuma, O. Kranenburg, P.G. Groot, E.E. Voest, M.F.B.G. Gebbink, Glycation induces formation of amyloid cross- β structure in albumin, *J. Biol. Chem. Volume 278*, 2003, Pages 41810-41819.
- [17] M.E. Westwood, P.J. Thornalley, Molecular characteristics of methylglyoxal-modified bovine and human serum albumins. Comparison with glucose-derived advanced glycation end product-modified serum albumins, *J. Protein Chem. Volume 4*, 1995, Pages 359-372.
- [18] K.M. Biemel, D.A. Friedl, M.O. Lederer, Identification and quantification of major Maillard cross-links in human serum albumin and lens protein, *J. Biol. Chem. Volume 277*, 2002, Pages 24907-24915.
- [19] N. Sattarahmady, A.A. Moosavi-Movahedi, F. Ahmad, G.H. Hakimelahi, M. Habibi-Rezaei, A.A. Saboury, N. Sheibani, Formation of the Molten Globule-Like State during Prolonged Glycation of Human Serum Albumin, *Biochim. Biophys. Acta Volume 1770*, 2007, Pages 933-942.
- [20] N. Sattarahmady, F. Khodaghali, A.A. Moosavi-Movahedi, H. Heli, G.H. Hakimelahi, Alginate as antiglycating agent for human serum albumin, *Int. J. Biol. Macromol. Volume 41*, 2007, Pages 180-184.
- [21] N. Sattarahmady, A.A. Moosavi-Movahedi, M. Habibi-Rezaei, S. Ahmadian, A.A. Saboury, H. Heli, N. Sheibani, Detergency effect of nanofibrillar amyloid formation on glycation of human serum albumin, *Carbohydrate Res. Volume 343*, 2008, Pages 2229-2234.
- [22] Z.Y. Ma, Y.P. Guan, H.Z. Liu, Affinity adsorption of albumin on Cibacron Blue F3GA-coupled non-porous micrometer-sized magnetic polymer microspheres, *React. Funct. Polym. Volume 66*, 2006, Pages 618-624.
- [23] D.J. Ledden, R.C. Feldhoff, S.K. Chan, Characterization of fragments of human albumin purified by Cibacron Blue F3GA affinity chromatography, *Biochem. J. Volume 205*, 1982, Pages 331-337.
- [24] U.K. Laemmli, Cleavage of structural proteins during the assembly of the head of bacteriophage T4, *Nature, Volume 227*, 1970, Pages 680-685.
- [25] C. Wilson, Staining of proteins on gels: comparison of dyes and procedures, *Methods Enzymol, Volume 91*, 1983, Pages 236-247.
- [26] A. Schmitt, J. Schmitt, G. Munch, J. Gasic-Milencovic, Characterization of advanced glycation end products for biochemical studies: side chain modifications and fluorescence characteristics, *Anal. Biochem. Volume 338*, 2005, Pages 201-215.

Authors' information

^{1*}Department of Biochemistry, Shiraz University of Medical Sciences, Shiraz, Iran. To whom correspondence should be addressed. Email address: sattarahmady@yahoo.com, Tel: +98 711 2303029, Fax: +98 711 2303029.

² Institute of Biochemistry and Biophysics, University of Tehran, Tehran, Iran.

³ School of Biology, College of Science, University of Tehran, Tehran, Iran.

⁴ Department of chemistry, Islamic Azad University, Fars Science and Research Branch, Marvdasht, Iran.

N. Sattarahmady received her BSc in cell and molecular biology from University of Tehran, MSc in biophysics from Institute of Biochemistry and Biophysics, University of Tehran and her PhD in biophysics from Institute of Biochemistry and Biophysics, University of Tehran. She is an assistant professor of biophysics at Shiraz University of Medical Sciences. Her current interests include protein structure and design of nanostructured materials for encapsulation and drug delivery.

A.A. Moosavi-Movahedi received his BSc in chemistry in 1975 from Shahid Beheshti University, MSc in chemistry in 1978 from Michigan University and obtained his PhD in biophysical chemistry in 1986 from Manchester University. He is a professor of biophysical chemistry at Institute of Biochemistry and Biophysics, University of Tehran. His main area of interest is biophysical chemistry of biological macromolecules.

M. Habibi-Rezaei received his PhD in biochemistry from Institute of Biochemistry and Biophysics, University of Tehran. He is an assistant professor of biochemistry at Tehran University.

H. Heli received his BSc in chemistry in 1999 from K.N. Toosi University of Technology, MSc in analytical chemistry in 2001 from Tarbiat Modares University and obtained his PhD in electrochemistry in 2004 from K.N. Toosi University of Technology. He is currently an assistant professor in chemistry at Islamic Azad University, Fars Science and Research Branch, Marvdasht. His major interests are synthesis of new nanostructured and targeted materials and their applications in bioelectrocatalysis, biosensors and bioactive delivery systems.

Purine Nucleoside Phosphorylase as a Molecular Target to Develop Active Compounds Against *Mycobacterium Tuberculosis*

Rodrigo G. Ducati¹, André A. Souto¹, Rafael A. Caceres², Walter F. de Azevedo Jr.³,
Luiz A. Basso^{1,*}, Diógenes S. Santos^{1,*}

Abstract – Despite the availability of chemotherapeutic and prophylactic approaches to fight consumption, human tuberculosis (TB) continues to claim millions of lives annually, mostly in developing nations, generally due to limited resources available to ensure proper treatment and where human immunodeficiency virus infections are common. Moreover, rising drug-resistant cases have worsened even further this picture. Accordingly, new therapeutic approaches have become necessary. The use of defined molecular targets could be explored as an attempt to develop new and selective chemical compounds to be employed in the treatment of TB. The present review highlights purine nucleoside phosphorylase, a component enzyme of the purine salvage pathway, as an attractive target for the development of new antimycobacterial agents, since this enzyme has been numbered among targets for *Mycobacterium tuberculosis* persistence in the human host. Enzyme kinetics and structural data are discussed to provide a basis to guide the rational anti-TB drug design. **Copyright © 2010 Praise Worthy Prize S.r.l. - All rights reserved.**

Keywords: Enzyme Kinetics and Structural Analysis, Human Tuberculosis, *Mycobacterium Tuberculosis*, Purine Nucleoside Phosphorylase, Rational Drug Development

I. Introduction

Human tuberculosis (TB), mainly due to *Mycobacterium tuberculosis* infection, remains a leading cause of mortality due to a single infectious agent. This aerobic pathogenic bacterium usually establishes its infection in the lungs, and its progression is fundamentally regulated by the integrity of the host's immune system. This disease is mostly distributed among developing nations, generally due to limited resources available to ensure proper treatment and where human immunodeficiency virus infections are common.

From a historic point of view, the introduction of effective chemotherapeutic and prophylactic measures against TB have drastically reduced human deaths worldwide. However, history has also given us clear evidence that this is no longer true. This versatile infectious agent has evolved to adapt to the conditions imposed by the human host to survive. The resumption of consumption has been basically attributed to the recent generation of drug-resistant strains, capable of overcoming the chemical action of the currently administered agents, and thereby, being associated to greater morbidity and mortality [1].

Clearly, new approaches to combat TB have become needed. The use of defined molecular targets could be explored as an attempt to develop new and selective chemical compounds to be employed in the treatment of this disease.

Particular features of this pathogen, such as enzymes from fundamental metabolic pathways with unique characteristics when compared to the human host could be evaluated to direct efforts towards target-based drug development [2]–[5].

The present review is focused on *M. tuberculosis* purine nucleoside phosphorylase (PNP; EC 2.4.2.1), a component enzyme of purine salvage pathway [3]. *M. tuberculosis* PNP is an attractive target for the development of new antimycobacterial agents, as it has been numbered among targets for *M. tuberculosis* persistence in humans (www.webtb.org). Enzyme kinetics and structural data have been included to provide a thorough knowledge on which to base the search for compounds with biological activity.

II. Selective Drug Development

II.1. Defining a Molecular Target

The complete genome sequencing of *M. tuberculosis* H37Rv strain [6] has made a decisive contribution to the field of research on TB, offering the scientific community a databank on which to explore singular features of this pathogen, thereby establishing a new phase in the battle against this pathogen. This particular strain has had a great application in biomedical research worldwide due to total virulence retention in animal

models, besides being susceptible to drugs and amenable to genetic manipulation [6].

The identification and validation of microbial essential pathways are important as a first step towards specific inhibitor design with low toxicity [7], since their component enzymes can be evaluated as possible targets for drug development. Homologues to enzymes of the purine salvage pathway have been identified in the genome sequence of *M. tuberculosis* H37Rv [6]. This pathway represents an essential cellular process that is critical for many organisms [8]. Since purine metabolism has been implicated in mycobacterial latency [9][10], it may offer a great opportunity to gather knowledge on a defined molecular target on which to base rational drug development efforts.

II.2. The Candidate

PNP, a component enzyme of the purine salvage pathway [3], plays a critical role in the reversible phosphorolysis of the *N*-glycosidic bond of β -purine (deoxy)ribonucleosides to generate α -(deoxy)ribose 1-phosphate (R1P) and the corresponding purine bases [8][11]. Irrespective of the cellular origin, PNPs have been structurally subdivided according to their quaternary structures into the homotrimeric (low molecular weight; PNP-I) and homo-hexameric (high molecular weight; PNP-II) classes. Substrate specificities are considerably dissimilar among these classes, as a consequence of the substantial divergence of residue composition at the catalytic site [12][13]. Homotrimeric PNPs are highly specific for 6-oxopurines, their nucleosides, and some analogues; whereas homo-hexameric PNPs additionally accept 6-aminopurines, their nucleosides, and many analogues [13].

The enzyme from *M. tuberculosis* (MtPNP), encoded by the *deoD* gene (Rv3307, 807 bp, 268 aa, 27539.4 Da, and pI = 5.75), alternatively named *punA*, is a member of the trimeric class [14]. This class includes the human (HsPNP) and bovine homologues, among others. PNPs belonging to the trimeric class differ significantly from the hexameric class, which is usually present in prokaryotes [13][15][16]. The mycobacterial homologue is more specific to natural 6-oxopurine nucleosides (inosine, deoxyinosine, guanosine, and deoxyguanosine (2dGuo)) and synthetic compounds, and does not catalyze adenosine phosphorolysis [17]. This substrate specificity is in agreement with the concept that homotrimeric PNP enzymes cannot catalyze phosphorolysis and/or synthesis of 6-aminopurine nucleosides to an appreciable extent [18][19]. Although MtPNP has been numbered among the top 100 persistence targets by the TB Structural Genomics Consortium (www.webtb.org), its physiological role in *M. tuberculosis* remains to be demonstrated. Gene replacement experiments have been carried out to produce mutant strains defective in functional PNP.

Surprisingly, *deoD*-encoded MtPNP appears to play an essential role in the survival of bacteria grown in rich medium, since a knockout strain could not be generated due to the unexpected essentiality of the gene (unpublished results). This result underscores the need for demonstrating protein function by experimental approaches instead of assigning function to a particular gene product based only on comparative data.

II.3. Selective Approach

A number of research groups have dedicated their efforts to determine specificity of substrates, kinetic mechanisms, and three-dimensional structures for PNPs from different bacterial sources [12][14][17][20]-[25] in comparison to HsPNP. Even though PNP activity is shared between humans and *M. tuberculosis*, drugs with selective toxicity against the mycobacterial enzyme can still be developed if one takes advantage of singular features that make them dissimilar [26]. In accordance with this proposal, it has recently been shown that even though bovine and human homologues share 87% sequence identity and have full conservation of the active site residues, inhibitors with differential specificity can be designed [27]. Although the mycobacterial and human homologues share 34.81% identity in amino acid sequence, the design of inhibitors with higher affinity for MtPNP seems to be feasible, since they appear to have different transition states [28] and structural features [25][29][30], which may be exploited to achieve specificity [24][31]-[39].

III. Enzyme Kinetics

MtPNP substrate specificity was probed by measurements of initial velocity employing natural and synthetic substrates [17]. The enzyme proved to be more specific for synthetic guanosine N7 methyl analogues, 2-amino-6-mercapto-7-methylpurine ribonucleoside (MESG) and 7-methylguanosine, than to natural nucleosides. This has been attributed to the increased catalytic constant values, since K_M values for all substrates were of similar magnitude. It is important to notice that the K_M value for MESG [17] was approximately 12-fold smaller than the one observed for HsPNP [39]. Indeed, the human homologue was shown to be more specific for natural substrates, such as inosine and guanosine, than to MESG [39]. These differences might imply that compounds with selective activity against MtPNP may be developed based on chemical functional group substitutions of MESG, in particular the sulfur at the sixth position of the purine base.

Initial velocity, product inhibition, and equilibrium binding (spectrofluorimetry and surface plasmon resonance) data suggested that MtPNP catalyzes the phosphorolysis of 2dGuo by a steady-state ordered bi bi kinetic mechanism, in which inorganic phosphate (PO_4) is the first substrate to bind to the enzyme followed by

2dGuo binding to form the catalytically competent ternary complex, and R1P is the first product to dissociate from the enzyme followed by the dissociation of guanine (Gua) (Fig. 1).



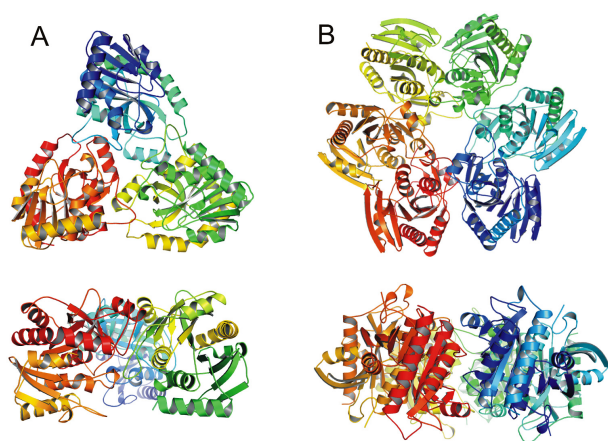
Fig. 1. Proposed enzyme kinetic mechanism for MtPNP with 2dGuo

pH-rate profiles indicated a general acid as being essential for both catalysis and 2dGuo binding, and deprotonation of a group abolished phosphate binding. Proton inventory and solvent deuterium isotope effects indicated that a single solvent proton transfer makes a modest contribution to the rate-limiting step. Pre-steady-state kinetic data indicated that product release appears to contribute to the rate-limiting step for the MtPNP-catalyzed reaction [17].

IV. Crystallographic Structure

IV.1. Overall Structure Description

MtPNP is composed predominantly of alanine (17.5%), leucine (12.3%), valine (10.1%), and glycine (10.4%) residues. As previously mentioned, PNPs with differing specificities have been identified, and, in a number of instances, purified from a broad range of organisms. Whereas most PNPs derived from bacteria are hexameric, MtPNP is a symmetrical homotrimer with a triangular arrangement of subunits similar to the mammalian PNP structures [24] (Figs. 2).



Figs. 2. Structures for (A) trimeric PNP (PDB: 1G2O) and (B) hexameric PNP (PDB: 1NW4)

In 2001, Wuxian Shi and co-workers solved, for the first time, the structures of MtPNP complexed with Immucillin-H (ImmH) and PO_4 and complexed with Iminoribitol, 9-deazahypoxanthine, and PO_4 . These crystallographic structures were deposited on the Protein Data Bank (PDB) under the codes 1G20 and 1I80 [24], respectively. These structures provided a detailed picture of the catalytic conformation of MtPNP upon transition

state binding.

Each monomer of the protein is folded into a single domain structure (α/β) containing nine β strands and nine α helices (Fig. 3). The core consists of a mixed eight-stranded β sheet ($\beta 2$, Thr50-Gln54; $\beta 3$, Gly70-Ile77; $\beta 4$, His80-Glu87; $\beta 1$, Val30-Leu34; $\beta 5$, Gln113-Leu124; $\beta 9$, Gln222-Thr230; $\beta 6$, Gln132-Leu142; and $\beta 7$, Ala176-Leu183). $\beta 5$ and $\beta 9$ are extended and participate in a smaller five-stranded distorted β barrel ($\beta 9$; $\beta 5$; $\beta 8$; Asp203-Gly206; $\beta 7$; and $\beta 6$). The β sheet core is flanked by several α helices on each side ($\alpha 1$, Pro8-Thr23; $\alpha 2$, Val42-Ala44; $\alpha 3$, Arg98-Tyr99; $\alpha 4$, Pro103-Ser110; $\alpha 5$, Pro162-Ser171; $\alpha 6$, Pro191-Leu200; $\alpha 7$, Val210-Ala219; $\alpha 8$, His243-Ala251; and $\alpha 9$, Thr255-Arg267). Note that all secondary structural elements described here were identified using the molecular modeling software SPBDV v.4.0 [40]. These secondary structural elements are linked by extended loops, a characteristic feature common to all PNP structures solved to date. The segment connecting $\beta 2$ and $\beta 3$ (residues Ala55-Ala69) presents a disordered loop in MtPNP:ImmH: PO_4 , although the authors reported that this loop was built into clear electron density in the $F_o - F_c$ electron density map. However, if compared to other structures (3IOM [25], 1I80 [24], and MtPNP:hypoxanthine (to be published elsewhere)), this loop presents a high root mean squared deviation of 8.21 Å, 8.44 Å, and 8.23 Å, respectively. The residues from this loop do not interact directly with bound inhibitor or phosphate, but are involved in the orientation of side chains of the residues in the catalytic sites [24].

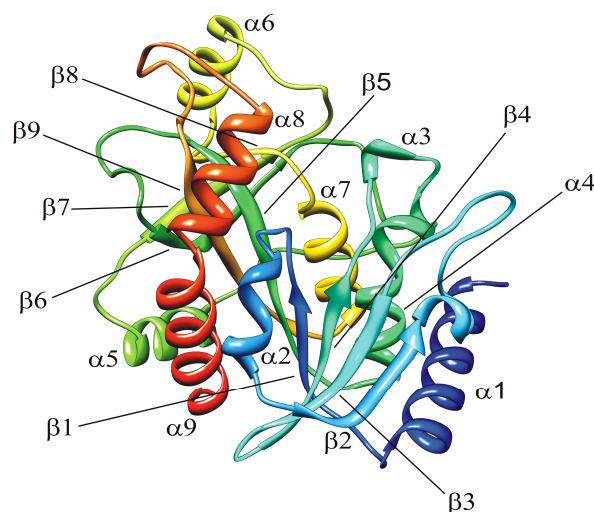


Fig. 3. Ribbon diagram of MtPNP showing the secondary structure (PDB: 3IOM)

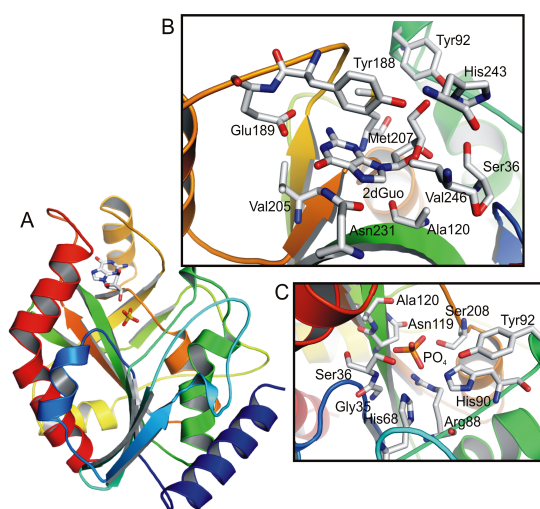
Contacts between each subunit involve residues from Loop4 (Ala65), Loop5 (Tyr92-Glu93), $\beta 6$ (Asp138-Leu142), Loop7 (Thr143-Ala159), $\beta 7$ (Val179), Loop8- $\alpha 6$ (Pro184-Leu200), Turn (Met207), $\alpha 7$ (Ile214), and Loop9- $\alpha 8$ (Ala234-His243). The seven hydrogen bond interactions at the subunit interfaces include Tyr92(A) O-N Gly150(B), His187(A) ND1-OG Ser146(B),

Tyr188(A) N-O Val154(B), Leu241(A) N-OD1 Asp155(B), Ala192(A) N-OD2 Asp138(B), Thr190(A) OG-O His139(B), and Glu193(A) OE2-N Asn141(B). The hydrophobic van der Waals interactions involve the pairs Tyr92(A)-Phe153(B), Tyr188(A)-Phe153(B), His243(A)-Phe153(B), His187(A)-Ile214(B), His187(A)-Leu156(B), Thr190(A)-Asp138(B), Thr190(A)-His139(B), Ala192(A)-Asp138(B), Glu193(A)-Leu140(B), and Met196(A)-Leu142(B).

In the trimeric PNPs, the entire active site is buried in the protein structure, and can be divided into three parts: the phosphate-binding site, in some crystallographic structures occupied by sulfate (used in high concentration in the crystallization conditions), and the pentose- and base-binding sites. The active site of each monomer is located in the interface of dimers. One active site in each dimer is located on the top and one on the bottom of the macromolecule. The distance between the active sites in each dimer is ~ 30 Å. At least two monomers are necessary to constitute a functional catalytic unit.

IV.2. Phosphate-binding Site

The phosphate-binding site (Fig. 4C) is characterized by a cluster of positive charges comprised of Gly35, Ser36, His68, Arg88, His90, Tyr92, Asn119, Ala120, and Ser208 residues. In MtPNP, most of these residues are in loops, except Asn119 and Ala120, which is part of $\beta 5$, and Ser208, which is in a turn. All sulfate (phosphate) oxygen atoms form at least three intermolecular hydrogen bonds or salt bridges with the protein. The phosphate (sulfate) anion is also in contact with oxygen O3' and nitrogen N1' of the pentose ring moiety of ImmH (1G2O [24] and 1N3I [28]). No residues from the adjacent monomer interact with the phosphate-binding site as occurs in other organisms [13].



Figs. 4. Ligand-binding sites of MtPNP. (A) Monomer of MtPNP (PDB: 3IOM) complexed with sulfate and 2dGuo. (B) Pentose- and base-binding sites (PDB: 3IOM). (C) Phosphate-binding site (PDB: 1G2O)

Molecular dynamics simulations of the phosphate-binding site of *Plasmodium falciparum* PNP demonstrated that it is more stable than the purine-binding site [41], and could thus become an alternative site for the design of new inhibitors as observed for HsPNP [29].

IV.3. Pentose- and Base-binding Sites

Up to date, four crystallographic structures of MtPNP have been solved and deposited in PDB (1G2O [24], 1I80 [24], 1N3I [28], and 3IOM [25]). However, only 3IOM was solved in complex with a natural substrate. The pentose- and base-binding sites are located close to the phosphate-binding site, and share some amino acid residues, such as Ser36, Tyr92, Ala120, and Ser208. The structure of MtPNP in complex with sulfate and 2dGuo [25] gives a detailed view of the pentose- and base-binding sites. A number of hydrophobic residues are found in the base-binding site, such as Val205, Met207, and Val246. The amino acid residues in MtPNP pentose- and base-binding sites are shown in Fig. 4B. There are six intermolecular hydrogen bonds between the protein and 2dGuo, two between the pentose ring, and four with the base moiety. Hydrogen bond interactions with the sugar moiety involve Ser36 OG-O2 2dGuo and His243 ND1-O3 2dGuo; and Glu189 OE1-N4 2dGuo, Glu189 OE2-N5 2dGuo, Asn231 OD1-N3 2dGuo, and Asn231 OD2-O4 2dGuo with the guanine base moiety. However, in the structure of MtPNP:sulfate:2dGuo ternary complex, we did not observe the presence of Phe153 of adjacent subunit in the active binding site making hydrophobic contact and therefore no involvement in π - π interactions with the base moiety, as observed in other trimeric PNP-I enzymes [13].

IV.4. Structure-based Drug Design

Protein crystallography is an essential tool for the discovery and investigation of pharmacological interactions at the molecular level. The crystallographic structure of MtPNP provides valuable information for the structure-based design of antimycobacterial drugs, since it captures the features of an active binding site. However, it was shown that the pentose- and base-binding sites can accommodate molecular structures that are different from its natural substrates, so caution should be kept in mind when molecular docking simulations is carried out in order to find enzyme selective inhibitors [25]. The development of new potent selective inhibitors for MtPNP is still a scientific endeavor as they may present high toxicity, making them inappropriate for human administration. Accordingly, efforts to develop drugs with selective toxicity based on structural differences between MtPNP and HsPNP should be pursued. A number of research groups have thus included computational tools to achieve this goal.

V. Potent Inhibitors of PNP

Potent inhibitors of PNPs are largely structural analogues of nucleoside substrates, embracing modifications of the base and/or pentose moiety, as well as replacement of the latter by other cyclic or acyclic moieties. The first structural changes only considered the ground state to the development of new inhibitors, obtaining IC_{50} values which ranged from 0.75 to 5 nM for PNP from mammalian erythrocytes [13]. The most outstanding molecule was 9-(3-pyridinyl-methyl)-9-deazaGua (BCX-34; Fig. 5), which is a potential candidate for the treatment of human T-cell proliferative disorders [42].

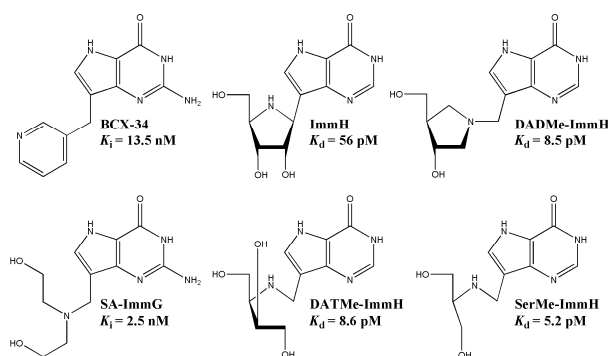


Fig. 5. Chemical structures of PNP inhibitors

However the most potent inhibitors were designed from extensive kinetic isotope effect studies of transition states on the phosphorolysis reaction of inosine [43]. The first inhibitors based on the transition state structure were derived from (1*S*)-1-(9-deazahypoxanthin-9-yl)-1,4-dideoxy-1,4-imino-D-ribitol (ImmH; Fig. 5) and presented IC_{50} values ranging from 0.48 to 1.57 nM in mammalian hosts, including mice, monkeys, and humans. These compounds were further shown to be effective for T-cell selective immunosuppression, and clinical trials are ongoing [44]. It was also found that the inhibition mechanism is slow-onset, tight-binding with equilibrium dissociation constants (K_d) in the pM range (23 to 72 pM) [45].

As the transition state structures of PNPs-catalyzed phosphorolysis were determined, the Immucillin of second generation was synthesized, with $K_d = 8.5$ pM (DADMe-ImmH; Fig. 5). The structural changes were nitrogen atom by anomeric carbon, the ring oxygen by a methylene group to mimic the pentosyl moiety in the transition state. The 9-methylene bridge served to place the cationic N1' nitrogen near the ribosyl C1' position in the transition state and the 2'-hydroxyl group was removed to provide chemical stability [46]. Scaling up synthesis of DADME-ImmH has also been shown to be feasible [47].

In 2006, when seeking to simplify the Immucillin analogues, Corelli and co-workers [48] synthesized a series of acyclic Immucillin analogues (SA-ImmG; $K_i = 2.5$ nM; Fig. 5), which had a dissociation constant

similar to the first generation of Immucillins. These acyclic derivatives made synthesis easy and low-cost which is fundamental to industrial scale-up. Based on these findings, an acyclic Immucillin series was further increased and the most active compound was DATMe-ImmH (Fig. 5). It was named third generation of PNP inhibitors with $K_d = 8.6$ pM [49].

More recently, a fourth generation of transition state analogues has been presented [50], of which the most active compound is SerMe-ImmH, with $K_d = 5.2$ pM (Fig. 5). It was demonstrated by isothermal titration calorimetry studies that the conformationally flexible Immucillins reduced the system entropic penalty [51]. This inhibitor is structurally achiral, reducing the challenge for synthesis in large scale.

Regarding MtPNP, when only derivatives were evaluated, ImmH and DADMe-ImmH and their dissociation constants were 650 and 42 pM, respectively [28]. If we compare the transition states and substrate specificities of various PNPs, it appears to be possible to design species-specific inhibitors for use as therapeutic agents [52]. This seems feasible as we compare the K_i of HsPNP (56 pM) and MtPNP (650 pM). However, for DADMe-ImmH the difference is less pronounced: 16 pM for HsPNP and 42 pM for MtPNP. It has been proposed that changes in DADMe-ImmH are better to mimic the late transition state characteristic of the human enzyme catalyzed phosphorolysis [52].

VI. Conclusion

The present review strives to offer a brief review on current scientific data on MtPNP to provide insights on which to base selective drug development. As PNP-catalyzed phosphorolysis reaction is shared between humans and mycobacteria, differences in functional and structural features have been discussed to exploit them to achieve specificity.

Acknowledgements

This work was supported by funds of Millennium Initiative Program and National Institute of Science and Technology on Tuberculosis (INCT-TB), MCT-CNPq, Ministry of Health - Department of Science and Technology (DECIT) - Secretary of Health Policy (Brazil) to D.S.S., L.A.B and W.F.A.Jr. D.S.S. (CNPq, 304051/1975-06), L.A.B. (CNPq, 520182/99-5) and W.F.A.Jr. (CNPq, 300851/98-7) are Research Career Awardees of the National Research Council of Brazil (CNPq). R.G.D. and R.A.C. are postdoctoral fellows of CNPq.

References

- [1] R.G. Ducati, A. Ruffino-Netto, et al., The resumption of consumption - a review on tuberculosis, *Memórias do Instituto*

- Oswaldo Cruz, Volume 101, (Issue 7), November 2006, Pages 697-714.
- [2] R.G. Ducati, L.A. Basso, et al., Mycobacterial shikimate pathway enzymes as targets for drug design, *Current Drug Targets*, Volume 8, (Issue 3), March 2007, Pages 423-435.
 - [3] R.G. Ducati, A. Breda, et al., Purine Salvage Pathway in *Mycobacterium tuberculosis*, *Current Medicinal Chemistry*, Accepted for publication, 2010.
 - [4] A.D. Villela, Z.A. Sánchez-Quitian, et al., Pyrimidine Salvage Pathway in *Mycobacterium tuberculosis*, *Current Medicinal Chemistry*, Accepted for publication, 2010.
 - [5] Z.A. Sánchez-Quitian, C.Z. Schneider, et al., Structural and functional analyses of *Mycobacterium tuberculosis* Rv3315c-encoded metal-dependent homotetrameric cytidine deaminase, *Journal of Structural Biology*, Volume 169, (Issue 3), March 2010, Pages 413-423.
 - [6] S.T. Cole, R. Brosch, et al., Deciphering the biology of *Mycobacterium tuberculosis* from the complete genome sequence, *Nature*, Volume 393, (Issue 6685), June 1998, Pages 537-544.
 - [7] K. Duncan, Progress in TB drug development and what is still needed, *Tuberculosis (Edinburgh, Scotland)*, Volume 83, (Issue 1-3), 2003, Pages 201-207.
 - [8] H.M. Kalckar, Differential spectrophotometry of purine compounds by means of specific enzymes; determination of hydroxypurine compounds, *The Journal of Biological Chemistry*, Volume 167, (Issue 2), February 1947, Pages 429-443.
 - [9] A.K. Ojha, T.K. Mukherjee, et al., High intracellular level of guanosine tetraphosphate in *Mycobacterium smegmatis* changes the morphology of the bacterium, *Infection and Immunity*, Volume 68, (Issue 7), July 2000, Pages 4084-4091.
 - [10] T.P. Primm, S.J. Andersen, et al., The stringent response of *Mycobacterium tuberculosis* is required for long-term survival, *Journal of Bacteriology*, Volume 182, (Issue 17), September 2000, Pages 4889-4898.
 - [11] D.J. Porter, Purine nucleoside phosphorylase. Kinetic mechanism of the enzyme from calf spleen, *The Journal of Biological Chemistry*, Volume 267, (Issue 11), April 1992, Pages 7342-7351.
 - [12] C. Mao, W.J. Cook, et al., The crystal structure of *Escherichia coli* purine nucleoside phosphorylase: a comparison with the human enzyme reveals a conserved topology, *Structure*, Volume 5, (Issue 10), October 1997, Pages 1373-1383.
 - [13] A. Bzowska, E. Kulikowska, et al., Purine nucleoside phosphorylases: properties, functions, and clinical aspects, *Pharmacology & Therapeutics*, Volume 88, (Issue 3), December 2000, Pages 349-425.
 - [14] L.A. Basso, D.S. Santos, et al., Purine nucleoside phosphorylase from *Mycobacterium tuberculosis*. Analysis of inhibition by a transition-state analogue and dissection by parts, *Biochemistry*, Volume 40, (Issue 28), July 2001, Pages 8196-8203.
 - [15] K.F. Jensen, P. Nygaard, Purine nucleoside phosphorylase from *Escherichia coli* and *Salmonella typhimurium*. Purification and some properties, *European Journal of Biochemistry / FEBS*, Volume 51, (Issue 1), February 1975, Pages 253-265.
 - [16] K.F. Jensen, Two purine nucleoside phosphorylases in *Bacillus subtilis*. Purification and some properties of the adenosine-specific phosphorylase, *Biochimica et Biophysica Acta*, Volume 525, (Issue 2), August 1978, Pages 346-356.
 - [17] R.G. Ducati, D.S. Santos, et al., Substrate specificity and kinetic mechanism of purine nucleoside phosphorylase from *Mycobacterium tuberculosis*, *Archives of Biochemistry and Biophysics*, Volume 486, (Issue 2), June 2009, Pages 155-164.
 - [18] T.P. Zimmerman, N.B. Gersten, et al., Adenine as substrate for purine nucleoside phosphorylase, *Canadian Journal of Biochemistry*, Volume 49, (Issue 9), September 1971, Pages 1050-1054.
 - [19] J.D. Stoeckler, A.F. Poirot, et al., Purine nucleoside phosphorylase. 3. Reversal of purine base specificity by site-directed mutagenesis, *Biochemistry*, Volume 36, (Issue 39), September 1997, Pages 11749-11756.
 - [20] A. Bzowska, E. Kulikowska, et al., Properties of purine nucleoside phosphorylase (PNP) of mammalian and bacterial origin, *Zeitschrift für Naturforschung. C*, Volume 45, (Issue 1-2), January-February 1990, Pages 59-70.
 - [21] K.F. Jensen, Purine-nucleoside phosphorylase from *Salmonella typhimurium* and *Escherichia coli*. Initial velocity kinetics, ligand binding, and reaction mechanism, *European Journal of Biochemistry / FEBS*, Volume 61, (Issue 2), January 1976, Pages 377-386.
 - [22] J. Tebbe, A. Bzowska, et al., Crystal structure of the purine nucleoside phosphorylase (PNP) from *Cellulomonas sp.* and its implication for the mechanism of trimeric PNPs, *Journal of Molecular Biology*, Volume 294, (Issue 5), December 1999, Pages 1239-1255.
 - [23] T.H. Tahirov, E. Inagaki, et al., Crystal structure of purine nucleoside phosphorylase from *Thermus thermophilus*, *Journal of Molecular Biology*, Volume 337, (Issue 5), April 2004, Pages 1149-1160.
 - [24] W. Shi, L.A. Basso, et al., Structures of purine nucleoside phosphorylase from *Mycobacterium tuberculosis* in complexes with immucillin-H and its pieces, *Biochemistry*, Volume 40, (Issue 28), July 2001, Pages 8204-8215.
 - [25] R.G. Ducati, L.A. Basso, et al., Crystallographic and docking studies of purine nucleoside phosphorylase from *Mycobacterium tuberculosis*, *Bioorganic & Medicinal Chemistry*, Volume 18, (Issue 13), July 2010, Pages 4769-4774.
 - [26] W.B. Parker, M.C. Long, Purine metabolism in *Mycobacterium tuberculosis* as a target for drug development, *Current Pharmaceutical Design*, Volume 13, (Issue 6), 2007, Pages 599-608.
 - [27] E.A. Taylor Ringia, P.C. Tyler, et al., Transition state analogue discrimination by related purine nucleoside phosphorylases, *Journal of the American Chemical Society*, Volume 128, (Issue 22), June 2006, Pages 7126-7127.
 - [28] A. Lewandowicz, W. Shi, et al., Over-the-barrier transition state analogues and crystal structure with *Mycobacterium tuberculosis* purine nucleoside phosphorylase, *Biochemistry*, Volume 42, (Issue 20), May 2003, Pages 6057-6066.
 - [29] L.F. Timmers, R.A. Caceres, et al., Structural studies of human purine nucleoside phosphorylase: towards a new specific empirical scoring function, *Archives of Biochemistry and Biophysics*, Volume 479, (Issue 1), November 2008, Pages 28-38.
 - [30] R.A. Caceres, L.F. Timmers, et al., Crystal structure and molecular dynamics studies of human purine nucleoside phosphorylase complexed with 7-deazaguanine, *Journal of Structural Biology*, Volume 169, (Issue 3), March 2010, Pages 379-388.
 - [31] W.F. de Azevedo Jr., F. Canduri, et al., Crystal structure of human purine nucleoside phosphorylase at 2.3Å resolution, *Biochemical and Biophysical Research Communications*, Volume 308, (Issue 3), August 2003, Pages 545-552.
 - [32] W. Filgueira de Azevedo Jr., F. Canduri, et al., Structural basis for inhibition of human PNP by immucillin-H, *Biochemical and Biophysical Research Communications*, Volume 309, (Issue 4), October 2003, Pages 917-922.
 - [33] W. Filgueira de Azevedo Jr., G.C. dos Santos, et al., Docking and small angle X-ray scattering studies of purine nucleoside phosphorylase, *Biophysical Research Communications*, Volume 309, (Issue 4), October 2003, Pages 923-928.
 - [34] W.F. de Azevedo Jr., F. Canduri, et al., Crystal structure of human PNP complexed with guanine, *Biophysical Research Communications*, Volume 312, (Issue 3), December 2003, Pages 767-772.
 - [35] F. Canduri, D.M. dos Santos, et al., Structures of human purine nucleoside phosphorylase complexed with inosine and ddi, *Biophysical Research Communications*, Volume 313, (Issue 4), January 2004, Pages 907-914.
 - [36] F. Canduri, V. Fadel, et al., Crystal structure of human PNP complexed with hypoxanthine and sulfate ion, *Biophysical Research Communications*, Volume 326, (Issue 2), January 2005, Pages 335-338.
 - [37] F. Canduri, V. Fadel, et al., New catalytic mechanism for human purine nucleoside phosphorylase, *Biophysical Research Communications*, Volume 327, (Issue 3), February 2005, Pages 646-649.
 - [38] D.M. dos Santos, F. Canduri, et al., Crystal structure of human purine nucleoside phosphorylase complexed with acyclovir.

- Biophysical Research Communications*, Volume 308, (Issue 3), August 2003, Pages 553-559.
- [39] R.G. Silva, J.H. Pereira, et al., Kinetics and crystal structure of human purine nucleoside phosphorylase in complex with 7-methyl-6-thio-guanosine, *Archives of Biochemistry and Biophysics*, Volume 442, (Issue 1), October 2005, Pages 49-58.
- [40] N. Guex, M.C. Peitsch, SWISS-MODEL and the Swiss-PdbViewer: an environment for comparative protein modeling, *Electrophoresis*, Volume 18, (Issue 15), December 1997, Pages 2714-2723.
- [41] F.B. Zanchi, R.A. Caceres, et al., Molecular dynamics studies of a hexameric purine nucleoside phosphorylase, *Journal of Molecular Modeling*, Volume 16, (Issue 3), March 2010, Pages 543-550.
- [42] S. Bantia, J.A. Montgomery, et al., *In vivo* and *in vitro* pharmacologic activity of the purine nucleoside phosphorylase inhibitor BCX-34: the role of GTP and dGTP, *Immunopharmacology*, Volume 35, (Issue 1), October 1996, Pages 53-63.
- [43] P.C. Kline, V.L. Schramm, Purine nucleoside phosphorylase. Inosine hydrolysis, tight binding of the hypoxanthine intermediate, and third-the-sites reactivity, *Biochemistry*, Volume 31, (Issue 26), July 1992, Pages 5964-5973.
- [44] S. Banti, P.J. Miller, et al., Comparison of *in vivo* efficacy of BCX-1777 and cyclosporin in xenogeneic graft-vs.-host disease: the role of dGTP in antiproliferative action of BCX-1777, *International Immunopharmacology*, Volume 2, (Issue 7), June 2002, Pages 913-923.
- [45] R.W. Miles, P.C. Tyler, et al., One-third-the-sites transition-state inhibitors for purine nucleoside phosphorylase, *Biochemistry*, Volume 37, (Issue 24), June 1998, Pages 8615-8621.
- [46] G.B. Evans, R.H. Furneaux, et al., Synthesis of second-generation transition state analogues of human purine nucleoside phosphorylase, *Journal of Medicinal Chemistry*, Volume 46, (Issue 24), November 2003, Pages 5271-5276.
- [47] V.P. Kamath, J.J. Juarez-Brambila, et al., Development of a Practical Synthesis of a Purine Nucleoside Phosphorylase Inhibitor: BCX-4208, *Organic Process Research & Development*, Volume 13, (Issue 5), July 2009, Pages 928-932.
- [48] T. Semeraro, A. Lossani, et al., Simplified analogues of immucillin-G retain potent human purine nucleoside phosphorylase inhibitory activity, *Journal of Medicinal Chemistry*, Volume 49, (Issue 20), October 2006, Pages 6037-6045.
- [49] K. Clinch, G.B. Evans, et al., Third-generation immucillins: syntheses and bioactivities of acyclic immucillin inhibitors of human purine nucleoside phosphorylase, *Journal of Medicinal Chemistry*, Volume 52, (Issue 4), February 2009, Pages 1126-1143.
- [50] M.C. Ho, W. Shi, et al., Four generations of transition-state analogues for human purine nucleoside phosphorylase *Proceedings of the National Academy of Sciences of the United States of America*, Volume 107, (Issue 11), March 2010, Pages 4805-4812.
- [51] A.A. Edwards, J.M. Mason, et al., Altered enthalpy-entropy compensation in picomolar transition state analogues of human purine nucleoside phosphorylase, *Biochemistry*, Volume 48, (Issue 23), June 2009, Pages 5226-5238.
- [52] E.A. Taylor Ringia, V.L. Schramm, Transition states and inhibitors of the purine nucleoside phosphorylase family, *Current Topics in Medicinal Chemistry*, Volume 5, (Issue 13), 2005, Pages 1237-1258.

Authors' information

¹Centro de Pesquisas em Biologia Molecular e Funcional (CPBMF), Instituto Nacional de Ciência e Tecnologia em Tuberculose (INCT-TB), Pontifícia Universidade Católica do Rio Grande do Sul (PUCRS), Porto Alegre, RS, Brazil.

²Faculdade de Biociências, Instituto Nacional de Ciência e Tecnologia em Tuberculose (INCT-TB), Laboratório de Bioquímica Estrutural,

Pontifícia Universidade Católica do Rio Grande do Sul (PUCRS), Porto Alegre, RS, Brazil.

³Corresponding authors: Postal address: Centro de Pesquisas em Biologia Molecular e Funcional (CPBMF), Instituto Nacional de Ciência e Tecnologia em Tuberculose (INCT-TB), Pontifícia Universidade Católica do Rio Grande do Sul (PUCRS), Avenida Ipiranga 6681/92-A, 90619-900, Porto Alegre, RS, Brazil. Phone/Fax: +55-51-33203629. E-mail addresses: diogenes@pucrs.br (Diógenes S. Santos) or luiz.basso@pucrs.br (Luiz A. Basso).



Dr. **Diógenes S. Santos** was born in Gandu (Bahia State) in Brazil on June 28th, 1942. Dr. Santos did BSc in Veterinary Medicine at Federal University of Bahia (1968) in Brazil, MSc in Microbiology and Immunology at Federal University of São Paulo (1972), PhD awarded by Federal University of São Paulo (1975) for his experimental work at Medical Center of New York University (under Dr. Werner K. Maas supervision) in USA, and post-doc at Oxford University in England (1993-1995). Dr. Santos was adjunct professor at Federal University from 1975 to 2003, and he is since full professor at Pontifical Catholic University of Rio Grande do Sul. The major field of study of Dr. Santos is the rational-drug design (function- and structure-based) of chemotherapeutic agents to treat tuberculosis and T-cell mediated diseases.

He has published over 129 papers in important international scientific journals (for instance, EMBO Journal, Cell, Molecular Microbiology, Journal of Cellular Biochemistry, Infection and Immunity, Journal of Cellular Biochemistry, Infection and Immunity, Journal of Bacteriology, ABB, BBRC, Proteins, Biophysical Journal, Chemical Communications, Current Pharmaceutical Design, Bioorganic & Medicinal Chemistry, Journal of Structural Biology, Current Pharmaceutical Biotechnology, Current Drug Targets, Cell Biochemistry and Biophysics, Microbial Cell Factories, Acta Crystallographica, Journal of Inorganic Biochemistry, Tetrahedron Letters, Organic Letters, Protein Expression and Purification, Journal of Clinical Microbiology, MIOC, FEMS Microbiology Letters, Medicinal Chemistry Reviews, Avian Diseases). He has also published 9 book chapters and deposited over 31 structural coordinates on the Protein Data Bank (www.rcsb.org). He acted as mentor of 36 MSc dissertations and 8 PhD theses. Dr. Santos has filed for 4 patents in Brazil and 2 abroad (Patent Convention Treaty – PCT).

Dr. Santos was the founder, and director for ten years, of Biotechnology Center of Federal University of Rio Grande do Sul, and acted as consultant for BID, FAO and WHO. As co-ordinator of a program for graduate training of young Brazilian scientists, Dr. Santos has masterminded the graduation of over 40 (forty) students abroad (from Japan, Europe, to California in USA). Dr. Santos is the Chief Executive Officer of “Quatro G Research & Development”, a biotechnology-based private company. Dr. Santos is currently the head of the National Institute of Science and Technology on Tuberculosis of the Ministry of Health and Ministry of Science and Technology of Brazil.

Adsorption of Rhodamine B Dye – Thermodynamic and Equilibrium Studies

K. Baskaran¹, B. R. Venkatraman², S. Arivoli*³

Abstract – *Calotropis gigantea* bark carbon, a waste from the agricultural field, was investigated as a replacement for the current expensive methods of removing rhodamine B from aqueous solutions. *Calotropis gigantea* bark was collected from agricultural fields in and around Pudukkottai. It was carbonized and activated and sieved to the desired particle size. The 50 ml conical flasks containing solution and *Calotropis gigantea* bark carbon were shaken at room temperature (30±2°C). The pH of values of solution was adjusted by addition of HNO₃ and NaOH. The batch study indicated that initial pH of aqueous solution considerably affects the dye removal. While the removal efficiency decreased with increasing initial concentration, it increased with increasing adsorbent concentration. The linear forms of the Langmuir and Freundlich models result indicated that the Langmuir adsorption isotherm fitted the data better than the Freundlich adsorption isotherm. Adsorption of the dye onto *Calotropis gigantea* bark carbon was favorable sorption. Therefore, *Calotropis gigantea* bark carbon, the low-cost is suitable for use as adsorbent for rhodamine B under this investigation. **Copyright** © 2010 Praise Worthy Prize S.r.l. - All rights reserved.

Keywords: Activated Carbon (CGC), Rhodamine B, Adsorption Isotherm, Adsorption Kinetics, Thermodynamic Parameters, Intra-Particle Diffusion and Regeneration Pattern

I. Introduction

The discharge of highly coloured effluents into natural water bodies is not only anesthetically displeasing, but it also impedes light penetration, thus upsetting biological processes within a stream. In addition, many dyes are toxic to some organisms causing direct destruction of aquatic communities. Some dyes can cause allergic dermatitis, skin irritation, cancer and mutation in man. Recent estimates indicate that, approximately, 12% of synthetic textile dyes used each year is lost during manufacture and processing operation and 20% of these dyes enter the environment through effluents that result from the treatment of residual industrial waters.

Wastewaters from dyeing industries released in to nearby land or rivers without any treatment because the conventional treatment methods are not cost effective in the Indian context.

Adsorption is one of the most effective methods and activated carbon is the preferred adsorbent widely employed to treat wastewater containing different classes of dyes recognizing the economic drawback of commercial activated carbon.

Many investigators [1] - [3] have studied the feasibility of using inexpensive alternative materials like pearl millet husk, date pits, saw dust buffing dust of leather industry, coir pith, crude oil residue, tropical grass, olive stone and almond shells, pine bark, wool waste, coconut shell etc., as carbonaceous precursors for the removal of dyes from water and wastewater.

The present study undertaken to evaluate the efficiency of a carbon adsorbent prepared from acid activated *Calotropis gigantea* bark carbon for removal of dye in aqueous solution. In order to design adsorption treatment systems, knowledge of kinetic and mass transfer processes is essential. In this paper, the applicability of kinetic and mass-transfer models for the adsorption of Rhodamine B onto acid activated carbon is reported.

II. Experimental Procedure

II.1. Materials

II.1.1. Adsorbent Materials

The dried *Calotropis gigantea* bark was carbonized with concentrated sulphuric acid in the weight ratio of 1:1 (w/v). The resulting carbon was washed with distilled water until a constant pH of the slurry was reached. Then the carbon was dried for four hours at 100°C in a hot air oven. Heating for twelve hours in a furnace at 500°C has completed the carbonization and activation. The dried material was ground well to a fine powder and sieved.

II.2. Adsorption Dynamic Experiments

II.2.1. Batch Equilibration Method

The adsorption experiments were carried out in a batch process at 30, 40, 50 and 60° C temperatures. The

known weight of adsorbent material was added to 50 ml of the dye solutions with an initial concentration of 10 mg/L to 50 mg/L. The contents were shaken thoroughly using a mechanical shaker rotating with a speed of 120 rpm. The solution was then filtered at preset time intervals and the residual dye concentration was measured.

II.2.2. Effect of Variable Parameters

II.2.2.1. Dosage of Adsorbents

The various doses of the adsorbents are mixed with the dye solutions and the mixture was agitated in a mechanical shaker. The adsorption capacities for different doses were determined at definite time intervals by keeping all other factors constant.

II.2.2.2. Initial Concentration of Dye

In order to determine the rate of adsorption, experiments were conducted with different initial concentrations of dyes ranging from 10 to 50 mg/L. All other factors have kept constant.

II.2.2.3. Contact Time

The effect of period of contact on the removal of the dye on adsorbent in a single cycle was determined by keeping particle size, initial concentration, dosage, pH and concentration of other ions constant.

II.2.2.4. p^H

Adsorption experiments were carried out at pH 3,4,5,6,7,8,9 and 10. The acidic and alkaline pH of the media was maintained by adding the required amounts of dilute hydrochloric acid and sodium hydroxide solutions. The parameters like particle size of the adsorbents, dye concentration, dosage of the adsorbent and concentration of other ions have kept constant while carrying out the experiments. The pH of the samples was determined using a portable pH meter, Systronics make. The pH meter was calibrated with 4.0 and 9.2 buffers.

II.2.2.5. Chloride

The experiments were done in the presence of varying chloride environments using various sodium chloride solutions. While doing the experiments, the absence of other anions has ensured.

II.2.2.6. Temperature

The adsorption experiments were performed at four different temperatures viz., 30, 40, 50 and 60°C in a thermostat attached with a shaker, Remi make. The constancy of the temperature was maintained with an accuracy of $\pm 0.5^\circ\text{C}$.

II.2.2.7. Zero point charge

The pH at the potential of zero charge of the carbon (pH_{zpc}) was measured using the pH drift method [4]. The pH of the solution was adjusted by using 0.01 M sodium hydroxide or hydrochloric acid. Nitrogen was bubbled through the solution at 25°C to remove the dissolved carbon dioxide. 50 mg of the activated carbon was added to 50 ml of the solution. After stabilization, the final pH was recorded. The graphs of final pH versus initial pH used to determine the zero point charge of the activated carbon.

II.2.2.8. Desorption Studies

Desorption studies help to elucidate the nature of adsorption and recycling of the spent adsorbent and the dye. The effect of various reagents used for desorption are studied.

III. Results and Discussion

III.1. Characterization of the Adsorbent

Activated carbons are a widely used adsorbent due to its high adsorption capacity, high surface area, micro porous structure and high degree of surface respectively. The wide usefulness of carbon is a result of their specific surface area, high chemical and mechanical stability. The chemical nature and pore structure usually determines the sorption activity. The physico chemical properties are listed in Table I.

TABLE I
CHARACTERISTICS OF THE ADSORBENT

Properties	CGC
Particle size (mm)	0.048
Density (g/cc)	0.2876
Moisture content (%)	2.50
Loss on ignition (%)	89
Acid insoluble matter (%)	1.75
Water soluble matter (%)	0.73
pH of aqueous solution	6.5
pH_{zpc}	6.1

III.2. Effect of Carbon Concentration

The adsorption of the dyes on carbon was studied by varying the carbon concentration (25-250 mg/50mL) for 30 mg/L of dye concentration. The percent adsorption increased with increase in the carbon concentration (Figure 1). This was attributed to increased carbon surface area and availability of more adsorption sites [5], [6]. Hence the remaining parts of the experiments are carried out with the adsorbent dose of 50mg/50 mL.

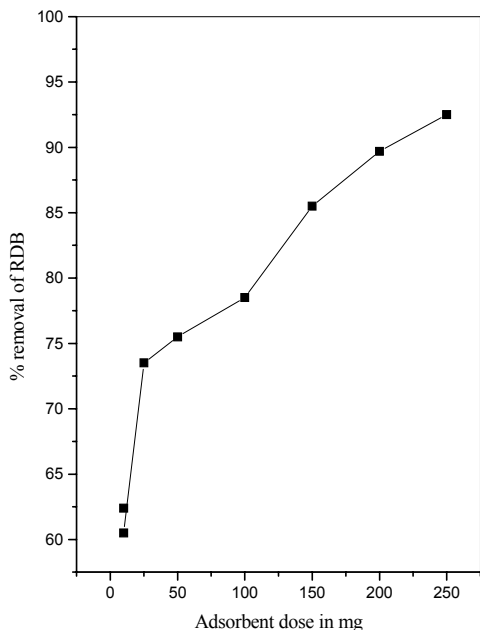


Fig. 1. Effect of adsorbent dose on the removal of RDB dye [RDB]=30 mg/L; Contact time=60 min; Temp=30°C

III.2.1. Effect of Contact Time and Initial Dye Concentration

The experimental results of adsorptions of at various concentrations (10, 20, 30, 40 and 50 mg/L) with contact time are shown in representative Figure 2.

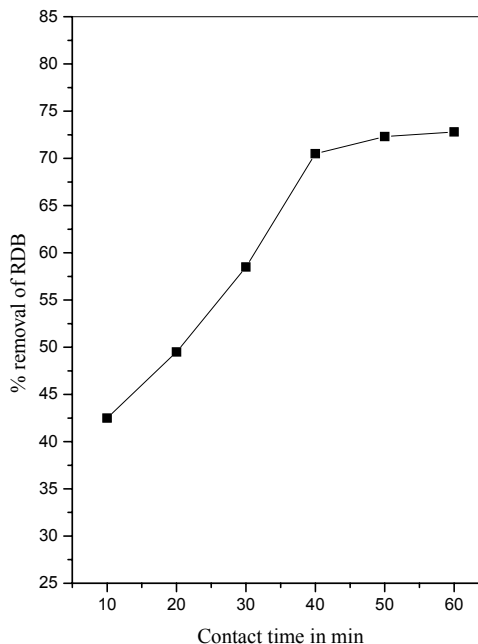


Fig. 2. Effect of contact time on the removal of RDB dye [RDB]=30 mg/L; Adsorbent dose=25 mg/50ml; Temp=30°C

TABLE II
EQUILIBRIUM PARAMETERS FOR THE ADSORPTION OF DYE ONTO ACTIVATED CARBON

[RDB] ₀	C _e (mg/L)				Q _e (mg/g)				Dye removed (%)			
	30°	40°	50°	60°	30°	40°	50°	60°	30°	40°	50°	60°
10	1.6415	1.3402	1.1505	1.0015	16.717	17.3196	17.699	17.9970	83.58	86.59	88.49	89.98
20	4.1545	3.9162	3.7092	3.5156	31.691	32.1676	32.5816	32.9688	79.22	80.41	81.45	82.42
30	8.0415	7.8012	7.6015	7.4012	43.917	44.3976	44.797	45.1976	73.19	73.99	74.66	75.32
40	14.1814	13.6146	13.1177	12.6185	51.6372	52.7708	53.7646	54.7630	64.54	65.96	67.20	68.45
50	23.6056	22.7165	21.8189	20.9950	52.7888	54.5670	56.3622	58.0100	52.78	54.56	56.36	58.01

It means that the adsorption is highly dependent on initial concentration of dye. It is because of that at lower concentration, the ratio of the initial number of dye molecules to the available surface area is low subsequently the fractional adsorption becomes independent of initial concentration. However, at high concentration the available sites of adsorption becomes fewer and hence the percentage removal of dye is dependent upon initial concentration [5], [6]. Equilibrium have established at 40 minutes for all concentrations. Figure 2 reveals that the curves are single, smooth, and continuous, leading to saturation, suggesting the possible monolayer coverage of the dyes on the carbon surface.

III.2.2. Adsorption Isotherm

The experimental data analyzed according to the linear form of the Langmuir and Freundlich isotherms [7], [8]. The Langmuir isotherm represented by the following equation:

$$C_e/Q_e = 1/Q_m b + C_e/Q_m \tag{1}$$

where, C_e is the equilibrium concentration (mg/L), Q_e is the amount adsorbed at equilibrium (mg /g) and Q_m and b is Langmuir constants related to adsorption efficiency and energy of adsorption, respectively. The linear plots of C_e/Q_e versus C_e suggest the applicability of the Langmuir isotherms (Figure 3). The values of Q_m and b were determined from slope and intercepts of the plots and are presented in Table III.

TABLE III
LANGMUIR ISOTHERM RESULTS

Dye	Temp °C	Statistical parameters/constants		
		r ²	Q _m	b
RDB	30	0.9972	62.89	0.2525
	40	0.9936	64.10	0.2816
	50	0.9961	65.36	0.2985
	60	0.9967	67.11	0.3125

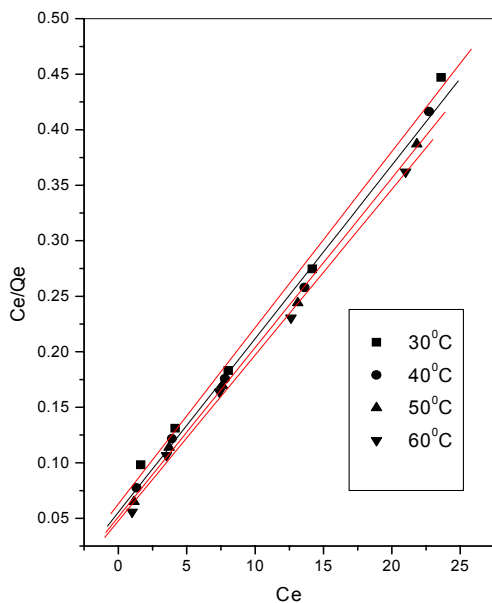


Fig. 3. Linear Langmuir adsorption isotherm for the removal of RDB

From the results, it is clear that the value of adsorption efficiency Q_m and adsorption energy b of the carbon increases on increasing the temperature. From the values we can conclude that the maximum adsorption corresponds to a saturated monolayer of adsorbate molecules on adsorbent surface with constant energy and no transmission of adsorbate in the plane of the adsorbent surface. The observed b values shows that the adsorbent prefers to bind acidic ions and that speciation predominates on sorbent characteristics, when ion exchange is the predominant mechanism takes place in the adsorption of RDB, it confirms the endothermic nature of the process involved in the system [9] - [11]. To confirm the favourability of the adsorption process, the separation factor (R_L) was calculated and presented in Table IV. The values were found to be between 0 and 1 and confirm that the ongoing adsorption process is favorable [12].

The Freundlich equation was employed for the adsorption of Rhodamine B dye on the adsorbent. The Freundlich isotherm was represented by:

$$\log Q_e = \log K_f + 1/n \log C_e \quad (2)$$

where, Q_e is the amount of Rhodamine B dye adsorbed (mg/g), C_e is the equilibrium concentration of dye in solution (mg/L) and K_f and n are constants incorporating the factors affecting the adsorption capacity and intensity of adsorption, respectively.

TABLE IV
DIMENSIONLESS SEPARATION FACTOR (R_L)

[RDB] ₀ (mg/L)	30°C	40°C	50°C	60°C
10	0.284	0.262	0.251	0.242
20	0.165	0.151	0.142	0.137
30	0.116	0.106	0.100	0.096
40	0.090	0.081	0.077	0.074
50	0.073	0.066	0.062	0.060

Linear plots of log Q_e versus log C_e shows that the adsorption of Rhodamine B dye obeys the Freundlich adsorption isotherm (Figure 4).

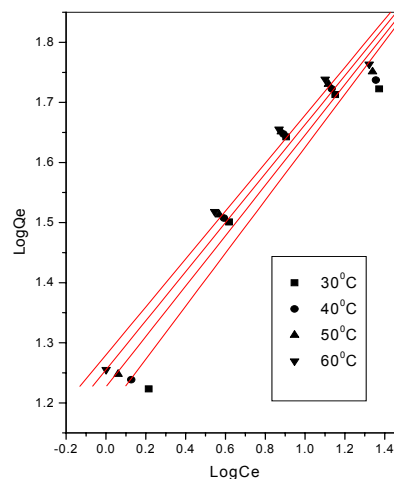


Fig. 4. Linear Freundlich adsorption isotherm for the adsorption of RDB

The values of K_f and n given in the Table V shows that the increase in negative charges on the adsorbent surface that makes electrostatic force like Vanderwaal's between the carbon surface and dye ion. The molecular weight, size and radii either limit or increase the possibility of the adsorption of the dye onto adsorbent. However, the values clearly show the dominance in adsorption capacity. The intensity of adsorption is an indicative of the bond energies between dye and adsorbent and the possibility of slight chemisorptions rather than physisorption [11]. However, the multilayer adsorption of RDB through the percolation process may be possible. The values of n are greater than one indicating the adsorption is much more favorable [12].

TABLE V
FREUNDLICH ISOTHERM RESULTS

Dye	Temp	Statistical parameters/constants		
		r ²	K _f	n
RDB	30	0.9968	3.2693	2.2691
	40	0.9959	3.4099	2.3860
	50	0.9928	3.5085	2.4527
	60	0.9906	3.5966	2.5087

III.2.3. Effect of Temperature

The adsorption capacity of the carbon increased with increase in the temperature of the system from 30°-60°C. Thermodynamic parameters such as change in free energy were determined using the following equations (ΔG°) (J/mol), enthalpy (ΔH°) (kJ/mol) and entropy (ΔS°) (J/K/mol) were determined using the following equations:

$$K_0 = C_{solid}/C_{liquid} \tag{3}$$

$$\Delta G^\circ = -RT \ln K_0 \tag{4}$$

$$\log K_0 = \Delta S^\circ / (2.303RT) - \Delta H^\circ / (2.303RT) \tag{5}$$

where, K₀ is the equilibrium constant, C_{solid} is the solid phase concentration at equilibrium (mg/ L), C_{liquid} is the

liquid phase concentration at equilibrium (mg/L), T is the temperature in Kelvin and R is the gas constant. The ΔH° and ΔS° values obtained from the slope and intercept of Van't Hoff plots have presented in Table 6. The values ΔH° is within the range of 1 to 93 KJ/mol indicates the physisorption. The results points out that physisorption are much more favorable for the adsorption of RDB. The positive values of ΔH° show the endothermic nature of adsorption and it governs the possibility of physical adsorption [12]. Because in the case of physical adsorption, while increasing the temperature of the system, the extent of dye adsorption increases, this rules out the possibility of chemisorption [12]. The low ΔH° value depicts dye is physisorbed onto adsorbent.

The negative values of ΔG° (Table VI) shows the adsorption is highly favorable and spontaneous. The positive values of ΔS° (Table VI) shows the increased disorder and randomness at the solid solution interface of RDB with CGC adsorbent, while the adsorption there are some structural changes in the dye and the adsorbent occur. The adsorbed water molecules, which have displaced by the adsorbate species, gain more translational entropy than is lost by the adsorbate molecules, thus allowing the prevalence of randomness in the system. The enhancement of adsorption capacity of the activated carbon at higher temperatures was attributed to the enlargement of pore size and activation of the adsorbent surface [11].

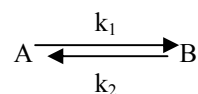
TABLE VI
EQUILIBRIUM CONSTANT AND THERMODYNAMIC PARAMETERS FOR THE ADSORPTION OF DYE ONTO CARBON

[D] ₀	K ₀				ΔG°				ΔH°	ΔS°
	Temperature (°C)									
	30	40	50	60	30	40	50	60		
10	5.091	6.461	7.691	8.985	-4100.33	-4855.53	-5478.70	-6078.54	-15.78	65.77
20	3.814	4.106	4.391	4.688	-3372.36	-3676.22	-3973.85	-4277.99	-5.76	30.14
30	2.730	2.845	2.946	3.053	-2530.58	-2721.36	-2902.00	-3090.42	-3.10	18.60
40	1.820	1.938	2.049	2.169	-1509.38	-1721.85	-1926.81	-2144.81	-4.88	21.10
50	1.118	1.201	1.291	1.381	-281.30	-476.71	-687.13	-894.75	-5.93	20.49

III.2.4. Kinetics of Adsorption

The kinetics of sorption describes the solute uptake rate, which in turn governs residence time or sorption reaction. It is one of the important characteristics in defining the efficiency or sorption. In the present study, the kinetics of the dye removal was carried out to understand the behaviour of these low cost carbon adsorbents. The adsorption of dye from an aqueous follows reversible first order kinetics, when a single

species are considered on a heterogeneous surface. The heterogeneous equilibrium between the dye solutions and the activated carbon are expressed as:



where, k₁ is the forward rate constant and k₂ is the backward rate constant. A represents dyes remaining in

the aqueous solution and B represent dye adsorbed on the surface of activated carbon. The equilibrium constant (K_0) is the ratio of the concentration adsorbate in adsorbent and in aqueous solution ($K_0=k_1/k_2$).

In order to study the kinetics of the adsorption process under consideration the following kinetic equation proposed by Natarajan and Khalaf as cited in literature [1] has been employed:

$$\log C_0/C_t=(K_{ad}/2.303)t \quad (6)$$

where, C_0 and C_t are the concentration of the dye in (in mg/L) at time zero and at time t, respectively. The rate constants (K_{ad}) for the adsorption processes have been calculated from the slope of the linear plots of $\log C_0/C_t$ versus t for different concentrations and temperatures. The determination of rate constants as described in literature given by:

$$K_{ad}=k_1+k_2=k_1+(k_1/K_0)=k_1[1+1/K_0] \quad (7)$$

The overall rate constant k_{ad} for the adsorption of dye at different temperatures are calculated from the slopes of the linear Natarajan-Khalaf plots. The rate constant values are collected in Table VII shows that the rate constant (k_{ad}) increases with increase in temperature suggesting that the adsorption process is endothermic in nature. Further, k_{ad} values decrease with increase in initial concentration of the dye. In cases of strict surface adsorption a variation of rate should be proportional to the first power of concentration. However, when pore diffusion limits the adsorption process, the relationship between initial dye concentration and rate of reaction will not be linear. Thus, in the present study pore diffusion limits the overall rate of dye adsorption. The overall rate of adsorption is separated into the rate of forward and reverse reactions using the above equation. The rate constants for the forward and reverse processes are also collected in Table VII indicate that, at all initial concentrations and temperatures, the forward rate constant is much higher than the reverse rate constant suggesting that the rate of adsorption is clearly dominant [11], [13].

TABLE VII
RATE CONSTANTS FOR THE ADSORPTION OF RDB DYE (K_{ad} , MIN^{-1}) AND THE CONSTANTS FOR FORWARD (K_1 , MIN^{-1}) AND REVERSE (K_2 , MIN^{-1}) PROCESS

[D] ₀	Temperature (°C)											
	k_{ad}				30		40		50		60	
	30	40	50	60	k_1	k_2	k_1	k_2	k_1	k_2	k_1	k_2
10	0.02199	0.01827	0.01476	0.01178	0.01838	0.00361	0.01447	0.00379	0.01080	0.00395	0.00760	0.0041
20	0.02512	0.01909	0.01316	0.01101	0.02176	0.00336	0.01535	0.00373	0.00974	0.00342	0.00726	0.0037
30	0.02444	0.02020	0.01554	0.01254	0.02163	0.00281	0.01645	0.00374	0.01160	0.00393	0.00843	0.0041
40	0.03097	0.02333	0.01594	0.01264	0.02787	0.00310	0.01923	0.00410	0.01201	0.00393	0.00865	0.0039
50	0.03256	0.02781	0.01641	0.01279	0.02954	0.00302	0.02244	0.00537	0.01329	0.00312	0.00883	0.0040

III.2.5. Intraparticle Diffusion

The most commonly used technique for identifying the mechanism involved in the sorption process is by fitting the experimental data in an intraparticle diffusion plot. Previous studies by various researchers showed that the plot of q versus $t^{0.5}$ represents multi linearity, which characterizes the two or more steps involved in the sorption process. According to Weber and Morris, an intraparticle diffusion coefficient K_p is defined by the equation:

$$K_p = Q/t^{0.5} + C \quad (8)$$

Thus, the $K_p(\text{mg/g min}^{0.5})$ value can be obtained from the slope of the plot of $Qt(\text{mg/g})$ versus $t^{0.5}$ for Rhodamine B. It was noted that the sorption process tends to be followed by two phases. The two phases in the intraparticle diffusion plot suggest that the sorption

process proceeds by surface sorption and intraparticle diffusion [14], [15]. The initial curved portion of the plot indicates a boundary layer effect while the second linear portion is due to intraparticle or pore diffusion. The slope of the second linear portion of the plot has been defined as the intraparticle diffusion parameter $K_p(\text{mg/g min}^{0.5})$. On the other hand, the intercept of the plot reflects the boundary layer effect. The larger the intercept, the greater the contribution of the surface sorption in the rate limiting step. The calculated intraparticle diffusion coefficient K_p value was given by 0.335, 0.370, 0.408, 0.445 and 0.498 $\text{mg/g min}^{0.5}$ for initial dye concentration of 10, 20, 30, 40 and 50 mg/L at 30°C.

III.2.6. Effect of p^H

p^H is one of the most important parameters controlling the adsorption process. The effect of p^H of the solution on the adsorption of RDB ions on CGC was determined.

The result is shown in Fig. 5. The pH of the solution was controlled by the addition of HCl or NaOH. The uptake of RDB ions at pH 7 was the minimum and a maximum in uptake was obtained at pH 6.1. However, when the pH of the solution was increased (more than pH 8.0), the uptake of RDB ions was increased. It appears that a change in pH of the solution results in the formation of different ionic species, and different carbon surface charge. At pH values lower than 7.0, the RDB ions can enter into the pore structure. At a pH value higher than 7.0, the zwitterions form of RDB in water may increase the aggregation of RDB to form a bigger molecular form (dimer) and become unable to enter into the pore structure of the carbon surface. The greater aggregation of the zwitter ionic form is due to the attractive electrostatic interaction between the carboxyl and xanthane groups of the monomer.

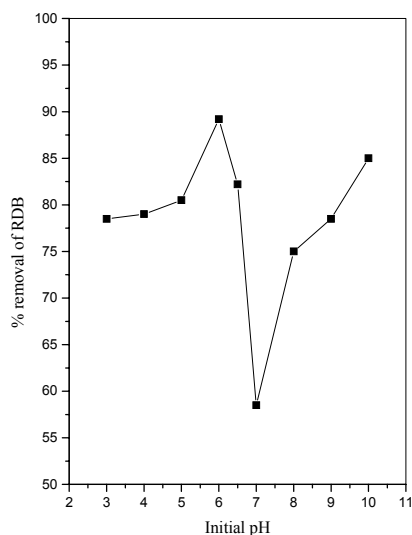


Fig. 5. Effect of pH on the removal of RDB [RDB]=30 mg/L; Contact time=60 min; Adsorbent dose=25 mg/50 mL

At a pH value higher than 8.0, the existence of OH⁻ creates a competition between $-N^+$ and COO⁻ and it will decrease the aggregation of RDB, which causes an increase in the adsorption of RDB ions on the carbon surface. The effect of the charge on the carbon surface and the electrostatic force of attraction and repulsion between the carbon surface and the RDB ions cannot explain the result [16].

III.2.7. Effect of Ionic Strength on the Adsorption of RDB

The effect of sodium chloride on the adsorption of RDB on CGC is shown in Fig. 6. In a low solution concentration NaCl had little influence on the adsorption capacity. At higher ionic strength the adsorption RDB will be increased due to the partial neutralization of the positive charge on the carbon surface and a consequent

compression of the electrical double layer by the Cl⁻ anion. The chloride ion can also enhance adsorption of RDB ion onto CGC by pairing of their charges and hence reducing the repulsion between the RDB molecules adsorbed on the surface. This initiates carbon to adsorb more of positive RDB ions [1], [16].

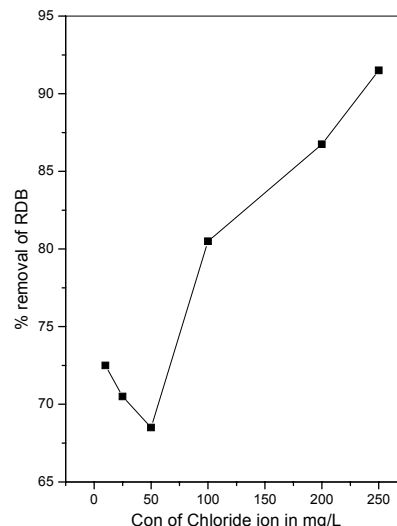


Fig. 6. Effect of Chloride ion on the removal of RDB [RDB]=30 mg/L; Adsorbent dose=25 mg/50 ml; Contact time=60 min

III.2.8. Desorption Studies

Desorption studies help to elucidate the nature of adsorption and recycling of the spent adsorbent and the dye. If the adsorbed dyes can be desorbed using neutral pH water, then the attachment of the dye of the adsorbent is by weak bonds. If sulphuric acid or alkaline water desorb the dye then the adsorption is by ion exchange. If organic acids, like acetic acid can desorb the dye, then the dye has held by the adsorbent through chemisorption. The effect of various reagents used for desorption studies indicate that hydrochloric acid is a better reagent for desorption, because we could get more than 83% removal of adsorbed dye. The reversibility of adsorbed dye in mineral acid or base is in agreement with the pH dependent results obtained. The desorption of dye by mineral acids and alkaline medium indicates that the dyes were adsorbed onto the activated carbon through by physisorption mechanisms [17], [18].

IV. Conclusion

The experimental data correlated reasonably well by the Langmuir and Freundlich adsorption isotherms and the isotherm parameters were calculated. The low as well high pH value pays the way to the optimum amount of adsorption of the dye. The objective of this paper was utilization of *Calotropis gigantea* bark carbon as adsorbent materials for the dye removal. The following

conclusions have been drawn from the above investigations:

1. The removal efficiencies of rhodamine B through adsorption onto *Calotropis gigantea* bark carbon were found to be “between” 52% to 90%.
2. The initial pH of aqueous solutions considerably affects the dye removal. On the other hand percent removal of the dye decreased with increasing initial concentration but increased with increasing adsorbent concentration.
3. The best adsorptions were obtained under the condition of 25mg/50mL dye concentration and original pH solution. The suitable contact time was 40 minutes.
4. Langmuir and Freundlich adsorption isotherm equation shows the effectiveness of the chosen adsorbent for the removal of the dye.
5. The R_L parameter shows the adsorption of rhodamine B, onto *Calotropis gigantea* bark carbon was favorable.
6. The temperature variation study showed that the rhodamine B adsorption is endothermic and spontaneous with increased randomness at the solid solution interface.
7. *Calotropis gigantea* bark carbon has the potential for use as an adsorbent for dye wastewater containing rhodamine B.

References

- [1] S.Arivoli, *Kinetic and thermodynamic studies on the adsorption of some metal ions and dyes onto low cost activated carbons*, Ph D. Thesis, Dept. of Chem. Gandhigram Rural University, Gandhigram, 2007.
- [2] G.Sekaran, K.A.Shanmugasundaram, M.Mariappan, K.V. Raghavan, *Adsorption of dyes by buffing dust of leather industry*, Indian J. Chem. Technol., Volume 2, 1995, pages 311-315.
- [3] K.Selvarani, *Studies on Low cost Adsorbents for the removal of organic and Inorganics from Water*, Ph D. Thesis, Dept. of Chem., Regional Engineering College, Tiruchirappalli, 2000.
- [4] Y.F.Jia, K.K.Thomas, *Adsorption of metal ion on nitrogen surface functional groups in activated carbon*, Langmuir, Volume 18, 2002, pages 470-478.
- [5] C.Namasivayam, R.T. Yamuna, *Adsorption of direct red by biogas residual slurry*, Environ. Pollut., Volume 89 (Issue 1), 1995, pages 1-7.
- [6] C.Namasivayam, N.Muniasamy, K.Gayathri, M.Rani, K. Renganathan, *Removal of dyes from aqueous solution by cellulosic waste orange peel*, Biores. Technol., Volume 57, 1996, pages 37-43.
- [7] I. Langmuir, *Adsorption of gases on plane surfaces of glass, mica and platinum*, J. Amer. Chem. Soc., Volume 40, 1918, pages 1361-1403.
- [8] H. Freundlich, *Adsorption in solutions*, Z. Phys. Chemie., Volume 57, 1906, pages 384-470.
- [9] D.G. Krishna, G.Bhattacharyya, *Adsorption of methylene blue on kaolinite*, Appl. Clay. Sci., Volume 20 (Issue 6), 2002, pages 295-300.
- [10] S. Arivoli, M.Viji Jain, T. Rajachandrasekar, *Cobalt adsorption on a low cost carbon-Kinetic, equilibrium and mechanistic studies*, Mat. Sci. Res. India, Volume 3, 2006, pages 241-250.
- [11] S. Arivoli, M. Hema, *Comparative study on the adsorption kinetics and thermodynamics of dyes onto acid activated low cost carbon*, Intern. J. Phys. Sci., Volume 2, 2007, pages 10-17.
- [12] S. Arivoli, B.R.Venkatraman, T. Rajachandrasekar, M. Hema, *Adsorption of ferrous ion from aqueous solution by low cost activated carbon obtained from natural plant material*, Res. J. Chem. Environ., Volume 17, 2007, pages 70-78.
- [13] G. Renmin, S. Yingzhi, C. Jian, L. Huijun, Y. Chao, *Effect of chemical modification on dye adsorption capacity of peanut hull*, Dyes and Pigments, Volume 67, 2005, pages 175-181.
- [14] V. Vadivelan, K. Vasanthkumar, *Equilibrium, kinetics, mechanism and process design for the sorption of methylene blue onto rice husk*, J. Colloid. Interf. Sci., Volume 286, 2005, pages 90-100.
- [15] W.J. Weber, *Principle and Application of Water Chemistry*, (Edited by Faust S D and Hunter J V Wiley, New York, 1967).
- [16] Yupeng Guo, Jingzhu Zhao, Hui Zhang, Shaofeng Yang, Zichen Wang, Hongding Xu, *Use of rice husk based porous carbon for the adsorption Rhodamine B from aqueous solution*, Dyes and Pigments, Volume 66, 2005, pages 123-128.
- [17] S. Arivoli, K. Kalpana, R. Sudha, T. Rajachandrasekar, *Comparative study on the adsorption kinetics and thermodynamics of metal ions onto acid activated low cost carbon*, E. J. Chem., Volume 4, 2007, pages 238-254.
- [18] M.K. Sreedhar, T.S. Anirudhan, *Mercury (II) adsorption of desorption characteristics of coconut husk based carbon- Kinetics and self diffusion*, Indian J. Environ. Protect., Volume 19, 1999, pages 8.

Poly (Methyl Methacrylate-co-Maleic Anhydride-co-N-Isopropylacrylamide): Synthesis, Characterization and Antimicrobial Activity

E. Uzluk, M. Talu

Abstract – In this study, terpolymers of methyl methacrylate (MMA), maleic anhydride (MA) and N-isopropyl acrylamide (NIPA) were synthesized with different reaction times using 1,4-dioxane as a solvent and 2,2'-Azobisisobutyronitrile (AIBN) as initiator at 65 °C. Terpolymers of different molecular weight having different reaction times were prepared. By employing various reaction times, MMA-MA-NIPA terpolymers with molecular weights ranging between 49 480 and 60 302 were obtained. The terpolymers were characterized by FTIR and UV-vis spectroscopy, viscosity measurement, solubility testing. Terpolymer composition was determined with ¹H NMR spectroscopy and elemental analysis. Thermal properties were investigated by using TGA, DTA and DSC. It was observed that glass transition temperature (T_g) of terpolymers decreased with increasing of MMA and MA contents in terpolymers. The molecular weight and polydispersity index were determined by gel permeation chromatography (GPC). These anhydride-containing polymers differ significantly from other water-soluble polymer systems because their solution process is accompanied by spontaneous hydrolysis of anhydride linkages with the formation of strong hydrogen-bonded carboxylic fragments in the side chains of the macromolecules. The terpolymers were tested for their antimicrobial properties against selected pathogen bacteria and it was observed that depending on the carboxylic, methacrylate and acrylamide content of the polymers the antimicrobial activities differ. **Copyright © 2010 Praise Worthy Prize S.r.l. - All rights reserved.**

Keywords: Antimicrobial Activity, Maleic Anhydride, Methyl Methacrylate, N-isopropyl Acrylamide, Terpolymer

I. Introduction

Maleic anhydride (MA) is a unique comonomer because it does not readily undergo homopolymerization, but forms copolymers without difficulty [1], [2]. It is also unique in that the copolymers that are formed in the presence of radical initiators are in a 1:1 ratio and in an alternating sequence [3].

The complex-radical copolymerization of maleic anhydride with various functional comonomers is an effective method for the synthesis of functional macromolecules with given compositions, structures, and properties [4].

Alternating copolymers of maleic anhydride can be regarded as preactivated polymers due to the presence of anhydride moieties susceptible to the reaction with a primary amine of a biomolecule [5]. Poly(maleic anhydride-alt-methyl vinyl ether), poly(maleic anhydride-alt-divinyl ether) and poly(citraconic anhydride-alt-divinyl ether) were used in various applications in diagnostics and in chemotherapy as effective antitumor agents [6]-[8].

Polymers in biomedical applications is one of the fastest growing areas in polymer science, where the traditional sciences are connected to the more modern engineering sciences to solve human health problems. Polymeric biomaterials are usually understood as polymeric materials and articles made from them, which are used in medicine or biotechnology. The polymers needed biomedical applications can be classified into long-term bio-stable polymers which can be used artificial organs and short-term biodegradable polymers that may be used as temporary skin, drug carrier or soluble chemotherapeutic agents [9].

In the last few years, synthetic water-soluble polymers have become of great interest in the biological field [10]-[13]. Some polymers have been investigated as biocides because of the advantages in respect to the monomeric analogues [14], [15].

Water-soluble anhydride-containing copolymers, used as polyanions and their functional derivatives have high biological and physiological activity and, in particular, antimicrobial and antitumor properties [16].

Poly(methyl methacrylate), PMMA, is the most common members of the methacrylic acid ester polymer.

Due to its good optical and mechanical properties, PMMA has been used in a wide range of fields such as biomaterials and optic fibers [17], [18]. PMMA can be used in some special applications, in solid-state pulsed dye lasers and in biomedical fields [19]-[22].

The aim of the study was to obtain new biologically active polymers using anhydride-containing monomer. In the present work, radical-initiated terpolymerization of N-isopropyl acrylamide (NIPA), methyl methacrylate (MMA) with maleic anhydride (MA) has been studied as a way to obtain new reactive amphiphilic water-soluble polymers. The characterization of polymers is determined by FTIR, UV-vis, ^1H NMR, elemental analysis, viscosity measurement, solubility testing. Thermal properties were investigated by using TGA, DTA and DSC. The effect of hydrogen bond formation NIPA units on the terpolymer composition-properties relationship has been described and discussed. Terpolymers have been characterized in their antimicrobial activity against pathogen bacteria (*Staphylococcus aureus*, *Salmonella enteritidis*, *Streptococcus faecalis*, *Escherichia coli*, *Klebsiella pneumonia*, and *Pseudomonas aeruginosa*).

II. Experimental

II.1. Materials

MMA monomer (Merck) was distilled before use. It had the following characteristics: MMA, bp 100 °C, $n_D^{20} = 1.4162$, $d_4^{20} = 0.9461$. MA monomer (Aldrich) was purified by recrystallization from anhydrous benzene and sublimation in vacuum: mp 52.8 °C. NIPA monomer (Aldrich) was purified before use by distillation under vacuum and recrystallization from diethyl ether solution: bp 91.5 °C/2 mm, mp 61.6 °C. 2,2'-Azobisisobutyronitrile (AIBN) (Acros) was recrystallized twice from methanol: mp 102.5 °C. 1,4-dioxane (Merck), methanol (Fluka), diethyl ether (Merck), and benzene (Aldrich), dimethyl sulfoxide (DMSO) (Fluka), dimethyl formamide (DMF) (Fluka) and chloroform (CHCl_3) (Merck) and CH_2Cl_2 (Merck) were used as received.

II.2. Measurements

FTIR spectra of the terpolymers (KBr pellets) were obtained using a Mattson-1000 Model spectrophotometer in the 4000-400 cm^{-1} range. ^1H NMR spectra were recorded using a Bruker Avance DPX400 (400 MHz) spectrometer with DMSO-d_6 as a solvent at 27 °C. DSC, DTA and thermogravimetric analyses (TGA) of terpolymers were performed using a Shimadzu DSC-60 calorimeter and Shimadzu TG-DTA 60/60H Thermal Analyzer, respectively, in a nitrogen atmosphere at a heating rate of 10 °C/min. The CHNS-932 Model LECO Elemental Analyzer was used for the determination of C, H and N contents in the terpolymers synthesized.

Absorption spectra were obtained using a UNICAM UV2-100 UV-visible spectrophotometer equipped with 1 cm quartz cells and 10^{-5} mol/L solutions in deionized water and DMSO in the range of 200-600 nm. GPC analyses were performed at 30 °C using THF as eluent at a flow rate of 1.0 mL/min. A refractive index detector was used as a detector. The instrument (Polymer Laboratories PL-GPC 220) was calibrated with a mixture of polystyrene standards using GPC software for the determination of the number-average molecular weight (M_n), weight-average molecular weight (M_w) and polydispersity index (PDI) of the terpolymer sample. Intrinsic viscosities of the polymers were determined in DMSO at 25 °C in 0.5 g/dL using a Ubbelohde viscometer.

The antimicrobial activities of the synthesized terpolymers were determined by the well-diffusion method [23], [24]. In this work, *Staphylococcus aureus*, *Salmonella enteritidis*, *Streptococcus faecalis* (Gram-positive) and *Escherichia coli*, *Klebsiella pneumonia*, *Pseudomonas aeruginosa* (Gram-negative) were used to assess the antibacterial activities of synthesized terpolymers. The bacterial subcultures for *Staphylococcus aureus*, *Salmonella enteritidis*, *Streptococcus faecalis*, *Escherichia coli*, *Klebsiella pneumonia* and *Pseudomonas aeruginosa* were obtained from Gazi University, Faculty of Science and Arts, Department of Biology. *Staphylococcus aureus*, *Salmonella enteritidis*, *Streptococcus faecalis*, *Escherichia coli*, *Klebsiella pneumonia* and *Pseudomonas aeruginosa* liquid cultures were prepared in brain heart infusion broth for the antimicrobial activity tests. All polymers were dissolved in deionized water at concentrations of 10 mg/mL. The solutions were filtered through a Millipore membrane filter (0.45 μm , Millipore, USA). Deionized water was found to have no antimicrobial activity against any of the organisms. Approximately 1 cm^3 of a 24 h broth culture containing 10^6 cfu/ cm^3 of bacteria was placed in sterile petri dishes. Moltent nutrient agar (15 cm^3) kept at 45 °C was then poured into the Petri dishes and allowed to solidify. Six millimeter diameter holes were then punched carefully using a sterile cork borer and completely filled with the test solutions. The plates were incubated for 24 h at 37 °C. After 24 h, the inhibition zone that appeared around the holes in each plate was measured.

II.3. Synthesis of Poly(methyl methacrylate-co-maleic anhydride-co-N-isopropylacrylamide)

The terpolymerization of MMA, MA and NIPA (N-isopropylacrylamide) using monomer feed ratio MMA:MA:NIPA= 1:2:1 was carried out in 1,4-dioxane at 65 °C for 6, 12, 24, and 36 h with AIBN radical initiator at constant total concentration of monomers under nitrogen atmosphere. Monomers, AIBN and 1,4-dioxane were added to a three-necked flask that was equipped with a stirrer, condenser and thermometer. The

flask was placed in a glycerin bath. The terpolymers produced were recovered by the addition of 10-fold excess methanol and by washing with diethyl ether and benzene. Purified terpolymers were then dried at 40 °C for 24 h under vacuum. The yields of terpolymers (6, 12, 24, and 36 h) are 63%, 75%, 83%, and 92% respectively. Terpolymer compositions were found by elemental analysis (N content for NIPA) and ^1H NMR spectroscopy using integral areas of characteristic monomer absorptions.

III. Results and Discussion

Poly(MMA-co-MA-co-NIPA) terpolymers were synthesized by radical-initiated polymerization in anhydrous medium. From the structural peculiarities of the monomers of the ternary systems under study, it may be predicted that the formation of different types of intermolecular complexes, such as the charge transfer complex (CTC) between the double bond MA (electron acceptor) and MMA (electron donor) and the hydrogen-bonded complex between MA and NIPA (electron acceptor). The synthesis and some physical properties of terpolymers are given in Table I.

TABLE I
SYNTHESIS AND SOME PHYSICAL PROPERTIES OF TERPOLYMERS

Reaction time	Yield	Color	η_{inh}
6 h	63%	Light brown	0.46 dL/g
12 h	75%	Light brown	0.57 dL/g
24 h	83%	Brown	0.60 dL/g
36 h	92%	Brown	0.73 dL/g

To obtain information about the molecular sizes of the polymers, the limit viscosity numbers (η) of the DMSO solutions of each polymer were determined and these values are given in Table I.

The polymers had intrinsic viscosities 0.46-0.73 dL/g and confirmed to be terpolymers by FTIR, UV-vis, ^1H NMR spectroscopy and elemental analysis. Light brown-to-brown films could be cast from the 1,4-dioxane solution of the resultant polymers.

A representative FTIR spectrum of terpolymer (reaction time: 6 h) is shown Fig. 1. FTIR spectra (KBr pellet, cm^{-1}): 3304 (m) and 3108 (w), broad bands for NH secondary amide; 2973 (m) and 2874 (w), CH stretching in CH, CH_2 and CH_3 groups; 1850 and 1770 (m), C=O stretching of anhydride units; 1724 (s), C=O stretching of COO^- ; 1670 (s), C=O stretching of amide I band; 1545 (m), NH amide II band; 1164 (s), C-O-C band in anhydride units; 1085 (m), NH bending in $-\text{NH}\cdots\text{O}=\text{C}$; 950-900 (s), O=C-O-C=O ring stretching vibrations of a saturated cyclic five-membered anhydride. Spectra of these terpolymers contain characteristic bands for H-bonded C=O groups and H-bonded secondary amide NH group. It can be proposed that intermolecular H-bonded fragments are most probably formed between alternating MA-NIPA diads of macromolecules in given Scheme 1 [25]. These results indicated that poly(MMA-

co-MA-co-NIPA) is successfully polymerization.

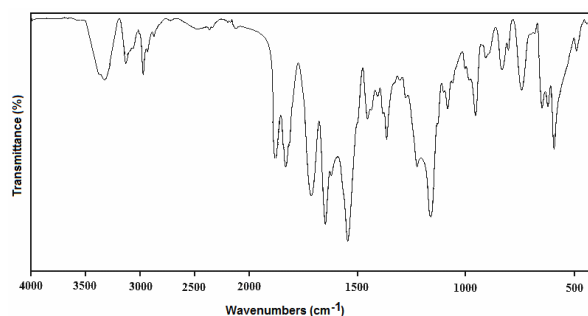
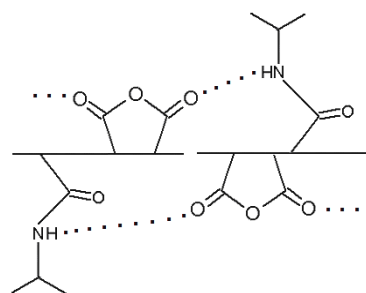


Fig. 1. FTIR spectra of poly(MMA-co-MA-co-NIPA) (reaction time: 6 h)



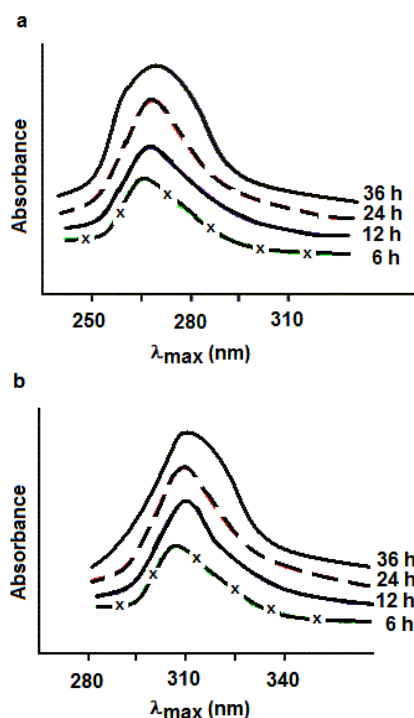
Scheme 1. Intermolecular H-bonded fragments between NIPA and MA

The elemental analyses of terpolymers are in good agreement with the calculated values for the proposed structures.

The UV-vis absorption spectrum of terpolymers in deionized water and DMSO is shown in Figs. 2. The spectrum of terpolymers exhibited typical peaks at 268 nm and 315 nm in deionized water and DMSO, respectively. The bands at 268 nm (reaction time: 6h, in deionized water) corresponded to $n \rightarrow \pi^*$ (C=O group in anhydride unit) transition.

A representative ^1H NMR spectrum of terpolymer is shown Fig. 3. ^1H NMR spectra (in DMSO-d_6 and $\text{CHCl}_3\text{-d}_1$ at 27 °C), ppm: (1) 2H, CH_2 1.40-1.80, (2) 1H, CH 1.80-2.40, (3) 1H, NH 6.95-8.10, (4) 3H, CH_3 1.95, (5) 2H, CH_2 2.40-3.20, (6) 1H, CH, 3.60, (7) 1H, CH and (8) 2H, O- CH_2 , 3.80, (9) and (10) 2H, CH 4.40 for maleic unit. The signals around δ 6.95-8.10 ppm appeared on increasing the amount of the NIPA unit in the terpolymer. Its intensity increases with an increase in ratio of the NIPA unit to other units in the terpolymer. Terpolymer compositions calculated using elemental analysis data (content of N) were in reasonable agreement with those obtained from ^1H NMR analysis [26]. Results of ^1H NMR and elemental analysis for the terpolymers are summarized in Table II.

The solubility of terpolymers was tested by 0.01 g of the polymer with 2 mL of various solvents in test tubes. All of the polymers were soluble in organic solvents, such as DMSO, DMF, and deionized water at room temperature and were insoluble in such as CH_2Cl_2 , CHCl_3 , methanol, 1,4-dioxane.



Figs. 2. UV-vis spectrum of terpolymers in deionized water (a); terpolymers in DMSO (b)

TABLE II
¹H NMR AND ELEMENTAL ANALYSIS DATA FOR DETERMINING THE COMPOSITION OF POLY(MMA-co-MA-co-NIPA) TERPOLYMERS (MONOMER FEED, MMA:MA:NIPA= 1:2:1)

Reaction time	Terpolymer composition (mol%)						
	¹ H NMR analysis			Nitrogen analysis			
	N (%)	<i>m</i> ₁	<i>m</i> ₂	<i>m</i> ₃	<i>m</i> ₁	<i>m</i> ₂	<i>m</i> ₃
6 h	3.98	27.1	45.0	27.9	27.0	45.1	27.9
12 h	4.11	25.6	47.1	27.3	25.9	47.2	26.9
24 h	4.30	23.8	48.5	27.7	24.0	48.4	27.6
36 h	4.47	21.5	49.1	29.4	22.1	48.8	29.1

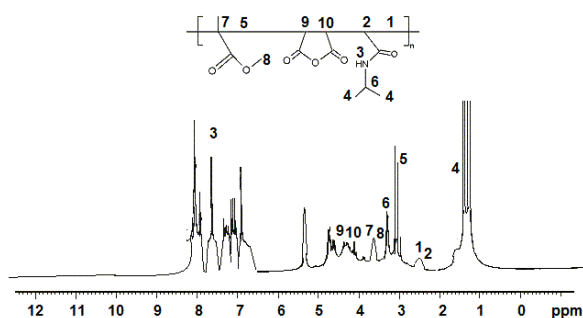


Fig. 3. ¹H NMR spectrum of poly(MMA-co-MA-co-NIPA) terpolymer (reaction time: 6 h)

The hydrophilicity of free-anhydride-containing poly(MMA-co-MA-co-NIPA) synthesized in an organic solvent significantly increases when this polymer is

dissolved in water with the formation of more hydrophilic free carboxylic groups. This exothermic process is accompanied by instantaneous hydrolysis of the anhydride units and the formation of two free carboxylic groups (-COOH) in the side chain.

Thermal properties of terpolymers were investigated by means of thermogravimetric analysis (TGA), DTA and DSC in a nitrogen atmosphere at a heating rate of 10 °C/min (Fig. 4). The obtained results are also listed in Table III.

TABLE III
 THERMAL BEHAVIORS OF TERPOLYMERS

Reaction time	DSC analysis		DTA anal.		TGA analysis			
	<i>T</i> _g (°C)	Δ <i>H</i> (mJ)	<i>T</i> _m ^a (°C)	Δ <i>H</i> (mJ)	<i>T</i> _d (°C)	<i>T</i> _i (°C)	<i>T</i> _m ^b (°C)	<i>T</i> _f (°C)
6 h	280	56.9	460	30.0	480	185	380	420
12 h	250	34.8	420	45.6	445	176	360	410
24 h	181	40.0	367	32.9	439	154	339	390
36 h	170	23.8	350	23.0	435	130	305	340

*T*_i: initial degradation temperature
*T*_m^a: melting temperature
*T*_m^b: maximum degradation temperature
*T*_f: final degradation temperature

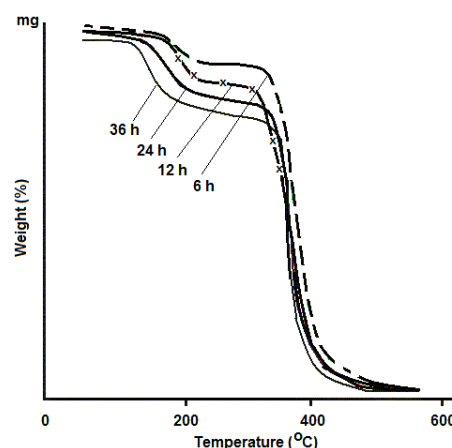


Fig. 4. TGA thermogram of poly(MMA-co-Ma-co-NIPA) terpolymers

As seen from Table III, three degradation temperatures (*T*_i, *T*_m^b, and *T*_f) of polymers were different from each other. The TGA results of terpolymers showed a two-step weight loss. In the two step degradation, the first weight loss indicates the expulsion of water molecules/moisture adsorbed in materials. Second step is due to the rupture of the polymer chain. The first weight loss for the terpolymers occurs around 130-185 °C and is the result of the loss of free water and solvent. The second weight loss is around 340-420 °C. It is found that the thermal degradation temperatures of terpolymers shifted to the lower value with increase of reaction time. TGA results confirmed that the poly(MMA-co-MA-co-NIPA) terpolymers are thermooxidatively stable up to 420 °C. As seen from Table III, maximum degradation temperature (*T*_m^b) observed at 305-380°C in terpolymers. This seems to be related to the crystalline phase that the

formed through intermolecular H bonding between the free $-C=O$ and $-NH$ groups containing terpolymers.

The polymers with molar masses have more free chain ends when compared with those with higher molar masses. This means that the free volume ratio is greater, so the T_g values of the polymers with lower molar masses are smaller [27]. Another factor affecting on the T_g value is the size and polarity of the subgroups connected to main chain. As the polarity and the number of subgroups increase, the polymer hardness also increases. The synthesized terpolymers display different thermal properties, including melting and glass-transition behaviors, depending on the content of hydrogen-bonding fragments [4].

The values of T_g , T_m^a and ΔH (enthalpy) for the terpolymers are presented in Table III. It is shown that increase of reaction time in the terpolymers decreases the value of T_g from 280 to 170 °C and the value of T_m^a from 460 to 350 °C. The polymer characteristic depends on molar mass and chain structure.

The number-average molecular weight (M_n), weight-average molecular weight (M_w) and polydispersity index (PDI) values of terpolymers are presented in Table IV. Poly(MMA-co-MA-co-NIPA) terpolymers prepared at different reaction time show a continuous increase in M_n and M_w values with increasing MMA, MA and NIPA content in terpolymer structure.

TABLE IV
MOLECULAR WEIGHT AVERAGES OF
POLY(MMA-CO-MA-CO-NIPA) TERPOLYMERS

Molecular weight averages (by GPC)			
Reaction time	M_n	M_w (g/mol)	PDI
6 h	31 150	49 480	1.60
12 h	33 250	48 875	1.50
24 h	39 480	56 062	1.42
36 h	45 340	60 302	1.33

Intrinsic viscosity of the terpolymers produced at different reaction times were determined in DMSO at 25 ± 0.1 °C in the concentration range 0.1-1.0 g/dL using a Ubbelohde viscometer. $[\eta]$: 0.46 (reactime time: 6 h), 0.57 (12 h), 0.60 (24 h), and 0.73 (36 h) dL/g.

It is reasonable to presume that the viscosity of polymer solution would be dependent on concentration and the average molecular size of the sample and hence the molecular weight. The MMA-MA-NIPA terpolymer prepared at different reaction time show a continuous decrease in intrinsic viscosity with decreasing MMA, MA and NIPA content in terpolymer structure. Viscosity and GPC results suggested that the MMA-MA-NIPA comonomer composition has a great effect on the resultant terpolymer molecular weight.

The antimicrobial effect of the on different pathogenic bacteria terpolymers on these microorganisms under *in vitro* conditions has been studied. The antibacterial activities of terpolymers were determined against six

bacteria (*Staphylococcus aureus*, *Salmonella enteritidis*, *Streptococcus faecalis*, *Escherichia coli*, *Klebsiella pneumonia* and *Pseudomonas aeruginosa*). The data for the antimicrobial tests are summarized in Table V.

TABLE V
IN VITRO ANTIMICROBIAL ACTIVITY OF POLYMERS AGAINST
STAPHYLOCOCCUS AUREUS, SALMONELLA ENTERITIS, STREPTOCOCCUS
FAECALIS, ESCHERICHIA COLI, KLEBSIELLA PNEUMONIAE AND
PSEUDOMONAS AERUGINOSA (DIAMETER OF ZONE, MM)

Reaction time	Gram-positive bacteria			Gram-negative bacteria		
	<i>S. aureus</i>	<i>S. enteritidis</i>	<i>S. faecalis</i>	<i>E. coli</i>	<i>K. pneumoniae</i>	<i>P. aeruginosa</i>
6 h	22	21	26	18	15	10
12 h	25	24	27	19	17	11
24 h	25	26	29	22	17	12
36 h	28	29	32	23	19	15

All polymers had different antibacterial activity *in vitro* against the tested bacterial strains. Terpolymer (reaction time: 36 h) showed more antimicrobial activity than other terpolymers (reaction time: 6, 12, and 24 h) against these strains. The highest inhibition of growth occurred for *Staphylococcus aureus*. The terpolymers generally affected *Staphylococcus aureus*, whilst the terpolymers were less effective against *Pseudomonas aeruginosa*. All polymers showed low antimicrobial activity against *Klebsiella pneumonia* and *Pseudomonas aeruginosa*. Microorganisms used in the present study are responsible for many hospital infections. For example, *Staphylococcus aureus* can cause pneumonia, meningitis, endocarditis, toxic shock syndrome (TSS) and septicemia.

All polymers studied, containing biologically active moieties in the form of carboxylic acid, anhydride, and amide groups and acid/amide complexed fragments, were more effective against Gram-positive bacteria than against Gram-negative bacteria [28]. This observation may be explained by different surface layer structural architectures of the biomacromolecules of the test bacteria. If the compounds can form covalent complexes or interact electrostatically with the cell wall, it is very probable that the compounds will show biocidal activity [29].

The terpolymers containing pendant groups derived from hydrolysis with strong hydrogen bonding tendencies easily form self-assembled structure with polymer chains through $COO^- \cdots +NH$ noncovalent interaction between free carboxylic groups of MA units and NIPA groups. As the ratio of $COOH/N$ increases (i.e., the number of $COOH$ groups increase) in the terpolymers, antimicrobial activity of the terpolymer toward Gram-positive bacteria increases [30].

The bacteria size varied between 500 and 3000 nm. This value is 20-60 times higher than the size of

terpolymers, which were in the size range of peptidoglycan network holes. These terpolymers can interact with the cell membrane, producing changes that would finally cause the death of the bacteria. However, another probable mechanism is the interaction with teichoic acid at the cell wall. This entity which contains phosphate bridges (negative charges) that could be interact electrostatically with the polycations. This would permit the polymer to stay at the bacterial cell, blocking the ion exchange channels, inhibiting growth, and producing cell death. Another possibility is the interaction with peptidoglycan, producing degradation and finally cell death [29].

IV. Conclusion

The present study involved the synthesis of poly(MMA-co-MA-co-NIPA) by radical-initiated polymerization in anhydrous medium. Chemical structure and compositions were identified by FTIR, UV-vis and ¹H NMR spectroscopy, and elemental analysis. Using ¹H NMR spectroscopy and elemental analysis data reflecting terpolymer composition, the values of m_1 , m_2 and m_3 for monomer pairs were found. The glass transition temperatures of terpolymer were controlled from 280 to 170 °C. Controlling glass transition temperatures could be important data while melt processing of these terpolymers. Terpolymers were thermooxidatively stable up to 420 °C. Thermal properties of polymer depend on the content of hydrogen-bonding fragments. The data obtained show that the terpolymers synthesized have antibacterial effects depending on the comonomer structure and molecular weight. In vitro evaluation of the MA terpolymers showed that they are antibacterial effectors. As the percentage of monomers in the terpolymer structures increases, the effectiveness of the terpolymers to inhibit the growth of the pathogen bacteria increases.

Acknowledgements

This work was supported by TÜBİTAK (The Scientific and Technological Research Council of Turkey) (project number: 107T299) and Gazi University Research Found (project numbers: 05/2007-10, 05/2007-44). The authors thank Environmental Engineer Nihat Demiroğlu for supports.

References

[1] D. Spridon, L. Panaitescu, et al., Synthesis and Biocompatibility of Maleic Anhydride Copolymers: I. Maleic Anhydride-Vinyl Acetate, Maleic Anhydride-Methyl Methacrylate and Maleic Anhydride-Styrene, *Polymer International*, Volume 43, (Issue 2), June 1997, Pages 175-181.

[2] S. Ranganathan, W.E. Baker, et al., Peroxide Initiated Maleic Anhydride Grafting: Structural Studies On An Ester-containing Copolymer and Related Substrates, *Journal of Polymer Science*

Part A: Polymer Chemistry, Volume 37, (Issue 11), June 1999, Pages 1609-1618.

[3] G.B. Butter, *Anionic Polymer Drugs* (Wiley-1980).

[4] Z.M.O. Rzaev, Complex-Radical Alternating Copolymerization, *Progress in Polymer Science*, Volume 25, (Issue 2), March 2000, Pages 163-217.

[5] L. Veron, M.C.D. Bignicourt, et al., Syntheses of Poly[N-(2,2 Dimethoxyethyl)-N-methyl acrylamide] for The Immobilization of Oligonucleotides, *Journal of Applied Polymer Science*, Volume 60, (Issue 11), April 1996, Pages 235-244.

[6] C. Ladaviere, A. Domard, et al., Covalent Immobilization of Biological Molecules to Maleic Anhydride and Methyl Vinyl Ether Copolymers - A Physico-Chemical Approach, *Journal of Applied Polymer Science*, Volume 71, (Issue 6), February 1999, Pages 927-936.

[7] C. Chaix, C. Minard-Basquin, et al., Oligonucleotide Synthesis on Maleic Anhydride Copolymers Covalently Bound to Silica Spherical Support and Characterization of The Obtained Conjugates, *Journal of Applied Polymer Science*, Volume 70, (Issue 12), December 1998, Pages 2487-2497.

[8] G.B. Buttler, *Cyclopolymerization and Cyclocopolymerization* (Marcel Dekker-1992).

[9] S.W. Shabaly, A.S. Hoffman, et al., *Polymers as Biomaterials* (Plenum Press-1984).

[10] M. Ignatova, N. Manolova, et al., Water-Soluble Polymers Bearing Biologically Active Residues, 3. Hydrolysis of Polyethers and Poly(ether-ester)s Bearing 1-Naphthylacetyl Groups, *Macromolecular Chemistry and Physics*, Volume 196, (Issue 5), May 1995, Pages 1663-1669.

[11] S. Richardson, P. Ferruti, et al., Poly(amidoamine)s as Potential Endosomolytic Polymers: Evaluation *In vitro* and Body Distribution in Normal and Tumour-Bearing Animals, *Journal of Drug Targeting*, Volume 6, (Issue 6), July 1999, Pages 391-404.

[12] R. Duncan, Polymer Conjugates for Tumour Targeting and Intracytoplasmic Delivery. The EPR Effect as A Common Gateway?, *Pharmaceutical Science & Technology Today*, Volume 2, (Issue 11), November 1999, Pages 441-449.

[13] E. Gianasi, M. Wasil, et al., HPMA Copolymer Platinates as Novel Antitumour Agents: *In vitro* Properties, Pharmacokinetics and Antitumour Activity *In vivo*, *European Journal Cancer*, Volume 35, (Issue 6), June 1999, Pages 994-1002.

[14] J.S. Patel, S.V. Patel, Bioactive Polymers: Synthesis, Release Study and Antimicrobial Properties of Polymer Bound Ampicillin, *Die Angewandte Makromolekulare Chemie*, Volume 271, (Issue 1), November 1999, Pages 24-27.

[15] G. Sun, T. Chen, T., et al., A Novel Biocidal Styrenetriazinedione Polymer, *Polymer*, Volume 37, (Issue 16), August 1996, Pages 3753-3756.

[16] H.K. Can, A.L. Doğan, et al., Synthesis and Antitumor Activity of Poly(3,4-Dihydro-2H-Pyran-co-Maleic Anhydride-co-Vinyl Acetate), *Journal of Applied Polymer Science*, Volume 96, (Issue 6), June 2005, Pages 2352-2359.

[17] A.D. Ernest, D.W. Lamb, Observation of Axial Acoustic Waves in Multimode PMMA Optical Fibres and Implications for A New Class of Optical Fibre Sensor, *Journal of Physics: Conference Series*, Volume 15, September 2005, Pages 270-275.

[18] E. Vargün, M. Sankir, et al., Synthesis and Characterization of 2-Hydroxyethyl Methacrylate (HEMA) and Methyl Methacrylate (MMA) Copolymer Used as Biomaterial, *Journal of Macromolecular Science Part A: Pure and Applied Chemistry*, Volume 47, (Issue 3), March 2010, Pages 235-240.

[19] T. Susdorf, D. del Agua, et al., Photophysical Characterization of Pyrromethene 597 Laser Dye in Silicon-Containing Organic Matrices, *Applied Physics B*, Volume 86, (Issue 3), February 2007, Pages 537-545.

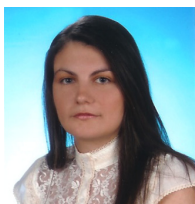
[20] K.M. Abedin, M. Alvarez, et al., 10 kHz Repetition Rate Solid-State Dye Laser Pumped by Diode-pumped Solid-State Laser, *Optics Communications*, Volume 218, (Issue 4-6), April 2003, Pages 359-363.

[21] M. Atai, D.C. Watts, et al., Shrinkage Strain-Rates of Dental Resin-Monomer and Composite Systems, *Biomaterials*, Volume 26, (Issue 24), August 2005, Pages 5015-5020.

- [22] M. Arimoto, H. Ichikawa, et al., Microencapsulation of Water-Soluble Macromolecules with Acrylic Terpolymers by The Wurster Coating Process for Colon-Specific Drug Delivery, *Powder Technology, Volume 141*, (Issue 3), March 2004, Pages 177-186.
- [23] M. Talu, E. Uzluk, et al., Synthesis and Characterization of Antimicrobial Copolymer and Terpolymers, *Drugs of the Future, Volume 32*, (Issue Suppl. A), July 2007, Pages 99-100.
- [24] N. Raman, A. Kulandaisamy, et al., Synthesis, Spectral, Redox and Antimicrobial Activities of Schiff Base Complexes Derived From 1-Phenyl-2,3-Dimethyl-4-Aminopyrazol-5-one and Acetoacetanilide, *Transition Metal Chemistry, Volume 26*, (Issue 1-2), February 2001, Pages 131-135.
- [25] S. Dinçer, V. Köseli, Radical Copolymerization of *N*-Isopropylacrylamide with Anhydrides of Maleic and Citraconic Acids, *European Polymer Journal, Volume 38*, (Issue 11), November 2002, Pages 2143-2151.
- [26] N.R. Cameron, J.M.G. Ferguson, et al., Enthalpy Relaxation of Styrene-Maleic Anhydride (SMA) Copolymers Part 1. Single Component Systems, *Polymer, Volume 41*, (Issue 19), September 2000, Pages 7255-7262.
- [27] U. Eisele, *Introduction to Polymer Physics* (Springer-1990).
- [28] A. Temiz, S.O. Togay, et al., Antimicrobial Poly(N-Vinyl-2-Pyrrolidone-alt-Maleic Anhydride)/Poly(Ethylene Imine) Macrocomplexes, *Journal of Applied Polymer Science, Volume 102*, (Issue 6), December 2006, Pages 5841-5847.
- [29] B.L. Rivas, E.D. Pereira, et al., Water-Soluble Cationic Polymers and Their Polymer-Metal Complexes With Biocidal Activity: A Genotoxicity Study, *Journal of Applied Polymer Science, Volume 87*, (Issue 3), January 2003, Pages 452-457.
- [30] H.K. Can, A.L. Doğan, et al., Synthesis, Characterization, and Antitumor Activity of Poly(Maleic Anhydride-co-Vinyl Acetate-co-Acrylic Acid), *Journal of Applied Polymer Science, Volume 100*, (Issue 5), June 2006, Pages -34253432.

Authors' information

Gazi University,
Faculty of Science and Arts,
Department of Chemistry,
Tekniokullar, 06500,
Ankara,
Turkey.



Elif Uzluk was born in Bursa, Turkey in 02/11/1982. Ms. Uzluk obtained his BSc from Gazi University, Department of Chemistry Teaching (Ankara, Turkey) in 2006. Ms. Uzluk received his MSc degree in 2008 from Gazi University, Department of Chemistry (Ankara, Turkey) where she studied synthesis, characterization and antimicrobial activity of water-soluble N-vinylimidazole-containing polymers. Ms. Uzluk is doctoral student in Physical chemistry at Gazi University, Department of Chemistry.

She published 10 articles between the years 2006-2010. She's previous publications include synthesis, characterization and electrochemical investigation of organic compounds; synthesis, characterization and antimicrobial effect of water-soluble N-vinyl-2-pyrrolidone-containing polymers; synthesis and characterization of conducting clay-polypyrrole composites. She research interests include the synthesis, characterization and antimicrobial activity of water-soluble maleic anhydride-containing polymers, quaternary ammonium compounds for antimicrobial materials; chemical or electrochemical synthesis and characterization new conducting clay-composites and clay-blends including modified polypyrrole, polythiophene and polyindene for electronic, electrochromic and photonic devices; electrochemical investigation of organic compounds.

Ms. Uzluk is a member Turkish Chemists Association and International Society of Electrochemistry.



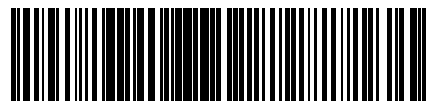
Muzaffer Talu was born in Ankara, Turkey in 11/13/1947. Prof. Talu obtained his BSc from Ankara University, Department of Chemical engineer (Ankara, Turkey) in 1970. Prof. Talu received his MSc degree in 1973 from Ankara University, Department of Chemistry (Ankara, Turkey), where she studied synthesis and characterization of acrylate-containing polymers. Prof. Talu obtained her PhD degree in 1977 from Ankara University, Department of Chemistry (Ankara, Turkey), where she studied kinetic investigation of solution polymerization of ethylacrylate.

She published 75 articles between the years 1974-2010. She's previous publications include synthesis of graft copolymerization methyl methacrylate; solution polymerization of ethylacrylate; grafting of poly(ethylene terephthalate) fibers with methacrylic acid; electrochemical polymerization of aniline, thiophene, pyrrole, furan and its derivatives; synthesis and characterization of conducting polymer-insulating polymer composite; synthesis, characterization and antimicrobial activity of water-soluble N-vinyl-2-pyrrolidone-containing polymers, synthesis and characterization of conducting clay-polypyrrole composite. She research interests include the synthesis, characterization of graft copolymerization methyl methacrylate on to polyethylene terephthalate; electrochemical polymerization of aniline, thiophene, pyrrole, furan and its derivatives; synthesis, characterization and antimicrobial activity of water-soluble maleic anhydride-containing polymers, quaternary ammonium compounds for antimicrobial materials; chemical or electrochemical synthesis and characterization new conducting clay-composites and clay-blends including modified polypyrrole, polythiophene and polyindene for electronic, electrochromic and photonic devices.

Prof. Talu is a member Turkish Chemical Society and Turkish Chemical Engineer Chamber.



Praise Worthy Prize



2038-033X(201008)1:1;1-A